

Department of Physics and Astronomy  
Ruprecht-Karls-University Heidelberg

**Master thesis**  
in Physics

submitted by

**Neta Tsur**

born in Ramat Gan, Israel

**2013**



**Noble gas isotopic signatures in thermal waters of the  
Dead Sea Transform, Israel**

This Master thesis has been carried out by Neta Tsur at the

**Institute of Environmental Physics**

under the supervision of

**Prof. Dr. Werner Aeschbach-Hertig**



*“There is running water and not a seasonal stream,  
the Jordan River is proudly flowing”*

Somewhere in the Valley, Noah Warschauer



**Abstract:**

Noble gas isotope composition (especially helium) in thermal waters from different areas along the Dead Sea Transform in Israel reveals local intrusions of volatile gases and heat flux from the mantle into the crust. The distinct  $^3\text{He}/^4\text{He}$  ratios in the atmosphere, crust and mantle enable one to separate the total helium concentration into mantle, crustal and atmospheric components. Helium isotope ratios of all sampled waters exceed the typical crustal ratio, indicating contributions of mantle derived helium to the total helium concentration. A clear trend can be observed in  $^3\text{He}/^4\text{He}$  ratios from different areas. Northern samples show higher  $^3\text{He}/^4\text{He}$  ratios than southern ones. Noble gas temperatures (NGTs) were used to determine the atmospheric helium component. Most of the samples contain less than 3% atmospheric helium, whereas the mantle derived helium component ranges from 2% to 38%. In addition to helium, the origin of  $\text{CO}_2$  in the water is examined. Measurements of  $\delta^{13}\text{C}$  indicate no mantle derived  $\text{CO}_2$ . Furthermore, stable isotopes data ( $\delta^{18}\text{O}$  and  $\delta^2\text{H}$ ) show no evidence of mantle derived water or water from reservoirs exceeding 100 °C.

**Zusammenfassung:**

In dieser Arbeit wird die isotopische Zusammensetzung von Edelgasen (vor allem Helium) in Thermalwasser entlang des israelischen Teils des Jordangrabens analysiert. Da sich das  $^3\text{He}/^4\text{He}$ -Verhältnis von Atmosphäre, Kruste und Mantel deutlich unterscheidet, lassen sich die Beiträge der einzelnen Edelgasreservoirs voneinander trennen. Die Untersuchungen zeigen, dass Gase und Wärme aus dem Erdmantel in die Erdkruste eindringen. Alle Wasserproben weisen ein  $^3\text{He}/^4\text{He}$ -Verhältnis auf, das deutlich höher ist als jenes der Kruste; folglich stammt zumindest ein Teil des Heliums aus dem Mantel. Ferner ist in den  $^3\text{He}/^4\text{He}$ -Verhältnissen ein klarer geographischer Trend erkennbar: Im Norden ist das Wasser deutlich stärker vom Manteleinfluss geprägt als die Proben aus den südlicheren Regionen.

Der atmosphärische Heliumanteil wurde mit Hilfe der Edelgastemperaturen (NGT) bestimmt. Die meisten Proben weisen weniger als 3% atmosphärisches Helium auf, wohingegen der Mantelanteil im Bereich von 2% bis 38% liegt.

Zusätzlich wurde die Herkunft des im Wasser gelösten  $\text{CO}_2$  untersucht. Dabei zeigen die Messungen von  $\delta^{13}\text{C}$ , dass das  $\text{CO}_2$  nicht aus dem Mantel stammt. Des Weiteren ergibt die Analyse der stabilen Isotope ( $\delta^{18}\text{O}$  und  $\delta^2\text{H}$ ), dass auch das Wasser nicht aus dem Mantel kommt und nie heißer als 100 °C war.



# Contents

<b>1</b>	<b>Introduction</b>	<b>11</b>
<b>2</b>	<b>Theory</b>	<b>15</b>
2.1	Solubility of noble gases . . . . .	15
2.2	Components of noble gases in groundwater . . . . .	17
2.3	Noble gases as paleoclimate tracers . . . . .	18
2.3.1	Excess air models . . . . .	18
2.3.2	Determination of noble gas temperatures . . . . .	22
2.4	Mantle derived isotopes in groundwater . . . . .	22
2.4.1	Helium isotopes: $^3\text{He}$ and $^4\text{He}$ . . . . .	22
2.4.2	$\text{CO}_2$ and $\delta^{13}\text{C}$ . . . . .	29
2.4.3	Stable isotopes: $\delta^{18}\text{O}$ and $\delta^2\text{H}$ . . . . .	31
<b>3</b>	<b>The Dead Sea Transform</b>	<b>33</b>
3.1	Geographic setting . . . . .	33
3.2	Tectonic setting . . . . .	34
3.3	Hydrogeology . . . . .	36
3.4	Sampling sites . . . . .	39
<b>4</b>	<b>Methods</b>	<b>41</b>
4.1	Water characteristics . . . . .	41
4.2	Noble gases: Mass spectrometry . . . . .	41
4.2.1	Sampling . . . . .	41
4.2.2	Measurement . . . . .	42
4.2.3	Data evaluation . . . . .	43
4.3	Isotopic composition . . . . .	45
4.3.1	Tritium . . . . .	45
4.3.2	$\delta^{13}\text{C}$ . . . . .	45
4.3.3	Stable isotopes . . . . .	46
<b>5</b>	<b>Results</b>	<b>47</b>
5.1	Noble gas temperatures . . . . .	50
5.2	Helium isotopes . . . . .	54
5.3	Helium components . . . . .	55
5.3.1	Tritiogenic helium: . . . . .	56
5.3.2	Terrigenous versus atmospheric helium: . . . . .	56
5.3.3	Separation of atmospheric, crustal and mantle derived helium . . . . .	60
5.4	Carbon isotopes . . . . .	63
5.5	Stable isotopes . . . . .	67
<b>6</b>	<b>Discussion</b>	<b>69</b>
6.1	Spatial distribution of $^3\text{He}/^4\text{He}$ . . . . .	69

6.2	Mantle, crustal and atmospheric components distribution . . . . .	70
6.3	The geothermal structure of the Dead Sea Transform . . . . .	71
6.4	Other isotopes as tracers for mantle flux . . . . .	74
6.4.1	Carbon isotopes . . . . .	74
6.4.2	Stable isotopes . . . . .	75
<b>7</b>	<b>Summary and outlook</b>	<b>77</b>
<b>A</b>	<b>Appendix</b>	<b>79</b>
A.1	Ostwald solubility calculation . . . . .	79
A.2	Mixing ratios of noble gases . . . . .	79
A.3	Stable isotopes notation . . . . .	79
A.4	Locations in Israel . . . . .	80
A.5	A detailed description of the sampling sites and the sampling process . . . . .	82
A.6	Neon and argon isotopic ratios . . . . .	91
A.7	Noble gas concentrations of the second and third measurement runs . . . . .	91
A.8	Additional figures . . . . .	94
	<b>List of Figures</b>	<b>97</b>
	<b>List of Tables</b>	<b>99</b>
	<b>Bibliography</b>	<b>103</b>

# 1 Introduction

The Earth was formed approximately four and a half billion years ago from a cloud of dust and gases that generated a melted sphere. This sphere started to cool down and different layers were formed. First, the outer thin crust was created, later the upper and lower mantle and finally the inner core (Figure 1.1). At the time the mantle was formed, it trapped a great amount of volatile gases. During the first 50 million years from Earth formation, massive degassing occurred in the mantle and partly continues at the present time [Allègre et al., 1987]. Some of the escaping volatiles infiltrate into the crust during the evolution of igneous rocks and can be dissolved by local groundwater. Among them are CO<sub>2</sub> and noble gases, which can be measured and provide information of a regional crust-mantle interaction.

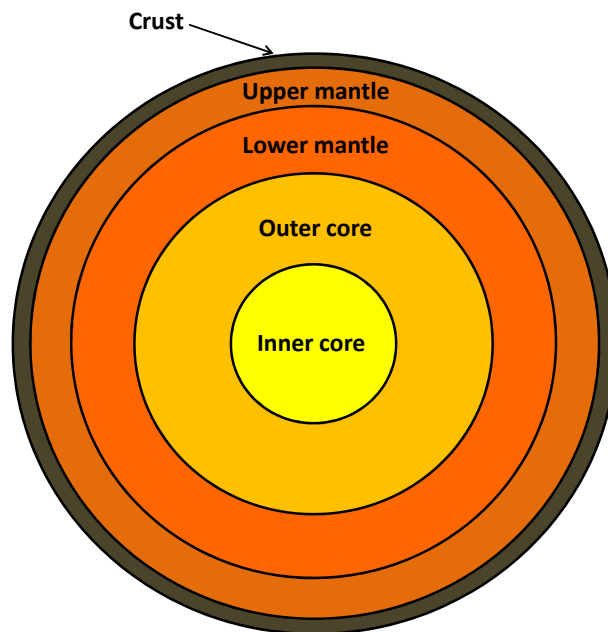


Figure 1.1: Interior layers of Earth (figure is not to scale).

There are five stable noble gases in nature: Helium (He), neon (Ne), argon (Ar), krypton (Kr) and xenon (Xe). They belong to a group of elements that have a full outer shell of valence electrons. Hence they are chemically inert and conservative. In addition, noble gases are found in rare amounts, which makes them ideal tracers in environmental studies.

Noble gases in groundwater usually originate from three main reservoirs: The atmosphere, the crust and the mantle. Each reservoir contributes a different fraction to their total dissolved concentration in groundwater. The fact that each fraction from each reservoir retains its composition is a powerful tool, which enables to separate the measured noble gas concentrations to atmospheric, crustal and mantle components. The distribution of

these components provides information about the groundwater recharge conditions and the crustal environments it was circulating through, since it had infiltrated into the ground.

The composition of the atmospheric component can be used for paleoclimate records. Since the solubility of noble gases depends on the temperature, the dissolved concentration of noble gases from atmospheric origin is attributed to the air temperature in the recharge zone at the recharge time. This effect is called Noble Gas Temperature (NGT) [Mazor, 1972].

Another use of noble gases in groundwater is to identify volatile fluxes from the mantle into a certain region of the crust, in which the water circulates. Thermal groundwater usually reaches large depths, where intrusion of volatiles from the mantle is likely to occur. Helium isotopes are commonly used to trace these intrusions. The isotope  $^3\text{He}$  mostly originates from the mantle and does not have a large surface inventory. Moreover, each of the helium reservoirs (mantle, crust and atmosphere) has a different fractionation ratio of  $^3\text{He}/^4\text{He}$ , thus making it possible to distinguish between mantle, crustal and atmospheric derived helium. Helium isotopes and other volatiles found in groundwater provide important information about mantle evolution and crust-mantle interactions, in form of geotectonic activity, volcanism and advective heat transfer [Sano and Wakita, 1988 and Mamyrin and Tolstikhin, 1984]. The geothermal state of the crust provides information of thermal energy resources, which are of environmental and economic importance.

Other isotopes can be analysed as well in order to detect other volatiles from the mantle. For example,  $^{13}\text{C}$  is used as a tracer for mantle derived  $\text{CO}_2$ . The stable isotopes  $^{18}\text{O}$  and  $^2\text{H}$  are often used as tracers of interaction between groundwater and local rocks. Such interaction occurs in high temperatures, which are sometimes caused by enhanced heat fluxes from the mantle. However, most of the volatiles have a high chemical and biological reactivity. Hence, it is more complicated to identify their fluxes from the mantle, compared to using noble gases.

This thesis analyses noble gases and other isotopes dissolved in thermal waters along the Israeli part of the Dead Sea Transform. It has been carried out parallel to the work of Kaudse [2014], who analyses thermal waters along the Jordanian part of the Dead Sea Transform. There exist former studies that analysed noble gases along the Dead Sea Transform in Israel. Mazor et al. [1973] measured noble gases in Hammat Gader springs in the Yarmouk Valley to identify mixing between groundwaters with different temperatures and salinities. Herzberg and Mazor [1979] measured noble gases in cold springs along the Dead Sea Transform and other parts of Israel to determine paleotemperatures. Ratios of  $^3\text{He}/^4\text{He}$  along the Dead Sea Transform were measured by Bergelson et al. [1999] on the western side of Lake Kinneret and Lange et al. [2008], who measured  $^3\text{He}/^4\text{He}$  ratios in the vicinity of Jericho. Both used the helium isotopes as tracers of groundwater salinization. Very recently, a detailed study of helium isotopes from springs and wells along the Dead Sea Transform was published by Torfstein et al. [2013]. The data were measured 15 years ago (1995–1998) and were analysed in order to find mantle derived helium.

In this thesis, thirteen samples were taken from thermal wells and springs in Israel in December 2012. The sampling sites are located in different regions from the Hula Valley in the north, to Arava Valley in the south. Concentrations of noble gases and their isotopes, as well as other isotopes of  $^{13}\text{C}$ ,  $^{18}\text{O}$  and  $^2\text{H}$  were measured. They were used for identifying volatiles from the mantle in the groundwater and determine noble gas temperatures. The main purpose of this work is to analyse the  $^3\text{He}/^4\text{He}$  ratio regarding to infiltration of mantle derived helium into the groundwater. Besides,  $^{13}\text{C}$  is used to determine the origin

---

of CO<sub>2</sub>, which is one of the main volatiles still escaping from the mantle. Furthermore, <sup>18</sup>O and <sup>2</sup>H are used to identify temperature anomalies in the crust, which are often caused by heat transfer from the mantle into the crust.



## 2 Theory

### 2.1 Solubility of noble gases

The concentration of a gas dissolved in water under equilibrium conditions is proportional to its concentration in the gas phase as defined by the so called Henry's law [Aeschbach-Hertig and Solomon, 2013]:

$$c_{ig} = H_i(T, S) \cdot c_{iw} \quad (2.1)$$

$c_{ig}$  and  $c_{iw}$  are the concentrations of species  $i$  in [mol/l], in gas and liquid phases, respectively.  $H_i$  is called Henry coefficient and is dimensionless. The concentration of a substance in a gas phase can be converted to partial pressure, thus Henry's law can also be written as:

$$p_i = H'_i \cdot c_{iw} \quad (2.2)$$

$p_i$  is the partial pressure of gas species  $i$  and  $H'_i$  is Henry coefficient in units of [atm·l/mol], so that  $H'_i = H_i \cdot RT$ . The pressure  $p_i$  is calculated from the concentration in a gas phase via the equation of state:

$$p = \frac{n}{V}RT = c_gRT \quad (2.3)$$

$n$  is number of moles of the gas,  $V$  is the volume occupied by the gas,  $R$  is the Gas Constant and  $T$  is the temperature.

Solubility is defined as the ratio between the concentration of a substance in a liquid phase and the concentration of it in a gas phase:

$$k_i = \frac{c_{iw}}{c_{ig}} = \frac{1}{H_i} \quad (2.4)$$

Higher solubility increases  $c_{iw}$ . There are number of definitions of solubility coefficients, deduced from different parameters of the system. For example, Ostwald solubility is defined as the ratio between the volume of a substance in a gas phase and the volume of it in a liquid phase:

$$L_i = \frac{V_{ig}}{V_{iw}} = \frac{1}{H_i} \quad (2.5)$$

Another form of Ostwald solubility is:

$$\lambda_i = \frac{c_{iw}}{p_i} = \frac{1}{H'_i} \quad (2.6)$$

$\lambda_i$  is given in units of [mol/atm·l].

Dissolving is a thermodynamic process which depends on temperature, salinity and pressure:

$$k_s = k_s(T, S, p) \quad (2.7)$$

The relationship between solubility and temperature can be determined by Van't Hoff equation. The following relation for Ostwald solubility was obtained by [Benson and Krause Jr. \[1976\]](#):

$$\ln\left(\frac{1}{H_i}\right) = \ln(L_i(T, S=0)) = a_0 + a_1 \cdot \frac{1}{T} + a_2 \cdot \frac{1}{T^2} \quad (2.8)$$

The parameters  $a_0$ ,  $a_1$  and  $a_2$  depend on the gas species and are calculated for temperatures in [K]. They are given in Appendix [A.1](#) for each noble gas.

Higher water salinity reduces the solubility, which is called ‘‘salting-out’’ effect. This effect can be neglected for very low salinities, i.e. fresh water. The decrease of the solubility with the temperature and salinity is demonstrated in Figure [2.1](#).

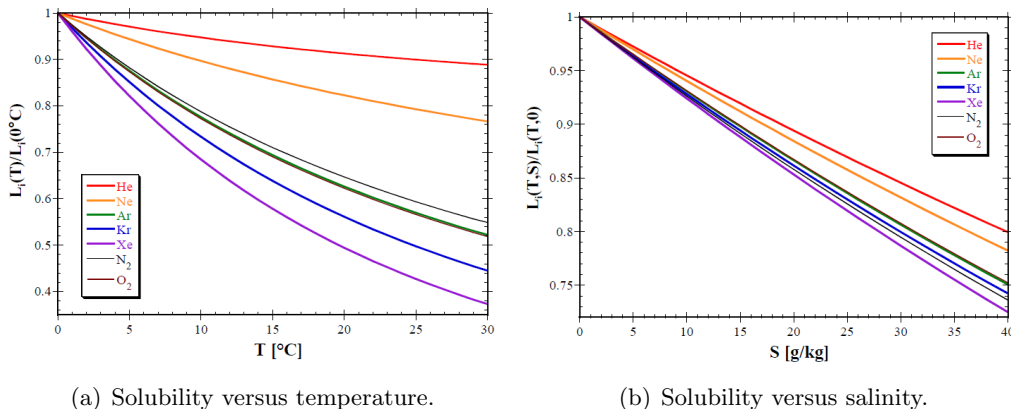


Figure 2.1: Solubility of the most abundant atmospheric gases and noble gases, adapted from [Cook and Herczeg \[2000\]](#).  $L_i(T)$  and  $L_i(T, S)$  refer to the solubility of each gas species  $i$  (see legend) in temperature  $T$  and salinity  $S$ . They are normalized to the solubility value in  $T = 0^\circ\text{C}$ . Adapted from [Kaudse \[2014\]](#).

The dependency of solubility on pressure is indirect, since the partial pressure of a gas,  $p_i$ , from Equation [2.2](#) depends on the temperature and on the water vapour pressure, which also depends on the temperature. Since the boundary layer between the water and air, where gas exchange takes place, is saturated in water vapour, its pressure should be subtracted from the dry air pressure to obtain the partial pressure:

$$p_i(z, T) = (p(z) - e_w(T)) x_i \quad (2.9)$$

$x_i$  is atmospheric mixing ratio of gas  $i$ , relative to dry air. The mixing ratios of noble gases in the atmosphere given in in appendix [A.2](#). The air pressure on the water surface altitude,  $p(z)$ , is given by the barometric Equation [[Roedel and Wagner, 2010](#)]:

$$p(z) = p_0 \cdot \exp\left(-\frac{z}{z_s}\right) \quad (2.10)$$

$$z_s = \frac{RT}{Mg}$$

The scale height,  $z_s = z_s(T)$  depends on the temperature, but is usually approximated to be  $z_s = 8000$  m.  $M$  is the molar mass of air. The water vapour pressure,  $e_w$ , is determined empirically.

## 2.2 Components of noble gases in groundwater

Noble gases dissolved in groundwater origin from different sources and their total concentration is composed of contributions of the different sources. Figure 2.2 shows that all noble gases origin from the atmosphere and that helium has additional contributions from non-atmospheric sources. Separation of the different components of the noble gases in a groundwater reservoir may give information about the characteristics of the reservoir, such as time scales (dating) and paleotemperatures. The latter will be discussed in Section 2.3.2.

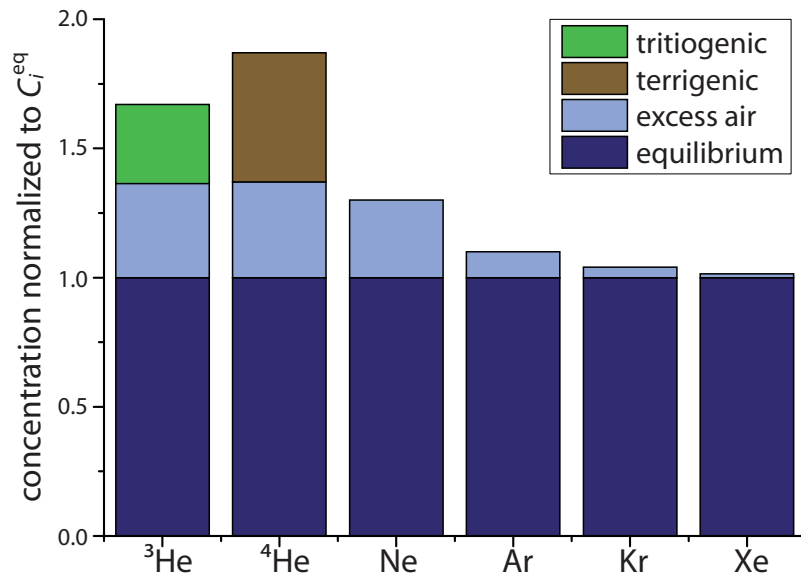


Figure 2.2: Noble gas components in groundwater, normalized to air equilibrated water. Note that all gases origin from the atmosphere (equilibrium and excess air components) and helium has additional non atmospheric components. Argon has a non-atmospheric component too, which is neglected for the purpose of this work. Adapted from Kipfer et al. [2002].

**Equilibrium component:** Recharging groundwater water exchanges gases with the atmosphere according to Henry's law (equations 2.1 and 2.2). Inserting  $p_i$  from Equation 2.9 into Equation 2.2, the equilibrium component of gas  $i$  in water is:

$$c_{iw}^{eq} = \frac{(p(z) - e_w(T)) x_i}{RT} \quad (2.11)$$

If the groundwater is formed from fresh water, such as meteoric water, salting out effect can be neglected, thus the equilibrium component depends only on the temperature.

**Excess air component:** Most groundwater samples contain additional dissolved noble gases with atmospheric composition, i.e. higher than the concentration of the equilibrium component, attributed to bubbles entrapment in the water [Heaton and Vogel, 1981]. This

excess air amount decreases for heavier noble gases, as can be seen in Figure 2.2. There are number of models that aim to explain and quantify this component, as described in Section 2.3.1.

**Tritogenic component:** Groundwater acts like a closed system for tritium and helium from the moment it loses contact with the atmosphere, thus, their total amount is conserved with time:

$${}^3\text{He}_{\text{tri}}(t) = {}^3\text{H}(0) - {}^3\text{H}_{\text{tri}}(t) \quad (2.12)$$

Tritium has a relatively short lifetime of  $T_{1/2} = 12.43$  years [Schlosser et al., 1989], therefore finding tritium in old water indicates mixing with younger water. The  ${}^3\text{H}$ - ${}^3\text{He}$  age, used for dating, is:

$$\tau = \frac{1}{\lambda} \ln \left( 1 + \frac{{}^3\text{He}_{\text{tri}}(t)}{{}^3\text{H}_{\text{tri}}(t)} \right) \quad (2.13)$$

Note that  $\tau$  is the time since the water was isolated from the atmosphere. The decay constant is:  $\lambda = \frac{\ln 2}{T_{1/2}} = 0.056 \text{ a}^{-1}$ .

**Terrigenous component:** This terrigenous component refers to noble gases that originate from the solid Earth and found in helium isotopes and  ${}^{40}\text{Ar}$ . This component is usually crustal (radiogenic) from nuclear production. Radiogenic components of other noble gas isotopes are usually very small and can be neglected [Kipfer et al., 2002].  ${}^3\text{He}$  is produced from Li and  ${}^4\text{He}$  is produced by  $\alpha$  decay of Th [Mamyrin and Tolstikhin, 1984 and Schlosser et al., 1989]:



It is important to notice that  ${}^3\text{He}$  is also produced from atmospheric tritium, which is considered to be a different component. In addition, some part of the helium can come from the mantle. Distinguishing the mantle from the crustal component, one can tell about the geothermal structure of the environment that the water comes from, as further explained in Section 2.4. The isotope  ${}^{40}\text{Ar}$  is produced from  ${}^{40}\text{K}$  and may also have a radiogenic fraction. Further discussion about helium components and mantle derived helium is found in Section 2.4.

## 2.3 Noble gases as paleoclimate tracers

### 2.3.1 Excess air models

There are number of models that are used for separation of the excess air component from the equilibrium component in groundwater samples. Each model assumes different formation processes of excess air, as demonstrated in Figure 2.3. The models which are used in this work and a few similar models are presented in the following text. In all models helium is usually excluded from the analyse, since it contains non atmospheric components, making the separation of excess air more complicated. The information in this section is mostly based on Aeschbach-Hertig et al., 2008 and Aeschbach-Hertig and Solomon, 2013

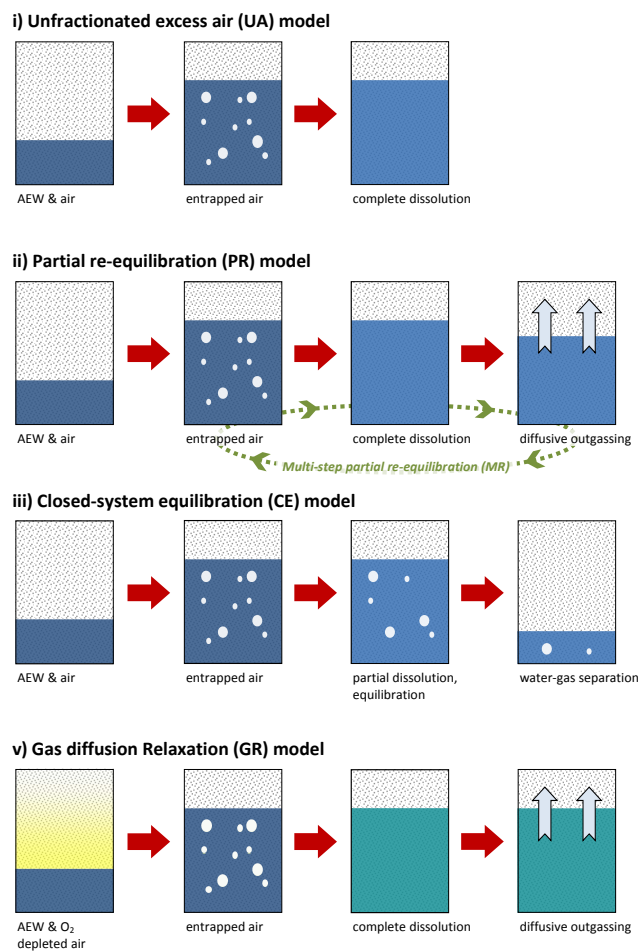


Figure 2.3: Illustrations of the excess air models described in Section 2.3.1. The different mechanisms of excess air formation in groundwater are shown here. Starting from the classical model of UA at the top further modified models below. Adapted from Wieser [2011] and modified by Mayer [2012].

**Unfractionated excess air model (UA)** This model represents the most simplified case of complete dissolution of entrapped air bubbles. The noble gas concentration in the groundwater is the sum of an equilibrium component and additional complete dissolution of air bubbles with the same equilibrium composition, given by Henry's law (Equation 2.1):

$$c_{iw}^{UA} = c_{iw}^{eq} (1 + AH_i) \quad (2.16)$$

The model has one parameter,  $A = \frac{V_a}{V_w}$ , which is the volume of dissolved air,  $V_a$ , relative to the water volume,  $V_w$ . Equation 2.16 can be written for an "effective air fraction"  $A'$ . Inserting the second term of Equation 2.16 into Henry's law (Equation 2.2) yields:

$$\begin{aligned} c_{iw}^{UA} &= c_{iw}^{eq} + A'x_i & (2.17) \\ A' &= A \frac{p - e_w}{RT} \\ A'x_i &= c_{iw}^{eq} AH_i = A \cdot c_{ia} \end{aligned}$$

$c_{ia}$  denotes the concentration of noble gas  $i$  in the gas phase. It is clear from Equation 2.17 noble gases with higher mixing ratios contribute more excess air, therefore argon, which has the biggest mixing ratio (see Table A.2) has a higher excess air concentration than the rest of the gases.

**Partial re-equilibration model (PR)** This model describes a complete dissolution of the entrapped air, followed by diffusive degassing leading to re-equilibration of the groundwater with the soil air. The excess air concentration then decreases and changes its composition due to depletion in light gases.

$$c_{iw}^{PR} = c_{iw}^{eq} \left( 1 + AH_i \cdot e^{-F_{PR} \left( \frac{D_i}{D_{Ne}} \right)^\beta} \right) \quad (2.18)$$

The parameters of this model are:  $A$ , which is the volume fraction of dissolved excess air relative to the water,  $F_{PR}$  is the degree of excess air loss after the re-equilibration,  $D_i$  denotes the diffusion coefficient of noble gas  $i$  in water,  $\beta$  refers to the degree of gas transfer due to diffusion and can vary between 0.5 to 1 [Aeschbach-Hertig and Solomon, 2013].  $D_i$  is normalized to the diffusion coefficient of neon, which is assumed to origin only from atmospheric source, as shown in Figure 2.2. Inserting  $F_{PR} = 0$  into Equation 2.18 gives the limit case of the UA model. As  $F_{PR} \rightarrow \infty$ , fractionation of all the noble gases takes place, so that all the excess air component diffuses from the water and vanishes, therefore samples that have high  $F_{PR}$  values might be close to Air Equilibrated Water (AEW). A special case of this model is the **partial degassing model (PD)**, where diffusive degassing acts on the total gas concentration and not only on the excess air component [Aeschbach-Hertig et al., 2008].

**Multi-step partial re-equilibration model (MR)** A modified PR model, in which the re-equilibration takes places in more than one step [Kipfer et al., 2002]. The model is described by the following equation:

$$\begin{aligned} c_{iw}^{MR} &= c_{iw}^{eq} \left( 1 + AH_i \cdot \sum_{k=1}^n e^{-kR_i} \right) = c_{iw}^{eq} \left( 1 + AH \cdot e^{-R_i} \frac{1 - e^{-nR_i}}{1 - e^{-R_i}} \right) & (2.19) \\ R_i &= F_{MR} \left( \frac{D_i}{D_{Ne}} \right)^\beta \end{aligned}$$

$n$  is the number of re-equilibration steps,  $R_i$  is the exponent defined by the former PR model. The parameter  $A$  is the dissolved excess air volume fraction relative to the water. The lower limit case of this model is the PR model which is obtained for  $n = 1$ .

**Closed-system equilibration model (CE)** The scenario described by this model is of air entrapment at the recharge zone, followed by partial dissolution, due to the increasing hydrostatic pressure, as the groundwater table rises [Aeschbach-Hertig et al., 2008]. The concentration of the dissolved excess air is:

$$c_{iw}^{CE} = c_{iw}^{eq} \frac{1 + AH_i}{1 + BH_i} = c_{iw}^{eq} \left( 1 + \frac{(1 - F_{CE}) AH_i}{1 + F_{CE} AH_i} \right) \quad (2.20)$$

The concept of the model is illustrated in Figure 2.4. The parameter  $A = \frac{V_a}{V_w}$  represents the total volume of air entrapped in the recharge zone ( $V_a$ ) relative to the water volume ( $V_w$ ). Note that it is defined here as the fraction of air entrapped at the recharge zone and is different than the  $A$  parameter from the other models, which represents the total amount of dissolved excess air.  $B = \frac{V_b}{V_w}$  is the total volume of the remaining air after the partial dissolution, relative to the water volume.  $A$  and  $B$  define the fractionation parameter  $F = \frac{B}{A} = \frac{V_b}{V_a}$ . Inserting  $F < 1$  (i.e.  $B < A$ ) into Equation 2.20 means that some of the initially entrapped air is dissolved, which corresponds to excess air formation. Taking  $F > 1$  (i.e.  $B > A$ ) means there is more air after the dissolution, than entrapped in the recharge zone, therefore it corresponds to degassing.  $F = 0$  ( $B = 0$ ) corresponds to complete dissolution, hence the UA model. CE is the only model presented here, which assumes a direct partial dissolution without any intermediate step on complete dissolution.

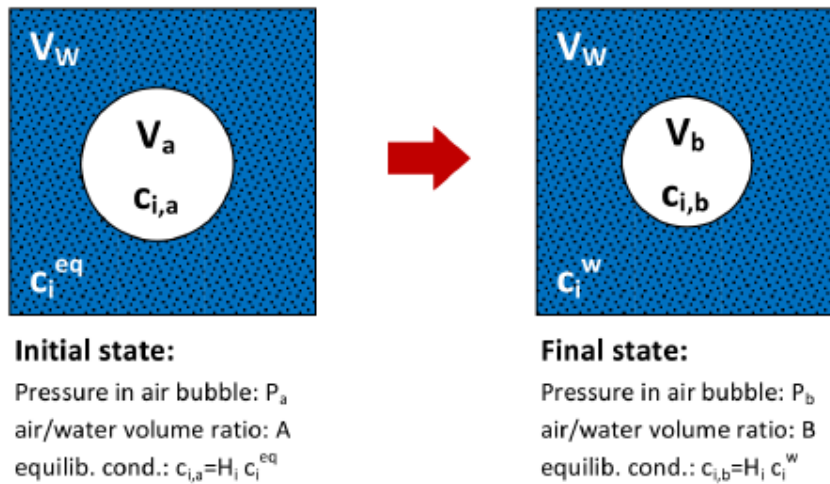


Figure 2.4: Derivation of the CE model, adapted from Aeschbach-Hertig et al. [2008].

Excess air is first entrapped in groundwater in the recharge zone. The total volume of the air is  $V_a$  and the concentration of noble gas  $i$  in the air is  $c_{i,a}$ . The volume of the surrounding water is  $V_w$  and the equilibrium concentration of each dissolved noble gas is  $c_i^{eq}$ . As the hydrostatic pressure increases, a fraction of the air bubbles dissolves until new equilibrium is reached. The total volume of the remaining air is  $V_b$  and the concentration of each noble gas in the air bubble is  $c_{i,b}$ . The volume of the water changes negligibly. The concentration of each noble gas, dissolved as excess air component is  $c_i^w$  and is given by Equation 2.20.

### 2.3.2 Determination of noble gas temperatures

As explained before, the solubility of noble gases in fresh water (with  $S=0$ ) depends only on the temperature. If it is possible to separate the equilibrium component from the others (Figure 2.2), the corresponding temperature determined from equilibration solubility (Equation 2.8) is the temperature at the groundwater table at the time of recharge, called **Noble Gas Temperature (NGT)** [Ballentine and Hall, 1999 and Aeschbach-Hertig et al., 1999]. Cook and Herczeg [2000] suggest that the **NGT** corresponds to the ground temperature of the water or soil in the recharge area.

Helium and argon contain non atmospheric components, therefore their concentrations must be corrected to atmospheric components for the **NGT** determination. Since the solubility of helium depends only weakly on the temperature, it is excluded from the determination [Aeschbach-Hertig and Solomon, 2013]. The equilibrium component of argon can be separated more easily, since most of it comes from  $^{36}\text{Ar}$ . Hence, in case the measured ratio of  $^{36}\text{Ar}/^{40}\text{Ar}$  is smaller than the atmospheric ratio of 0.003378 [Aeschbach-Hertig and Solomon, 2013],  $^{40}\text{Ar}$  is excluded from the **NGT** determination.

The measured concentration of each noble gas can be written as follows:

$$c_i^{meas} = c_i^{eq}(T, S, p) + c_i^{ex}(A, F) \quad (2.21)$$

Here,  $c_i^{meas}$  is the measured concentration of species  $i$ ,  $c_i^{eq}$  is the concentration of the equilibrium component, which depends on water temperature, salinity and air pressure and  $c_i^{ex}$  is the concentration of the excess air component, which depends on the parameters of the chosen excess air model, described in Section 2.3.1.  $A$  and  $F$  in Equation 2.21 are the parameters of the **CE** model, which is used for the analysis in this work. Salinity of  $S = 0$  can be assumed if the groundwater comes from meteoric origin and the pressure can be calculated from the estimated recharge altitude, with the barometric formula (Equation 2.10). Equation 2.21 can be written for each species  $i$  (Ne, Ar, Kr or Xe), making four equations. Since there are only three unknowns, the system overdetermined.

Ballentine and Hall [1999] and Aeschbach-Hertig et al. [1999] suggest to use inverse modelling instead of Equation 2.21, which cannot be solved. The idea is to find a set of parameters  $A$ ,  $T$  and  $F$ , which give the closest modelled concentrations,  $c_i^{mod}$ , to the measured ones,  $c_i^{meas}$ . The minimal difference between the modelled and measured concentrations can be found by minimizing  $\chi^2$ , defined as:

$$\chi^2 = \sum_i \frac{c_i^{meas} - c_i^{mod}}{\sigma_i^2} \quad (2.22)$$

$\sigma_i$  is the experimental  $1\sigma$  error of the species  $i$ . The lower  $\chi^2$  is, the better the fit is.

According to Sun et al. [2010], the same model should be used for the whole data set to enable comparison of **NGTs** to present temperature for a paleoclimate record.

## 2.4 Mantle derived isotopes in groundwater

### 2.4.1 Helium isotopes: $^3\text{He}$ and $^4\text{He}$

Helium has two stable isotopes:  $^3\text{He}$  and  $^4\text{He}$ . The second is very abundant and composes almost 100% of the total helium inventory, while the first constitutes only  $\sim 10^{-4}\%$  of

it (Table 4.1). Helium in groundwater originates from three main reservoirs: The atmosphere, the crust and the mantle. Each of them has a characteristic  $^3\text{He}/^4\text{He}$  ratio. The atmospheric ratio  $^3\text{He}/^4\text{He} = (1.384 \pm 0.006) \cdot 10^{-6}$  [Clarke et al., 1976], usually written as  $R_a$ , is constant due to the long residence time of helium there, which is  $10^5$  times longer than the mixing time of the atmosphere [Lupton, 1983]. Other helium isotope ratios are usually normalized to this constant ratio, for convenience. AEW has a slightly lower  $^3\text{He}/^4\text{He}$  ratio of  $1.360 \cdot 10^{-6}$ , due to slightly different solubility coefficients of  $^3\text{He}$  and  $^4\text{He}$  [Benson and Krause Jr., 1980]. Crustal helium is produced in nuclear reactions and depends on the concentration of its precursors (see Section 2.2). The  $^3\text{He}/^4\text{He}$  ratio of crustal helium ranges from  $1 \cdot 10^{-8}$  to  $3 \cdot 10^{-8}$ , corresponding to  $\sim 0.01 R_a$  [Mamyrin and Tolstikhin, 1984]. The upper mantle is characterised with the highest  $^3\text{He}/^4\text{He}$  ratio of  $\sim 10^{-5}$ , corresponding to  $(8 \pm 1) R_a$  [Graham, 2002]. The fact that these three reservoirs vary widely in their helium isotope composition, enables scientists to differentiate the origin of fluids.

Helium in the mantle, also called primordial helium, originates from solar nebulae during the early stages of the universe formation. The mantle reservoir of helium has two main sources: Ocean Island Basalts (OIB) and Mid Ocean Ridge Basalts (MORB), both contribute to the formation of the oceanic and continental crust. There exist some other sources of mantle helium, such as diamonds, which their helium signatures can be produced from dilution with old oceanic crust and sediments [Lupton, 1983]. The generation mechanism of Mid Ocean Ridge Basalts (MORB) and Ocean Island Basalts (OIB) is illustrated in Figure 2.5.

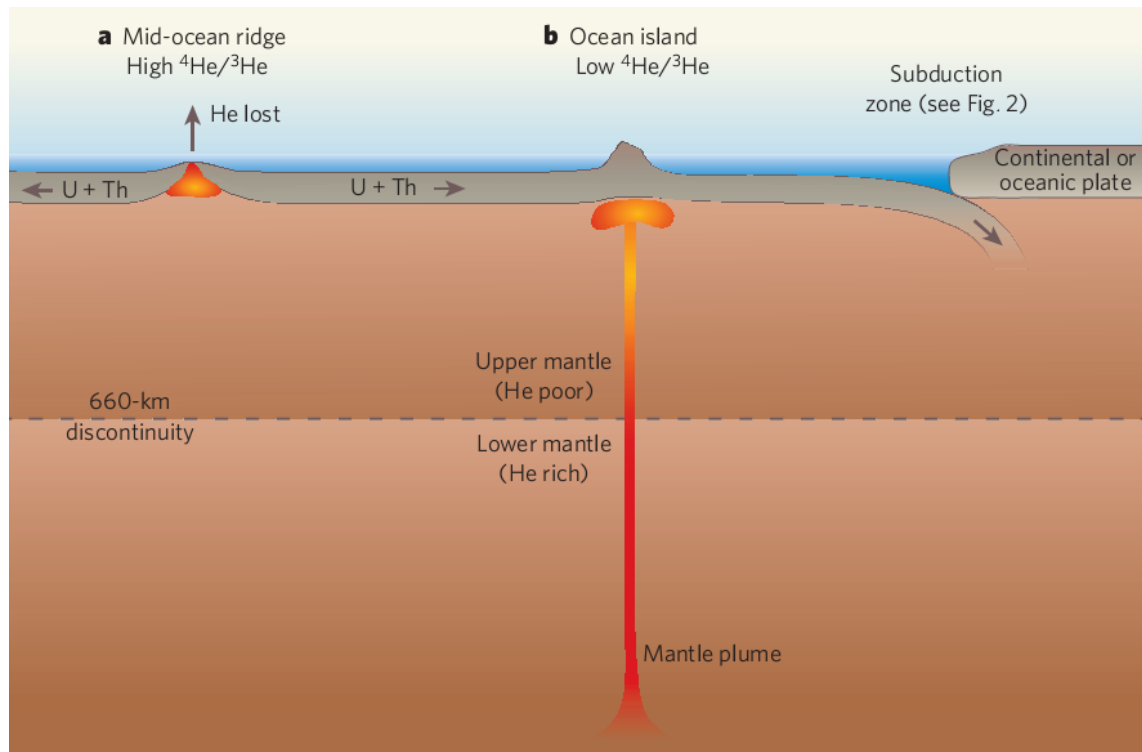


Figure 2.5: The two main sources of mantle derived helium are: (a) Mid Ocean Ridge Basalts (MORB) and (b) Ocean Island Basalts (OIB). Adapted from Elliott [2009].

The characteristic  $^3\text{He}/^4\text{He}$  ratio in MORBs is believed to originate from the upper mantle. Most of the helium released from there escapes to the atmosphere and a small fraction leaks into the oceanic and the continental crust. Melting of the oceanic crust undergoing the continental crust in subduction zones releases helium, which mixes with the local mantle and reduces the  $^3\text{He}/^4\text{He}$  ratios in the magma. In areas that are tectonically active, break up points in the continental crust enable intrusion of magma with a high  $^3\text{He}/^4\text{He}$  ratio and formation of igneous rocks that contain high  $^3\text{He}/^4\text{He}$  ratios as well. Local groundwater, which circulates through layers of such rocks, dissolve the helium, which increases their  $^3\text{He}/^4\text{He}$  ratio.

OIB, also known as “hot spot” appears in the ocean and one of the most famous examples are the islands of Hawaii. The helium in OIB originates from a deeper undepleted part of the mantle and is more enriched than the MORB. The  $^3\text{He}/^4\text{He}$  there varies from  $15 R_a$  to  $30 R_a$  [Lupton, 1983; Graham, 2002], due to a mixture with changing amounts of radiogenic  $^4\text{He}$  in the hot spot zone.

### Separation of the helium components

Helium measured in groundwater can be separated to different components, as depicted in Figure 2.6. Equilibrium and excess air come from the atmosphere, tritiogenic  $^3\text{He}$  is produced from atmospheric tritium and the terrigenous component contains helium from the crust and from the mantle. Two decompositions are discussed here: Separation of terrigenous from atmospheric components (“air correction”) and further separation of mantle derived helium from crustal helium. Tritiogenic component can be neglected for old water.

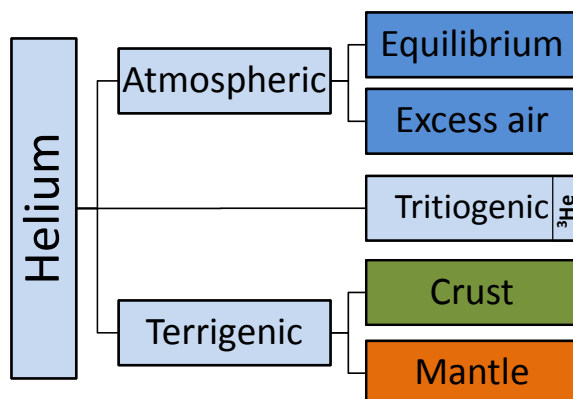


Figure 2.6: Helium components in groundwater. Most of the helium consists of  $^4\text{He}$ . Note that tritiogenic component consists only of  $^3\text{He}$ .

### Air correction

The separation between the atmospheric component and the terrigenous component is based on the assumption that all neon in the sample has an atmospheric source. It is called air correction since it is desired to remove the atmospheric component from the measured

helium isotope concentration. Three different approaches are presented here for derivation of the terrigenous isotope ratio  $R_{ter} = \frac{{}^3\text{He}_{ter}}{{}^4\text{He}_{ter}}$ , all lead to the same results: A graphic approach, isotopes decomposition approach and with the use of the fit results of excess air and equilibrium component (see Section 2.3.2).

#### Graphic approach

Mixing between atmospheric and terrigenous endmembers in groundwater is graphically demonstrated in Figure 2.7. Terrigenous helium consists of a mix of crustal and mantle derived helium.  ${}^3\text{He}/{}^4\text{He}$  ratios in water of a pure terrigenous origin lie on a mixing line between crustal and mantle derived helium endmembers, corresponding to the red line in Figure 2.7. The measured  $\text{Ne}/\text{He}$  ratio is proportional to the amount of helium of atmospheric origin. In this plot, groundwater starts from point “A” on the graph, with

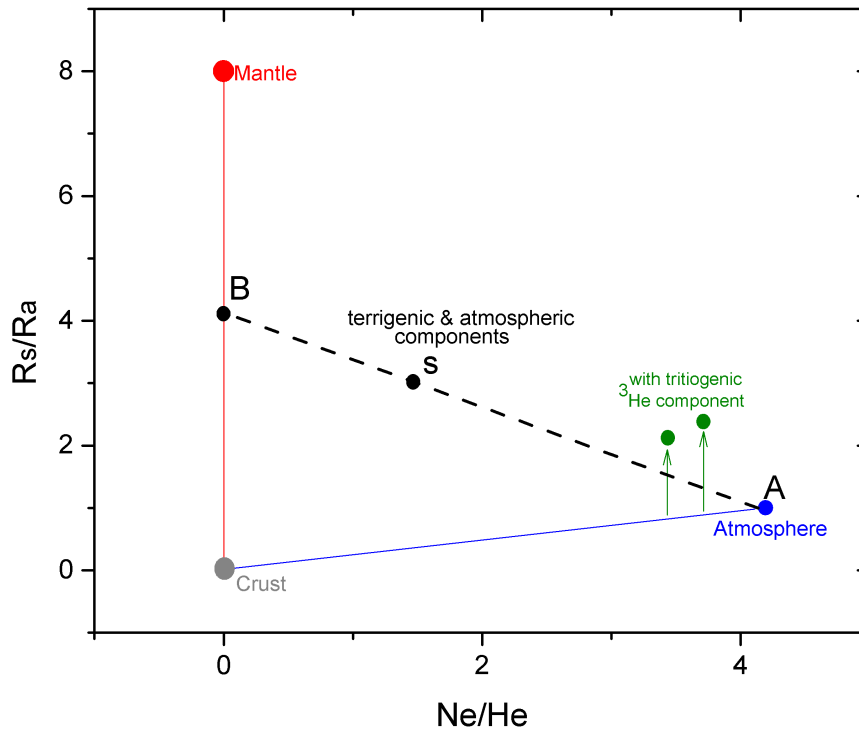


Figure 2.7:  ${}^3\text{He}/{}^4\text{He}$  in a water sample, normalised to the atmospheric ratio  $R_a$ , against neon to helium ratio in the sample. The helium isotope composition in groundwater can be treated as a mixing between three endmembers from three reservoirs: The atmospheric, the crustal and the mantle, which are marked on the plot. The lines represent mixing lines between these endmembers. Blue line: Atmosphere and crust mixing, red line: Crust and mantle mixing. The black dashed line is a general mixing line of a sample “s”, between the atmospheric and terrigenous (mantle+crust) endmembers. The corrected  ${}^3\text{He}/{}^4\text{He}$  ratio, without atmospheric contaminations is found where the dashed mixing line meets the crust mantle mixing line (point “B”).

AEW composition, with  $(Ne/He)_{AEW} \approx 4.2$  for water temperature of about 17°C and  $R_s/R_a \approx 1$ . After loosing contact with air, mixing with terrigenic helium takes place, thus additional helium from the crust and mantle is incorporated in the water, moving the water towards point “B” with  $Ne/He=0$ , as it gets older [Sano and Wakita, 1988].

Consider an arbitrary sample, marked as “s” in Figure 2.7. Assuming all neon in the sample is of atmospheric source, the terrigenic  $^3He/^4He$  component of the sample is the intercept of the mixing line from the atmosphere “A” to the sample “s”, marked as “B”. This is found here by calculating the equation of the line A–B. The general equation of this mixing line is:

$$y = mx + n \quad (2.23)$$

The equation of the line can be found from points “A” and “s”, each has known coordinates:

$$[x_A, y_A] = \left[ \left( \frac{Ne}{He} \right)_a, 1 \right] \quad (2.24)$$

$$[x_s, y_s] = \left[ \left( \frac{Ne}{He} \right)_s, \frac{R_s}{R_a} \right] \quad (2.25)$$

The slope of the line is:

$$m = \frac{\frac{R_s}{R_a} - 1}{\left( \frac{Ne}{He} \right)_s - \left( \frac{Ne}{He} \right)_a} \quad (2.26)$$

The intercept is obtained from inserting Equation 2.26 into the line Equation 2.23:

$$y_B = n = \frac{R_{ter}}{R_a} = y_s - mx_s = \frac{x_s y_A - x_A y_s}{x_s - x_A} \quad (2.27)$$

Inserting the coordinates of points “A” and “s” into 2.27 yields the non-contaminated helium component in the sample, normalized to  $R_a$ :

$$\frac{R_{ter}}{R_a} = \frac{\left( \frac{Ne}{He} \right)_s - \left( \frac{Ne}{He} \right)_a \cdot \frac{R_s}{R_a}}{\left( \frac{Ne}{He} \right)_s - \left( \frac{Ne}{He} \right)_a} \quad (2.28)$$

For convenience, an effective He to Ne ratio,  $x$ , is defined as:

$$x \equiv \frac{\left( \frac{Ne}{He} \right)_s}{\left( \frac{Ne}{He} \right)_a} \quad (2.29)$$

Inserting  $x$  into Equation 2.28 yields:

$$R_{ter} \equiv R_{corr} = \frac{R_s - x \cdot R_a}{1 - x} \quad (2.30)$$

#### Isotopes decomposition approach

If the tritogenic helium component can be neglected, a sample consists only of atmospheric and terrigenic components:

$$^3He_s = ^3He_a + ^3He_{ter} \quad (2.31)$$

$$^4He_s = ^4He_a + ^4He_{ter} \quad (2.32)$$

The isotopic ratio in the sample is:

$$\begin{aligned} R_s &= \frac{{}^3\text{He}_s}{{}^4\text{He}_s} = \frac{{}^3\text{He}_a + {}^3\text{He}_{ter}}{{}^4\text{He}_s} = \frac{R_a \cdot {}^4\text{He}_a + R_{ter} \cdot {}^4\text{He}_{ter}}{{}^4\text{He}_s} = \\ &= R_a \cdot \frac{{}^4\text{He}_a}{{}^4\text{He}_s} + R_{ter} \cdot \frac{{}^4\text{He}_{ter}}{{}^4\text{He}_s} \end{aligned} \quad (2.33)$$

Setting  $x \equiv \frac{{}^4\text{He}_a}{{}^4\text{He}_s}$  yields:

$$R_s = R_a \cdot x + R_{ter} \cdot (1 - x) \quad (2.34)$$

Extracting the terrigenous component gives:

$$R_{ter} = \frac{R_s - R_a \cdot x}{1 - x} \quad (2.35)$$

Assuming that all neon in the sample is from an atmospheric source and having in mind that  $[\text{He}] \approx [{}^4\text{He}]$ ,  $x$  can be written as:

$$\begin{aligned} x &\equiv \frac{{}^4\text{He}_a}{{}^4\text{He}_s} = \frac{{}^4\text{He}_a}{\text{Ne}_a} \cdot \frac{\text{Ne}_a}{{}^4\text{He}_s} = \\ &= \left( \frac{\text{He}}{\text{Ne}} \right)_a \cdot \left( \frac{\text{Ne}}{\text{He}} \right)_s = \\ &= \frac{\left( \frac{\text{Ne}}{\text{He}} \right)_s}{\left( \frac{\text{Ne}}{\text{He}} \right)_a} \end{aligned} \quad (2.36)$$

The parameter  $x$  is calculated from the measured  $\left( \frac{\text{Ne}}{\text{He}} \right)_s \cdot \left( \frac{\text{Ne}}{\text{He}} \right)_a \approx 4.1939$  is taken as the ratio in [AEW](#) for a water temperature of 17 °C.

Using the excess air fitting results:

The atmospheric component of helium is fitted for each sample, as described in sections [2.3](#) and [4.2](#). This component corresponds to the individual fitted [NGT](#) of each sample, therefore should be more reliable than the theoretic values used in the graphic and the decomposition approaches.

Similar to the decomposition approach, it is assumed that a groundwater sample contains atmospheric and terrigenous components, the corrected isotopes concentrations are then:

$${}^3\text{He}_{ter} = {}^3\text{He}_s - {}^3\text{He}_{atm}(CE) \quad (2.37)$$

$${}^4\text{He}_{ter} = {}^4\text{He}_s - {}^4\text{He}_{atm}(CE) \quad (2.38)$$

The terrigenous helium component ratio is simply the fractionation ratio  $R_{ter} = \frac{{}^3\text{He}_{ter}}{{}^4\text{He}_{ter}}$ .

### Atmospheric, crustal and mantle derived helium components

The following decomposition continues the air correction, separating the terrigenous helium component to crustal and mantle derived helium, which are shown in [Figure 2.6](#). The separation can be derived from a mixing model between atmospheric, crustal and mantle derived helium endmembers. [Aeschbach-Hertig \[2005\]](#) derived such a decomposition for

two components, which is expanded here to three components. The  ${}^3\text{He}/{}^4\text{He}$  ratio of a sample,  $R_s$ , can be written as:

$$R_s = \frac{{}^3\text{He}_s}{{}^4\text{He}_s} = \frac{{}^3\text{He}_a + {}^3\text{He}_m + {}^3\text{He}_c}{{}^4\text{He}_s} \quad (2.39)$$

The letters “a”, “m” and “c” refer to the atmosphere, mantle and crust, respectively. The average  ${}^3\text{He}/{}^4\text{He}$  ratios of the three reservoirs from Section 2.4 are summarized in Table 2.1 and inserted into Equation 2.39:

$$R_s = \frac{{}^4\text{He}_a \cdot R_a + {}^4\text{He}_m \cdot R_m + {}^4\text{He}_c \cdot R_c}{{}^4\text{He}_s} = {}^4A R_a + {}^4M R_m + {}^4C R_c \quad (2.40)$$

With the atmospheric, mantle and crustal  ${}^4\text{He}$  components:

$${}^4A = \frac{{}^4\text{He}_a}{{}^4\text{He}_s}; \quad {}^4M = \frac{{}^4\text{He}_m}{{}^4\text{He}_s}; \quad {}^4C = \frac{{}^4\text{He}_c}{{}^4\text{He}_s} \quad (2.41)$$

The relative parts of the  ${}^3\text{He}$  components can be calculated from 2.41 and using the  ${}^3\text{He}/{}^4\text{He}$  ratio of each reservoir from Table 2.1. For example, the atmospheric component reads:

$${}^3A = \frac{{}^3\text{He}_a}{{}^3\text{He}_s} = \frac{{}^4\text{He}_a \cdot R_a}{{}^4\text{He}_s \cdot R_s} = {}^4A \frac{R_a}{R_s} \quad (2.42)$$

The other two components can be calculated in the same way. It is clear from Equation 2.40 that the sum of the components is 1:

$${}^4A + {}^4M + {}^4C = 1 \quad (2.43)$$

Equation 2.43 can be written as:  ${}^4C = 1 - {}^4M - {}^4A$ . Inserting it into Equation 2.40 and solving for  ${}^4M$  yields:

$${}^4M = \frac{(R_s - R_c) - {}^4A \cdot (R_a - R_c)}{R_m - R_c} \quad (2.44)$$

where  $R_s$  is the measured  ${}^3\text{He}/{}^4\text{He}$  ratio and  $R_a$ ,  $R_m$  and  $R_c$  are the  ${}^3\text{He}/{}^4\text{He}$  ratios of the atmosphere, mantle and crust, respectively and are given in Table 2.1.  ${}^4C$  is then calculated from Equation 2.43 and  ${}^3A$ ,  ${}^3M$  and  ${}^3C$  are calculated using Equation 2.42. It is expected to find high fractions of mantle derived  ${}^3\text{He}$  ( ${}^3M$ ) even in groundwater samples that have small  ${}^3\text{He}/{}^4\text{He}$  ratios, due to the different characteristics of the atmosphere, crust and mantle, regarding their helium  ${}^3\text{He}/{}^4\text{He}$  ratios [Aeschbach-Hertig, 2005]. It is generally the case that most of the terrigenous  ${}^3\text{He}$  originates from the mantle, therefore it is useful to compare only the fractions of atmospheric, crustal and mantle  ${}^4\text{He}$ , namely  ${}^4A$ ,  ${}^4C$  and  ${}^4M$ , which sum up to approximately the total helium concentration in the water ( $[{}^4\text{He}] \approx [\text{He}]$ ).

This three components mixing model is connected to the air correction by the parameter  ${}^4A$ , which is exactly  $x$ , defined by the air correction (Equation 2.29).

Table 2.1: Average isotopic fractionations ( $^3\text{He}/^4\text{He}$ ) of the main three reservoirs of helium in groundwater from section 2.4.

$R_a$	$R_c$	$R_m$
1.384E-06	2.000E-08	1.000E-05

### 2.4.2 $\text{CO}_2$ and $\delta^{13}\text{C}$

$\text{CO}_2$  is one of the major volatiles that are still escaping from the mantle. According to Griesshaber and Oxburgh [1992]  $\text{CO}_2$  in gas phase is the main carrier of mantle derived  $^3\text{He}$ . A ratio of  $\text{CO}_2/^3\text{He} = 2 \cdot 10^9$  was measured for the upper mantle in ocean ridge basalts [Marty and Jambon, 1987]. The ratio of  $\text{CO}_2/^4\text{He}$  in the mantle is  $1 \cdot 10^4$  and for continental gases it depends on the production rate of radiogenic  $^4\text{He}$  from U and Th, thus decreasing with time, as the amount of  $^4\text{He}$  increases. If fluids from the mantle manage to rise through the crust and pass it without any contamination or fractionation they should have ratios of  $\text{CO}_2/^3\text{He}$  and  $\text{CO}_2/^4\text{He}$  that are similar to the ratios in the mantle [Griesshaber and Oxburgh, 1992 and Sano and Marty, 1995]. This however does not happen in the reality.

Groundwater usually contains a mixing of  $\text{CO}_2$  from different reservoirs, where different processes occur and lead to fractionation of the carbon isotopes (see Figure 2.8). Each source has a typical  $\delta^{13}\text{C}$  signature, as shown in Figure 2.8. According to Hoefs [2009] and Sano and Marty [1995] the main carbon sources on Earth are marine limestone that contain carbonate, with  $-2\text{‰} < \delta^{13}\text{C} < 2\text{‰}$  and sediments that contain biogenic organic carbon and have a signature of  $-40\text{‰} < \delta^{13}\text{C} < -20\text{‰}$ . According to Griesshaber and Oxburgh [1992],  $\delta^{13}\text{C}$  between  $-5\text{‰}$  to  $-8\text{‰}$  indicates mantle derived  $\text{CO}_2$ . Other studies suggest similar ranges, e.g. Barnes et al. [1978] (cited by O’Nions and Oxburgh [1988]) who state a range of  $\delta^{13}\text{C}$  between  $-4\text{‰}$  to  $-6\text{‰}$  and Sano and Marty [1995] who suggest  $-5\text{‰} < \delta^{13}\text{C} < -8\text{‰}$ . O’Nions and Oxburgh [1988] analysed gases with a mantle signature of  $\delta^{13}\text{C}$  and compared their  $^3\text{He}/^4\text{He}$  ratios with their  $\text{CO}_2/^3\text{He}$  ratios. Some of the gases had higher  $^3\text{He}/^4\text{He}$ , corresponding to a big mantle component, but others had lower  $^3\text{He}/^4\text{He}$  ratios, therefore the  $\text{CO}_2$  in these samples is not likely to come from the mantle, due to no correlation between the mantle isotope signature of  $\delta^{13}\text{C}$  and mantle derived helium.

It is not simple to attribute the  $\delta^{13}\text{C}$  signature to mantle derived carbon due to overlaps with isotopic signatures of other sources. Groundwater, for instance, has a signature of  $-20\text{‰} < \delta^{13}\text{C} < 0\text{‰}$ , due to multiple sources of  $\text{CO}_2$  there. Moreover, carbon in the crust, which was originally escaping from the mantle, has gone through different fractionation processes, that changed its isotopic composition and lead to the different isotopic signatures, thus making it difficult to identify  $\text{CO}_2$  of a mantle origin.

Sano and Marty [1995] introduced a mixing model to determine the nature of  $\text{CO}_2$  volatiles in hydrothermal waters, combining the  $\delta^{13}\text{C}$  and  $\text{CO}_2/^3\text{He}$  from  $\text{CO}_2$  in a gas phase. The idea is a three component mixing with endmembers from the upper mantle, marine limestone (carbonate) and sediments, marked as  $M$ ,  $L$  and  $S$ , respectively. The resulting

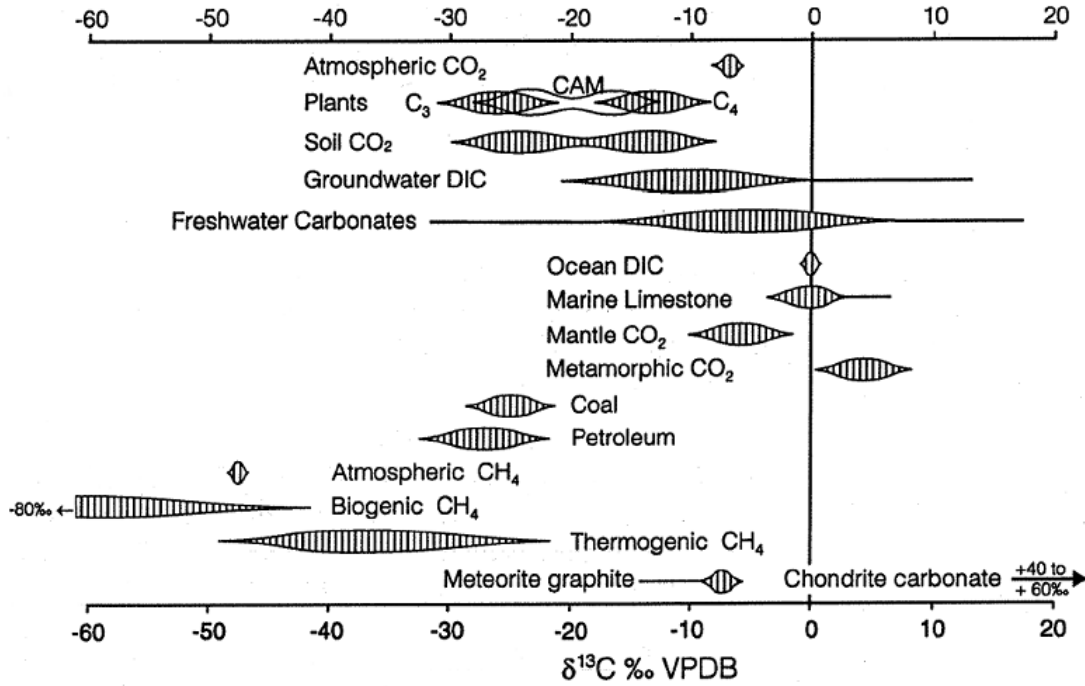


Figure 2.8: Typical  $\delta^{13}\text{C}$  isotopic signatures of different sources and as a result of different processes, adapted from [Clark and Fritz \[1997\]](#). Notice the overlap of the different sources, which makes it difficult to indicate the origin of  $\text{CO}_2$  in groundwater.

mixing equations can be written as following:

$$R_O = R_M M + R_L L + R_S S \quad (2.45)$$

$$\frac{1}{(\text{CO}_2/{}^3\text{He})_O} = \frac{M}{(\text{CO}_2/{}^3\text{He})_M} + \frac{L}{(\text{CO}_2/{}^3\text{He})_L} + \frac{S}{(\text{CO}_2/{}^3\text{He})_S} \quad (2.46)$$

$$M + L + S = 1 \quad (2.47)$$

$M$ ,  $L$  and  $S$  are the fractions of the mantle, limestone and sediment derived  $\text{CO}_2$  in the sample.  $R_M$ ,  $R_L$ ,  $R_S$  and  $R_O$  are the isotopic ratios  $^{13}\text{C}/^{12}\text{C}$ , of the mantle, limestone and sediment endmembers and the measured (“Observed”) isotope ratio of the sample, determined from  $\delta^{13}\text{C}$  and the PDB standard for each of the above fractionation ratios ( $i$ ):

$$R_{PDB} = 0.0112372 \quad (2.48)$$

$$R_i = \frac{\delta^{13}\text{C}_i \cdot R_{PDB}}{1000} + R_{PDB} \quad (2.49)$$

Solving Equations 2.45, 2.46, 2.47 yields the mantle derived  $\text{CO}_2$  component:

$$M = \frac{\frac{1}{(\text{CO}_2/{}^3\text{He})_o} - \frac{1}{(\text{CO}_2/{}^3\text{He})_s}}{\frac{1}{(\text{CO}_2/{}^3\text{He})_m} - \frac{1}{(\text{CO}_2/{}^3\text{He})_s}} \quad (2.50)$$

Table 2.2: Isotopic signatures of carbon and  $\text{CO}_2/{}^3\text{He}$  for mantle derived carbon (**M**), marine carbonate from limestone (**L**) and carbon from sediments (**S**). They are used for a three component mixing model following [Sano and Marty \[1995\]](#). See text for further information.

	<b>M</b>	<b>L</b>	<b>S</b>
$\delta^{13}\text{C}$ [‰]	$-6.5 \pm 2$	$0 \pm 2$	$-30 \pm 10$
$\text{R} = {}^{13}\text{C}/{}^{12}\text{C}$	1.1164E-02	1.1237E-02	1.0900E-02
$\text{CO}_2/{}^3\text{He}$	$1.5 \cdot 10^9$	$1 \cdot 10^{13}$	$1 \cdot 10^{13}$

### 2.4.3 Stable isotopes: $\delta^{18}\text{O}$ and $\delta^2\text{H}$

Precipitation from all over the world show a strong correlation in their stable isotopes composition. The relationship between their  $\delta^{18}\text{O}$  and  $\delta^2\text{H}$  levels is according to the following Equation [[Craig, 1961a](#)]:

$$\delta^2\text{H} = 8 \cdot \delta^{18}\text{O} + 10 \text{‰} \quad (2.51)$$

$\delta^{18}\text{O}$  and  $\delta^2\text{H}$  are given in [‰] and can be derived from the ratios  ${}^{18}\text{O}/{}^{16}\text{O}$  and  ${}^2\text{H}/{}^1\text{H}$  respectively (see appendix [A.3](#)). The line in Equation [2.51](#) is called the [Global Meteoric Water Line \(GMWL\)](#) and is plotted in [Figure 2.9](#). The isotopic composition of ocean water is defined as the reference “Standard Mean Ocean Water” (SMOW), so that  $\delta^{18}\text{O}_{\text{SMOW}} = \delta^2\text{H}_{\text{SMOW}} = 0\text{‰}$  [[Craig, 1961b](#)]. The main origin of precipitation is the ocean, where massive evaporation takes place. However, the [GMWL](#) has an intercept of  $+10 \text{‰}$  and not  $0 \text{‰}$ . This is called “Deuterium excess”, often abbreviated to “D-excess”. The water vapour above the ocean is more enriched in deuterium relative to the ocean water due to non-equilibrium fractionation during the initial evaporation.

The composition of stable isotopes in precipitation varies in different areas and is affected by the temperature and relative humidity. In warmer areas, evaporation of part of the precipitation can occur, causing enrichment in deuterium ([Fig 2.9](#)). There is also an elevation effect, in which precipitation falling on mountains in higher altitudes is more depleted due to enhanced rain-out there, as a result of decrease in the water vapour saturation pressure. There are other factors that affect on the isotopic composition of precipitation, but they are beyond the scope of this work.

The local meteoric water line for Israel is taken as the [Eastern Mediterranean Meteoric Water Line \(EMWL\)](#) from [Gat and Carmi \[1970\]](#) (cited by [Gat and Dansgaard \[1972\]](#)):

$$\delta^2\text{H} = 8 \cdot \delta^{18}\text{O} + 22 \text{‰} \quad (2.52)$$

The [EMWL](#) has the same slope as the [GMWL](#) but an enhanced D-excess, due to a stronger evaporation takes place in the Mediterranean Meer, relatively to the world wide average and due to its almost completely isolation from the Atlantic Ocean and therefore no isotope exchange. According to [Gat et al., 1969](#) and [Gat and Carmi, 1970](#), the local  $\delta^{18}\text{O}$  ranges from  $-7.5 \text{‰}$  to  $-4.5 \text{‰}$ .

Groundwater which originates from precipitation, also called meteoric water, can be expected to have a stable isotopes composition similar to that of local precipitation. For

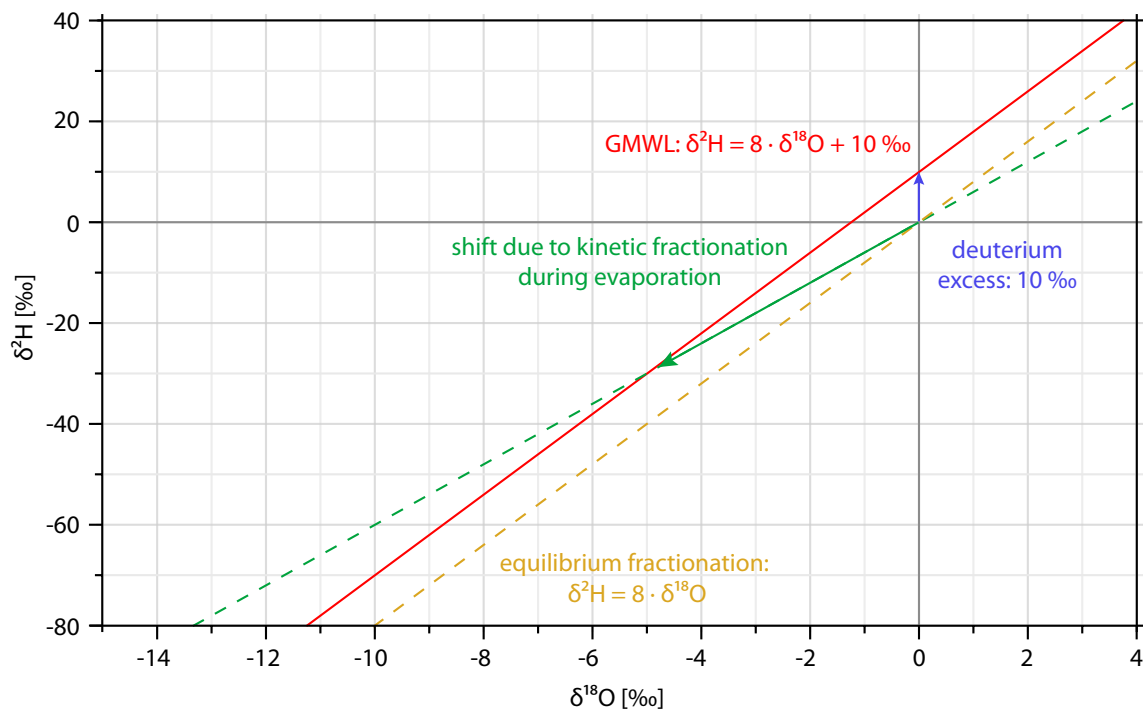


Figure 2.9: Relationship between  $\delta^{18}\text{O}$  and  $\delta^2\text{H}$  in global precipitation, given by the GMWL. Adapted from Bröder [2011].

example, groundwater formed in mountains is depleted in stable isotopes relative to groundwater from lower altitudes, due to the altitude effect mentioned before. Changes in the isotopic composition relative to the composition of local precipitation may be a result of fractionation processes in the ground, therefore stable isotopes can be used as tracers for interaction of groundwater with its surroundings.

Thermal waters, in some cases, are enriched in  $\delta^{18}\text{O}$ , due to interactions with crustal rocks at temperatures higher than  $100\text{ }^\circ\text{C}$ , which cause exchange of  $^{18}\text{O}$  [Hoefs, 2009]. The enrichment is seen only in  $\delta^{18}\text{O}$ , since  $^2\text{H}$  is not contained in minerals. High temperatures, leading to  $\delta^{18}\text{O}$  enrichment in groundwater may be a result of heat fluxes from the mantle. Therefore, stable isotopes can be used as tracers of heat transfer from the mantle to the crust, which can sometimes be a potential source of geothermal energy. However, Giggerbach [1992] analysed volcanic vapour discharges from volcanic systems with high temperatures, so called andesitic water, where fractionation and a deuterium shift take place due to evaporation. He indicated that the detection of this shift is not simple in case of dilution with local groundwater, which is the case for hot springs.

## 3 The Dead Sea Transform

This section reviews the main geographic, tectonic, geological and hydrological settings of the Dead Sea Transform with emphasis on the Israeli side, where the water samples of this thesis are taken from. Many of the geological structures in the Dead Sea Transform, such as basins and rock formations, are named after cities or places that are located in the surroundings. Hence, it is important for the reader to have a general orientation of Israel, especially the eastern part of the country, where the Dead Sea Transform lies. The names of the places mentioned in this section are marked on the map of Israel in Figure A.1. Many studies have been done about the different aspects of the Dead Sea Transform. A major part of this section bases on Horowitz, 2001 and Hoetzel, 2009.

### 3.1 Geographic setting

The Dead Sea Transform was formed during the Late Cenozoic as a result of the break up of the Arabian–African continent. It is a segment of a bigger rift system, called the Levant Rift, which is more than 1000 km long. The Levant Rift is divided into three segments: The Jordan Rift in the south, El Gharb Kara-Su Rift in the north and the Lebanese Fault in between. The East Anatolian Fault and the Red Sea are the borders of the Levant Rift to the north and south, respectively (Figure 3.1).

The Jordan Rift Valley is a 350 km long, narrow and north–south oriented valley on the border between the state of Israel and the kingdom of Jordan. The topography of both sides of the Jordan Rift Valley is asymmetric, as a result of a slip-strike fault. The Israeli side extends from the Hula Valley in the north to the northern Red Sea in the south. It is composed of a series of basins, that are bounded by large normal faults, which cause the floor of the basins to sink and the margins to reach up to a height of thousands of meters [Picard, 1987 ; Mart, 1991 and Horowitz, 2001].

The climate in the Jordan Rift Valley is of Mediterranean type in the north and semi arid to arid in the south, with warm and dry summers and mild winters. The rain time is from September to April.

The Israeli part of the Dead Sea Transform can be divided into regions of different climate and geography. Horowitz [2001] suggests a division into four main parts, from north to south:

1. **The northern part** extends from the borders between Israel–Lebanon and Israel–Syria to the southern side of Lake Kinneret. There are two main surface water bodies in this region: the Hula Lake and Lake Kinneret.
2. **The central part** lies between Lake Kinneret and the Dead Sea.
3. **The Dead Sea area** is located in the Judah Desert and is the lowest place on Earth (today about  $-427$  m, according to data of the Israeli Meteorological Service). The

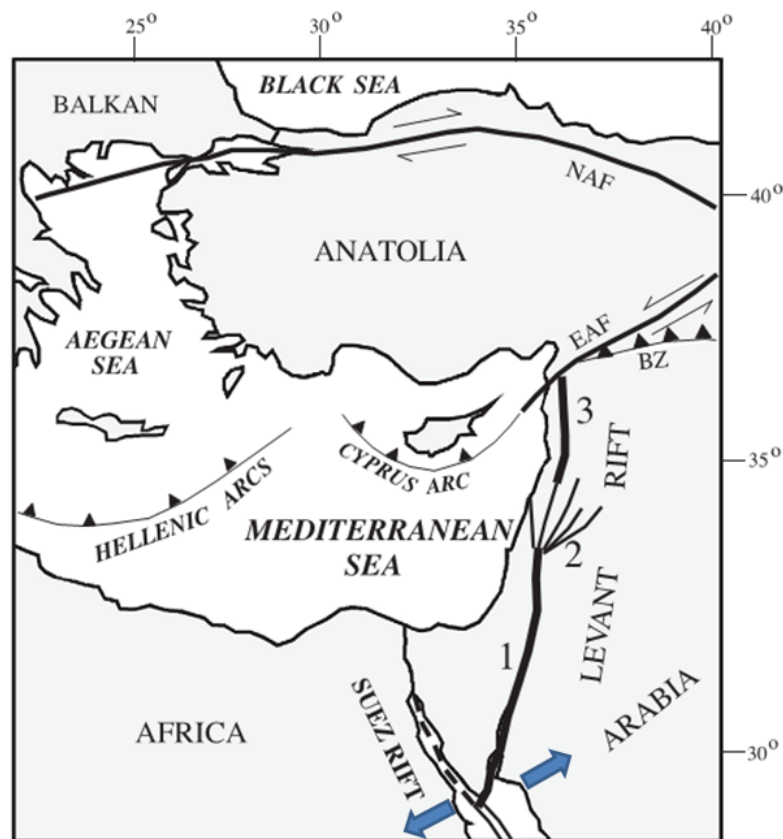


Figure 3.1: Tectonic map of the Levant Rift and the area, from Mart et al. [2005].

water level keeps going down due to human activity and massive evaporation. Thus, the area of the surface sea is constantly being reduced.

4. **The Arava Valley** extends from the Dead Sea to the Gulf of Aqaba, also called the Gulf of Eilat, named after the Jordanian and Israeli cities on the tip of the gulf. Since Arava Valley is located on the eastern part of the Negev Desert it is characterized with high temperatures and low precipitation.

### 3.2 Tectonic setting

The Dead Sea Transform connects the Red Sea, which is a spreading zone, with the Taurus–Zagros Mountains in Turkey, where continental subduction takes place [Freund, 1965 and Wilson, 1965]. The tectonic structure of it consists mostly of faults [Quennell, 1956, 1959]. According to Garfunkel et al., 1981 and Horowitz, 2001 it is considered to be a transform on the border between the African Plate and the Arabian Plate, with a 105 km long horizontal displacement [Quennell, 1959 ; Freund, 1965 ; R., 1970 and Freund et al., 1970]. It is called a transform fault because it is formed as a result of the movement of both plates away from each other, as depicted in Figure 3.1. According to Bayer et al. [1988], the displacement has began since the Oligocene–Miocene or since Mid–Miocene. From seismic and heat flow studies it is known that deformation still takes place along the Dead Sea Transform [Horowitz, 2001]. According to Garfunkel et al. [1981] the present average slip rate of the lateral motion is 0.7–1.0 cm/a. A more recent slip rate of 0.4–0.5 cm/a is

found by Gomez et al. [2007].

The rifting process and the lateral slip have led to formation of a pull-apart basins chain, as explained by Garfunkel et al. [1981]. A pull apart basin is formed as a result of a lateral motion of a fault, as illustrated in Figure 3.2. Refraction data and gravity anomalies indicate that the southern basins in the Dead Sea Transform are deeper than the northern ones [Horowitz, 2001]. The sediment fill in the southern basins extends up to 14 km before the basement is reached. The fill depth in the northern basin is 6–7 km. The main basins or segments along the Israeli side of Dead Sea Transform, described by Horowitz [2001], are from north to south: The Hula depression, Bet She’an – Lake Kinneret depression, the Dead Sea – Bet She’an segment and the Dead Sea – Arava depression.

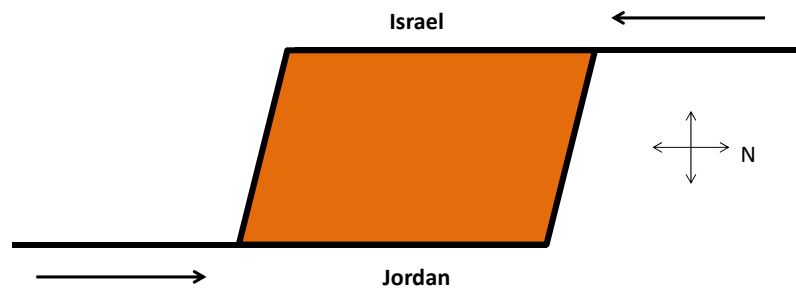


Figure 3.2: The Dead Sea Transform is a chain of pull apart basins, which are formed as a result of a left lateral motion slip of the fault, marked with arrows. Israel and Jordan are indicated for orientation.

The northernmost basin in the Dead Sea Transform is the Hula basin. It is bordered to the east by the Jordan River gorge and the Golan Heights, to the west by the mountains of Galilee and to the south by the Korazim block, which makes a topographic separation of the Hula Basin from the Kinneret basin. The Hula basin is shallow, only 5 km of sedimental fill, with faults on both east and west margins.

Southern from the Hula basin is the Bet She’an – Lake Kinneret Depression, which is under sea level and forms the Kinneret basin. Some active faults still exist in the margins of the lake.

The Dead Sea – Bet She’an segment begins at around the town of Bet She’an, south of Lake Kinneret and extends southward, down to the Dead Sea. The width of the valley is about 8 km around Bet She’an in the north and increases to 18 km around Jericho in the south. The valley is broadening a few kilometres southern of Bet She’an and connects the Yizrael Valley from the west. The slopes of this segment become more steep to the south, connecting to the high slopes of the margins of the Dead Sea basin.

The Dead Sea – Arava is the most prominent and seismically active basin in the Dead Sea Transform. It begins from about 5 km north to the Dead Sea and extends over 130 km to the south, down to Gav Ha’Arava. Step faults in the eastern and western margins of the Dead Sea have caused vertical displacements which lead to a depression of the basement. The depression is 7–18 km wide and has relatively steep slopes on both sides.

The thickness of the crust underlying the Dead Sea Transform varies from north to south, as illustrated in Figure 3.3. El-Isa et al., 1987 and Ginzburg et al., 1979 indicate that the crust in the southern Dead Sea Transform is an oceanic crust covered by the continental

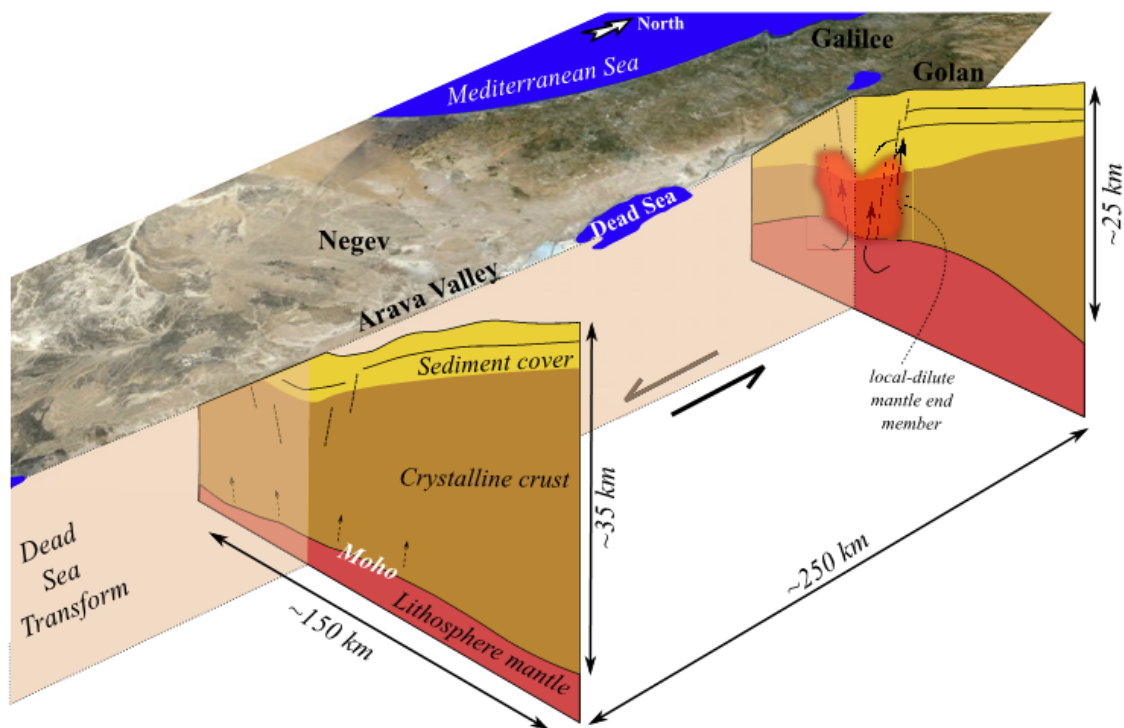


Figure 3.3: Schematic cross sections of the crust underlies the Dead Sea Transform. The thin arrows on the cross sections refer to the process of volatiles upwelling from the mantle. Adapted from [Torfstein et al., 2013]

crust of the Arabo–Nubian Massif and a thick wedge-like layer of Mesozoic and Tertiary sediments, which is up to 35 km thick. Horowitz [2001] indicates different densities of the crust in the north, also supports the existence of two types. The thickness of the crust decreases towards the north and reaches a thickness of about 25 km and has characteristics of a continental crust. For comparison, the crust underlies the south of Israel and the Negev desert is 40 km thick.

### 3.3 Hydrogeology

#### Aquifers

The stratigraphic profile of the Jordan Rift Valley comprises of different layers and rock formations starting from Precambrian time. The groundwater originates from regional calcareous and basaltic aquifers, as shown in the stratigraphic sequence in Figure 3.4. The main aquifers described by Hoetzl [2009] are summarized here.

The oldest main aquifer is the Ram Aquifer, consisting of Precambrian sandstone, limestone and siltstone. Above Ram lies the Zarqa aquifer from Permo–Triassic age. This group aquifer consists of limestone, argillaceous rocks with shales, dolomite and silt stone. It lies in the vicinity of Zarqa Ma'in and Hisban area in Jordan and has a thickness between 300 m to 350 m. Above Zarka lies the Kurnub sandstone aquifer, which is from lower Cretaceous age and is about 220–320 m thick. The sandstones of Kurnub are connected with the Zarqa and Ram aquifer. They form an interconnected aquifer complex that is called "Lower Aquifer Sandstone Complex" [Hoetzl, 2009]. Some parts of the interconnected

aquifer consist of marl and silt, separating the different parts from each other.

Above the lower complex aquifer lies a group of aquifers called the Upper Cretaceous aquifer. It consists of the regional aquifers that lie in the eastern and western sides of the Jordan Rift Valley. The Judea group lies under the Judea dessert and Samaria area on the western side of the Jordan Rift Valley. The thickness of the aquifer is 800–850 m and it comprises of limestone and dolomite.

The youngest group of aquifers is called the Dead Sea Group of the Jordan Valley Deposits. The stone formations in this group are from the Pleistocene–Holocene age. This group subdivides to local aquifers on both sides of the Dead Sea Transform and consists of gravel and sandstones.

#### **Water salinity**

The water bodies along the Dead Sea Transform vary from brackish to saline. According to [Torfstein et al. \[2013\]](#), the brackish groundwater found in the Arava Valley, originates from the deep Kurnub aquifer and the shallow Arava Formation and the Arava Fill, shown in Figure 3.4. The salinity of the water is coming from mixing with other brines and from dissolution of evaporites and other sediment layers [[Yechieli et al., 1992](#)].

The saline water of the Jordan Rift Valley contains surface and groundwater in the area of Lake Kinneret and the Dead Sea. The salinity of the brines varies from brackish to very high salinities of 400 g/l in the Dead Sea. The Ca-chloride brines formation can be explained by penetration of evaporated sea water to the Dead Sea Transform, followed by interaction of the water with limestone layers and dolomitization. Each of the water bodies has a different Ca-chloride composition, therefore different sedimentation rates of salt [[Starinsky, 1974](#)] (cited by [[Stern, 2010](#)]).

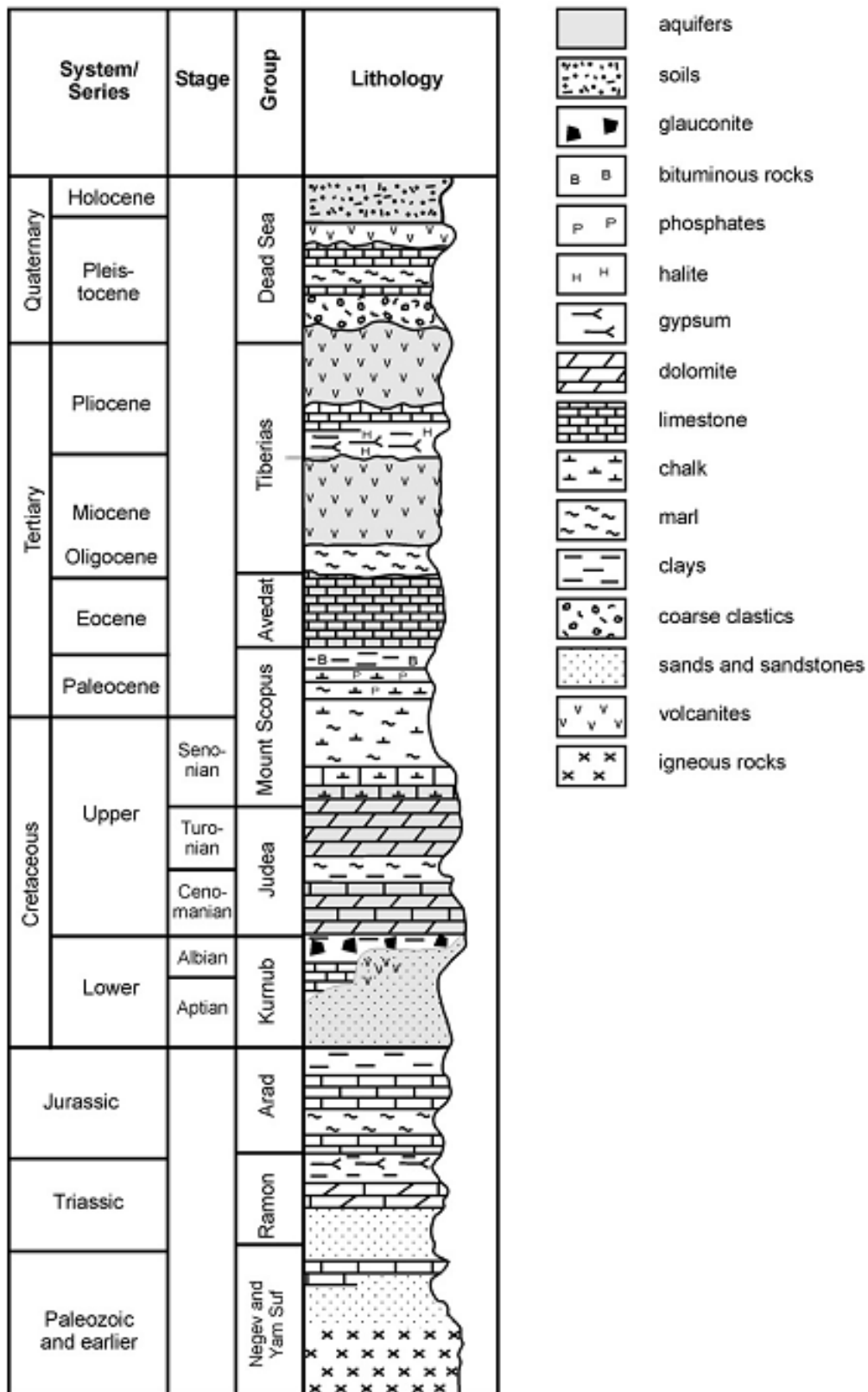


Figure 3.4: Stratigraphic column of Cisjordan, adapted from Möller et al. [2007b].

### 3.4 Sampling sites

A sampling campaign was carried out in December 2012 in Israel. 13 samples from springs and wells were taken at 9 sampling sites along the Dead Sea Transform. Locations and

Table 3.1: General information of the sampling sites in the Israel campaign, December 2012. Note that all the samples except of Shamir and Tzofar are below sea level.

Site*	Region**	Latitude	Longitude	Elv. [m]***	Site type
<b>Shamir</b>	Hula V.	33°10'22'	35°39'50"	245	Well field
<b>Meitzar</b>	Yarmouk V.	32°42'54"	35°41'46"	-90	Well field
<b>Hamat Gader</b>	Yarmouk V.	32°41'03"	35°39'55"	-163	Spring field
<b>Gofra Beach</b>	E. Kinneret	32°48'14"	35°38'32"	-183	Spring
<b>Hamat Tveria</b>	W. Kinneret	32°46'02"	35°33'00"	-183	Spring field
<b>Mineral Beach</b>	Dead Sea	31°32'45"	35°23'47"	-386	Well
<b>Ein Qedem</b>	Dead Sea	31°30'55"	35°23'43"	-404	Spring
<b>Ein Yahav</b>	Arava V.	30°40'32"	35°13'05"	-80	Well field
<b>Tzofar</b>	Arava V.	30°33'13"	35°10'40"	18	Well field

\*The owners of the sites are: Mekorot Israel National Water Co.: Meitzar, Ein Yahav and Tzofar. Mei Golan Water Co.: Shamir. Hamat Gader Resort: Hamat Gader. Gofra Beach: Gofra Beach. Nature and Park Authority: Hamat Tveria. Mineral Beach: Mineral Beach. Ein Qedem has no owner.

\*\*Region abbreviations: V: Valley, E: Eastern and W: Western.

\*\*\*Elevation above sea level in [m].

Table 3.2: Depth, screen and contributing rock layer of the sampled wells. All the wells are artesian, including Mineral, for which the owner could not provide borehole data. Depth corresponds to the depth of the drilling, relative to the surface and screen corresponds to the depth range from which groundwater actually comes.

Site	Depth [m]	Screen [m]	Lithography
<b>Shamir</b>	1,420	1,162–1,420	Limestone
<b>Meitzar 2</b>	807	448–807	Mostly Dolomite
<b>Meitzar 3</b>	336	80–336	Bitumenic Chalk
<b>Ein Yahav 6</b>	904	765–884	Sandstone
<b>Ein Yahav 16</b>	509	255–509	Mostly Limestone
<b>Ein Yahav 116</b>	190	136–171	Flint
<b>Tzofar</b>	1,010	836–1,007	Sandstone

site types are shown in Table 3.1 and Figure 3.5. Information about the sampled wells is given in Table 3.2. The sites differ from each other in the flow rate and their accessibility. Therefore, the sampling process was different from site to site, as described in appendix A.5.



Figure 3.5: Locations of the sampling sites of the Israel campaign, 2012.

## 4 Methods

This chapter describes the necessary sampling, measurement and evaluation methods applied in this study. The following parameters and samples were taken on each site: Water temperature, electrical conductivity, alkalinity, dissolved noble gases, tritium,  $\delta^{13}\text{C}$  and stable isotopes.

### 4.1 Water characteristics

The following water characteristics were measured in each site:

- **Temperature and electrical conductivity:** Measurements were taken with a WTW water probe. The water parameters were noted after their stabilization. According to the manufacturer, the precision of the temperature is  $\pm 0.2^\circ\text{C}$  and the precision of electrical conductivity is  $\pm 1 \mu\text{S}/\text{cm}$  for measured values below  $2 \mu\text{S}/\text{cm}$  and  $\pm 10 \mu\text{S}/\text{cm}$  for values above  $2 \mu\text{S}/\text{cm}$ .
- **Alkalinity:** An alkalinity test kit manufactured by *Salifert*, based on titration was used, with a precision of 0.1 meq/l for alkalinity above 3.9 meq/l and 0.07 meq/l for a smaller alkalinity.

Photos of the sampling are found in the appendix [A.8](#), Figure [A.11](#).

### 4.2 Noble gases: Mass spectrometry

#### 4.2.1 Sampling

As mentioned in Section [2](#), the solubility of noble gases in groundwater depends on the temperature and salinity at the time of equilibration with air. Therefore the sample should be taken as close as possible to the point where the water springs from the ground and the formation of bubbles should be avoided in order to avoid degassing. For the same reason, contact with atmospheric air should be avoided as well. Noble gases are very volatile, therefore a sealed copper tube is used as a container and in order to prevent gas escape and interaction with air. The copper tube is connected from both sides to hoses, as depicted in Figure [A.11](#). It is recommended to use transparent hoses in order to be able to detect and remove air bubbles. The hoses also help to prevent bubbles to form at the sides of the tube. Water should flow freely through the copper tube and fill the hoses. The sampling process slightly changes from site to site, depending on the site type (well or spring), the water pressure and the flow rate at the outflow point. After making sure that no air bubbles are trapped in the water, the copper tube is sealed.

### 4.2.2 Measurement

The noble gas samples were measured using a *GV Instruments* MM5400 sector field mass spectrometer, at the [Institute of Environmental Physics \(IUP\)](#). The distinction of different elements is done by ionization, where different ions move in different curves under magnetic field, due to Lorenz force. The radius of the curves depends on the mass and charge of the ions [[Hoffmann and Stroobant, 2007](#)]:

$$\frac{m}{q} = \frac{B^2 r^2}{2U} \quad (4.1)$$

$m$  is the ion mass,  $q$  is the ion charge,  $B$  is the magnetic field intensity,  $r$  is the radius of the curve and  $U$  is the magnitude of the voltage induced on the ion.

The measurement process lasts a few hours and consists of extraction and separation of the noble gases from the water, followed by detection in the spectrometer itself, as demonstrated in [Figure 4.2](#). A water sample is first connected to an inlet zone under vacuum conditions, where degasification takes place, extracting the dissolved noble gases from the water. According to Henry's law ([Equation 2.2](#)), the solubility depends on the partial pressure of the gas. The partial pressure of a gas decreases in vacuum, thus reducing the solubility, which leads to degasification. A zeolite trap is used to remove water vapour remnants and the rest flows into a cryo trap, where the individual noble gases are separated. The lighter gases (helium and neon) and the heavier gases (argon, krypton and xenon) are cooled down until they freeze and are trapped in different segments of the cryo. The cryo is then heated and desorbs the individual gases based on their melting point, from the lighter to the heavier, in different time intervals. The gas is then cleaned by getter pumps, removing remnants of other gases like nitrogen and is ready to be measured in the spectrometer, where the molecules are ionized, lead through a magnet and detected ([Figure 4.1](#)). Two kinds of detectors are used: An Electron multiplier for small amounts, measures counts per second and a Faraday cup for bigger amounts, which translates the ion current to voltage. The plot of a signal versus atomic mass has a shape of a peak, centered around the atomic mass of the measured isotope, for example, the peak of  $^4\text{He}$  has a maximum around about 4 AMU. The measurement is gas consuming, therefore the signal intensity decreases with time, hence the peak height decreases too.

In order to be able to convert the measured signal to gas amount, gas with a well known composition is measured and used for two kinds of calibrations. The first, called "fastcal" (fast calibration), is done before each measurement in order to determine changes of the spectrometer sensitivity. The second, called "Cal" (air standatd), is an absolute calibration of the whole system, including the preparation zone and the spectrometer itself. The measurement process of a "Cal" is similar to a measurement of a sample, but instead of extraction of gases from a sample, calibration gas is taken from a container and is inserted directly into the cryo trap (see [Figure 4.2](#)). The calibrations have to be regularly performed in order to adapt them to changes of background effects, such as temperature changes in the laboratory.

Other necessary measurements to monitor the system are background measurements, called "blank", where no sample is inserted into the spectrometer and [AEW](#) samples. The later are water samples, taken in the [IUP](#) from an aquarium containing water with known temperature and air pressure. This water stays a few weeks in the aquarium and

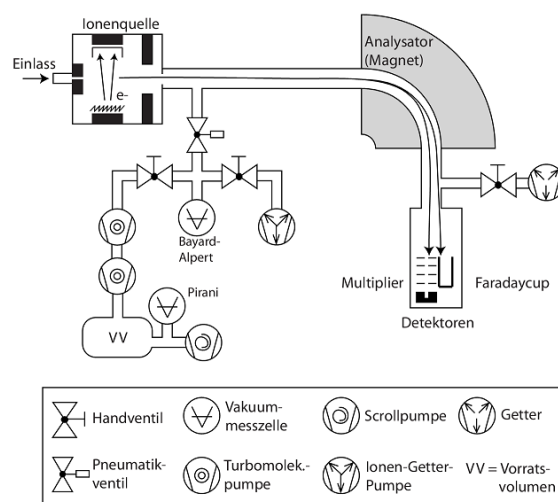


Figure 4.1: Schematic description of MM5400 mass spectrometer, used for noble gas measurements in the IUP, adopted from Friedrich [2007]. Gas molecules are flowing through the inlet and are ionized. The ions change their curve under magnetic field and are detected by one of the two detectors. The distinction between different ions is based on the mass and radius of the curve, following Equation 4.1.

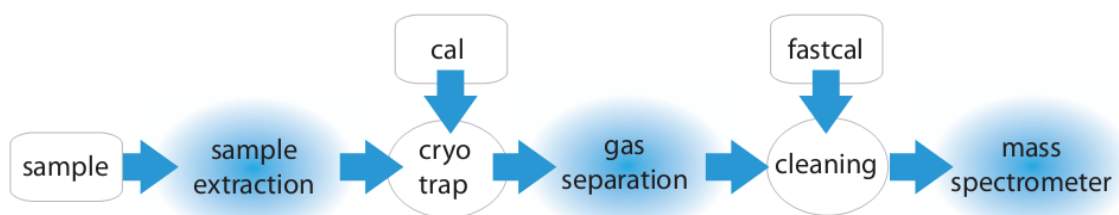


Figure 4.2: Measurement process of the mass spectrometer, modified from Wieser [2011].

exchanges gases with the surrounding air until an equilibrium is reached. The measured noble gas concentrations are compared with the theoretical concentrations.

As of today, eight noble gas isotopes are measured by the mass spectrometer:  $^3\text{He}$ ,  $^4\text{He}$ ,  $^{20}\text{Ne}$ ,  $^{22}\text{Ne}$ ,  $^{36}\text{Ar}$ ,  $^{40}\text{Ar}$ ,  $^{84}\text{Kr}$  and  $^{132}\text{Xe}$ . Further detailed information about the mass spectrometer in the IUP is found in Friedrich, 2007 ; Wieser, 2011 and Kaudse, 2014.

### 4.2.3 Data evaluation

The calculation of gas amount from the measured signal is done by the WuCEM software, developed by Michael Jung from the IUP. The analysis is done by a few steps. On the first step, the measured signal is extrapolated to the time of the gas inlet,  $t = 0$ . The signal amplitudes, measured at different times, are plotted against the time and are fitted, usually with a linear curve. The intercept of the fitted curve is taken as the signal strength at the time of inlet. This is done for the samples and the all the “Cals” and “blanks” that are measured close to the time of the samples measurement and to all the measured isotopes

and their corresponding “fastcals”. On the second step, the measured isotopes signals are corrected with the calibrations and blank measurements. The resulting gas amounts are given in units of [ccSTP], which is the volume (in cubic centimeters) that a given amount of gas occupies as STP: Standard Temperature and Pressure, of  $T_0 = 273.15\text{ K}$  and  $p_0 = 1\text{ atm}$ .

### From gas amount to concentration

The concentration of each isotope is obtained by dividing the amount by the total mass of the water in the sample, measured by weighting the sample before and after the measurement. The concentration of each element is calculated from the concentrations of the isotopes composing it, weighted with their atomic abundance factors. That way, the total element concentration can be calculated only from part of the isotopes, thus it is not required to measure them all. The atomic abundance factors of the isotopes measured in the IUP are listed in Table 4.1 and the calculation is done as follows:

$$[Element] = \frac{\sum_n [Isotope]_n}{\sum_n f_n} = \frac{\sum_n Isotope_n}{m \cdot \sum_n f_n}, \quad (4.2)$$

where [...] marks the concentration of an element or an isotope,  $n$  refers to a single isotope species, i.e.  ${}^4\text{He}$ ,  $f_n$  is the atomic abundance factor and  $m$  is the sample mass.

The total helium concentration is calculated only from  ${}^4\text{He}$ , since the amount of  ${}^3\text{He}$  is negligible:

$$[\text{He}] \simeq [{}^4\text{He}]$$

The concentration of argon is usually calculated as follows:

$$[\text{Ar}] = \frac{[{}^{36}\text{Ar}] + [{}^{40}\text{Ar}]}{0.003364 + 0.996}$$

As explained in Chapter 2, in case the ratio  ${}^{36}\text{Ar}/{}^{40}\text{Ar}$  is smaller than its ratio in the atmosphere, [Ar] is calculated only from  ${}^{36}\text{Ar}$ :

$$[\text{Ar}] = \frac{[{}^{36}\text{Ar}]}{0.003364} \quad (4.3)$$

### NGTs Fitting

The calculated noble gas concentrations can be fitted with one of the excess air models to find the NGT, as explained in the theory chapter. This is done here using Panga, a fitting software developed by Michael Jung. The concentrations are given to the software, as well as water salinity and estimated air pressure at the time of recharge. The software fits the given parameters to one of the excess air models and determines the NGT.

Samples with air contamination or degassing should be treated differently than other samples. Since it can be assumed that neon originates from the atmosphere and since its solubility does not change so much with the temperature, relatively to the other noble gases, it can be used as an indicator of air contamination or degassing. The average neon concentration of air equilibrated water is  $\sim 2 \cdot 10^{-7}\text{ ccSTP/g}$ . Much higher or lower

Table 4.1: Atomic abundance factors of the measured noble gas isotopes from [Kipfer et al. \[2002\]](#).

Isotope	Factor
<b>He3</b>	0.0000014
<b>He4</b>	1.0000000
<b>Ne20</b>	0.9050000
<b>Ne22</b>	0.0923000
<b>Ar36</b>	0.0033640
<b>Ar40</b>	0.9960000
<b>Kr84</b>	0.5700000
<b>Xe132</b>	0.2689000

concentrations indicate excess air or degassing, respectively and may lead to a wrong [NGT](#). A more qualitative way to identify degassing is the parameter  $\Delta\text{Ne}$ , defined as the relative part of excess air derived neon [[Aeschbach-Hertig and Solomon, 2013](#)]:

Fitting results that are not optimal, for example extremely low [NGTs](#) or high uncertainties, can be improved with the help of Monte Carlo simulations [[Jung et al., 2012](#)]. These randomly produce fitting results that distribute with certain expectation value and a statistical deviation. In some cases the Monte Carlo simulations succeed to produce physical results even though the fitting results are not physically reasonable.

## 4.3 Isotopic composition

Samples of tritium,  $^{13}\text{C}$  and stable isotopes are taken in glass bottles. The bottles should be filled with water almost completely, leaving a minimal portion of air for a safe transport.

### 4.3.1 Tritium

Tritium was measured in the tritium laboratory at the [IUP](#), as described by [Grothe \[1992\]](#). 9 ml water is heated to 600 °C and reduced by magnetism to produce  $\text{H}_2$  gas. The gas is then measured in a low counting chamber for 48 hours. This system can detect tritium from 2 TU, therefore results that show smaller amounts can only be qualitatively treated, which is sufficient for this study.

### 4.3.2 $\delta^{13}\text{C}$

During the sampling, before sealing the bottles, one drop of Micropur (Katadyn Products Inc.), which is used to purify water, was added to the water to stop any biological activity and prevent further fractionation.

The measurements were carried out in the carbon laboratory at the [IUP](#). The process consists of extraction of the DIC from the water, followed by a measurement in an accelerated mass spectrometer (AMS). For more information about the extraction line see [Unkel](#),

2006 and Kreuzer, 2007. The  $^{13}\text{C}$  measurement is further described by Wieser [2011]. The precision of the results is 0.03 ‰.

### 4.3.3 Stable isotopes

The stable isotopes were measured with a Picarro L2120-i system by the BGR, the laboratory of the Federal Institute for Geosciences and Natural Resources, in Hannover, Germany. According to the manufacturer, the measurement precision of  $\delta^{18}\text{O}$  is better than 0.1 ‰ and of  $\delta^2\text{H}$  is better than 0.5 ‰.

## 5 Results

This chapter shows and describes the results of the thermal waters sampling in Israel. The results are divided into two sections. The first section deals with noble gas temperatures and the the following sections present the results of helium isotopes in the thermal waters, in connection with other environmental isotopes and noble gases. Measurement uncertainties and errors appear only in tables and are omitted from graphs for clarity.

Thermal waters from 13 wells and springs were sampled along the Dead Sea Transform in Israel in December 2012. The sampling sites spread from the Hula Valley in the north, to the Arava Valley in the south. All locations are marked on the map in Figure 3.5 and described in Table 3.1. Water temperature, electrical conductivity and alkalinity are presented in Table 5.1.

Table 5.1: Water temperature, electrical conductivity and alkalinity. H.Tveria corresponds to Hamat Tveria. The corresponding precisions are: Temperature:  $\pm 2^\circ\text{C}$ , electrical conductivity:  $\pm 10 \mu\text{S/cm}$  and alkalinity: 0.07 meq/l for values under 3.9 meq/l and 0.1 meq/l for higher values.

Sample	T [ $^\circ\text{C}$ ]	E.C [ $\mu\text{S/cm}$ ]	Alkalinity [meq/l]
<b>Gofra</b>	30.8	6840	2.62
<b>Shamir</b>	45.4	1237	3.94
<b>H. Tveria</b>	58.9	37800	2.73
<b>Meitzar 2</b>	65.3	1835	4.68
<b>Meitzar 3</b>	40.2	660	0.79
<b>Makla</b>	48.5	1895	0.56
<b>Balzam</b>	41.7	1393	0.79
<b>Mineral</b>	42.7	148100	1.54
<b>Qedem</b>	43.8	148500	2.73
<b>Yahav 6</b>	43.5	2690	4.62
<b>Yahav 16</b>	35.0	2780	3.30
<b>Yahav 116</b>	31.0	2170	0.90
<b>Tzofar 20</b>	43.3	9630	3.08

Noble gas isotopes of helium, neon, argon, krypton and xenon were measured by the mass spectrometer of the Groundwater and Paleoclimate Research Group at the Institute of Environmental Physics in Heidelberg University. Several samples were collected from each site and the measurements were carried out in three runs. The samples from the first run, which went without significant complications, are used for further analysis. The second and third runs are not included in the analysis due to an electrical blackout during the measurements. Their results are found in Appendix A.7. The measured isotopes concentrations from the first run are listed in Table 5.2. The total amount of each element was calculated from the isotopes composing it, using Equation 4.2 and is shown in Table 5.3. Ein Makla, Hamat Tveria and Ein Qedem have high  $^{36}\text{Ar}/^{40}\text{Ar}$  ratios (see Appendix

Table 5.2: Noble gas isotopes concentrations in thermal waters along the Israeli side of the Dead Sea Transform, in [ccSTP/g].

Sample	$^3\text{He}$	$\Delta^3\text{He}$	$^4\text{He}$	$\Delta^4\text{He}$	$^{20}\text{Ne}$	$\Delta^{20}\text{Ne}$	$^{22}\text{Ne}$	$\Delta^{22}\text{Ne}$
Gofra	3.378E-12	1.426E-13	1.424E-06	8.651E-09	1.256E-07	5.118E-10	1.282E-08	6.088E-11
Shamir	7.963E-12	3.458E-13	2.046E-06	1.054E-08	2.218E-07	9.040E-10	2.268E-08	9.623E-11
Meitzar 3	1.105E-12	4.920E-14	4.614E-07	2.464E-09	1.976E-07	8.297E-10	2.018E-08	9.809E-11
Balzam	1.525E-11	7.722E-13	5.068E-06	3.596E-08	1.612E-07	7.227E-10	1.654E-08	7.747E-11
Meitzar 2	4.328E-11	1.890E-12	1.515E-05	8.904E-08	1.680E-07	6.997E-10	1.720E-08	8.021E-11
Makla	2.501E-11	1.036E-12	9.880E-06	5.963E-08	1.483E-07	6.313E-10	1.520E-08	6.903E-11
Yahav 116	1.241E-12	4.729E-14	2.376E-06	1.234E-08	2.360E-07	1.008E-09	2.412E-08	1.122E-10
Yahav 6	6.204E-12	2.430E-13	9.235E-06	5.569E-08	2.212E-07	9.411E-10	2.266E-08	9.874E-11
Yahav 16	3.670E-12	1.457E-13	6.772E-06	4.224E-08	2.067E-07	8.605E-10	2.111E-08	9.163E-11
Yahav 16	9.174E-12	3.564E-13	1.567E-05	8.123E-08	1.521E-07	6.175E-10	1.560E-08	7.167E-11
Tzofar 20	4.120E-11	1.839E-12	2.826E-05	1.494E-07	9.213E-08	3.843E-10	9.439E-09	5.177E-11
Hamat Tveria	3.322E-14	1.339E-15	2.786E-08	2.840E-10	6.767E-08	2.863E-10	6.918E-09	3.985E-11
Mineral	7.729E-12	2.919E-13	9.132E-06	5.518E-08	3.961E-08	1.774E-10	4.027E-09	3.556E-11
Qedem								
Sample	$^{36}\text{Ar}$	$\Delta^{36}\text{Ar}$	$^{40}\text{Ar}$	$\Delta^{40}\text{Ar}$	$^{84}\text{Kr}$	$\Delta^{84}\text{Kr}$	$^{132}\text{Xe}$	$\Delta^{132}\text{Xe}$
Gofra	9.681E-07	2.385E-08	2.742E-04	6.929E-07	3.675E-08	7.041E-10	2.350E-09	4.718E-11
Shamir	1.254E-06	2.682E-08	3.704E-04	8.924E-07	4.950E-08	8.288E-10	3.227E-09	7.234E-11
Meitzar 3	1.116E-06	2.431E-08	3.339E-04	8.199E-07	4.243E-08	7.542E-10	2.587E-09	4.773E-11
Balzam	1.014E-06	2.465E-08	2.982E-04	7.859E-07	3.897E-08	7.149E-10	2.463E-09	4.945E-11
Meitzar 2	1.303E-06	2.978E-08	3.881E-04	9.090E-07	5.016E-08	8.377E-10	3.132E-09	6.524E-11
Makla	1.030E-06	2.315E-08	3.074E-04	7.652E-07	4.026E-08	7.331E-10	2.506E-09	4.999E-11
Yahav 116	1.111E-06	2.444E-08	3.299E-04	7.887E-07	4.024E-08	7.212E-10	2.511E-09	6.151E-11
Yahav 6	1.172E-06	2.542E-08	3.494E-04	8.350E-07	4.079E-08	7.653E-10	2.444E-09	4.901E-11
Yahav 16	1.082E-06	2.396E-08	3.112E-04	7.544E-07	3.744E-08	7.236E-10	2.354E-09	5.358E-11
Tzofar 20	8.088E-07	1.988E-08	2.449E-04	6.354E-07	2.849E-08	6.296E-10	1.753E-09	3.420E-11
Hamat Tveria	6.494E-07	1.759E-08	2.087E-04	5.846E-07	2.871E-08	6.123E-10	1.868E-09	3.785E-11
Mineral	3.009E-07	1.162E-08	8.424E-05	3.527E-07	9.614E-09	4.527E-10	5.142E-10	1.465E-11
Qedem	2.054E-07	2.048E-08	1.060E-04	3.789E-07	1.366E-08	4.590E-10	8.737E-10	2.157E-11

Table 5.3: Elemental noble gas concentrations in thermal waters along the Israeli side of the Dead Sea Transform, in [ccSTP/g]. H.Tveria refers to the spring of Hamat Tveria. Argon, which was used in this study only for NGT determination, is corrected to atmospheric component, as explained in sections 2.2 and 4.2.

Sample	He	$\Delta$ He	Ne	$\Delta$ Ne	Ar	$\Delta$ Ar	Kr	$\Delta$ Kr	Xe	$\Delta$ Xe
Gofra	1.424E-06	8.651E-09	1.388E-07	5.183E-10	2.754E-04	6.939E-07	6.448E-08	1.235E-09	8.739E-09	1.754E-10
Shamir	2.046E-06	1.054E-08	2.451E-07	9.144E-10	3.719E-04	8.936E-07	8.684E-08	1.454E-09	1.200E-08	2.690E-10
Meitzar 3	4.614E-07	2.464E-09	2.184E-07	8.400E-10	3.352E-04	8.210E-07	7.444E-08	1.323E-09	9.620E-09	1.775E-10
Balzam	5.068E-06	3.596E-08	1.782E-07	7.306E-10	2.994E-04	7.870E-07	6.837E-08	1.254E-09	9.158E-09	1.839E-10
Meitzar 2	1.515E-05	8.904E-08	1.857E-07	7.083E-10	3.897E-04	9.104E-07	8.800E-08	1.470E-09	1.165E-08	2.426E-10
Makla	9.880E-06	5.963E-08	1.639E-07	6.386E-10	3.063E-04	6.883E-06	7.063E-08	1.286E-09	9.321E-09	1.859E-10
Yahav 116	2.376E-06	1.234E-08	2.608E-07	1.019E-09	3.312E-04	7.898E-07	7.060E-08	1.265E-09	9.337E-09	2.288E-10
Yahav 6	9.235E-06	5.569E-08	2.445E-07	9.515E-10	3.508E-04	8.362E-07	7.156E-08	1.343E-09	9.091E-09	1.823E-10
Yahav 16	6.772E-06	4.224E-08	2.284E-07	8.702E-10	3.125E-04	7.555E-07	6.568E-08	1.270E-09	8.754E-09	1.992E-10
Tzofar 20	1.567E-05	8.123E-08	1.681E-07	6.253E-10	2.458E-04	6.362E-07	4.997E-08	1.105E-09	6.521E-09	1.272E-10
H.Tveria	2.826E-05	1.494E-07	1.018E-07	3.899E-10	1.930E-04	5.229E-06	5.037E-08	1.074E-09	6.947E-09	1.408E-10
Mineral	2.786E-08	2.840E-10	7.479E-08	2.904E-10	8.459E-05	3.532E-07	1.687E-08	7.941E-10	1.912E-09	5.448E-11
Qedem	9.132E-06	5.518E-08	4.376E-08	1.818E-10	6.107E-05	6.089E-06	2.396E-08	8.053E-10	3.249E-09	8.021E-11

A.6, therefore their argon concentrations were calculated only from  $^{36}\text{Ar}$ , as explained in sections 2.2 and 4.2.

## 5.1 Noble gas temperatures

The concentrations from Table 5.3 were fitted to different excess air models to obtain NGTs and the atmospheric component of each noble gas, as explained in chapters 2 and 4.

Examination of the neon concentrations in Table 5.3 reveals that Ein Gofra, Ein Balzam, Meitzar 2, Ein Makla, Tzofar 20, Hamat Tveria, Mineral and Ein Qedem contain less than  $2 \cdot 10^{-7}$  ccSTP/g, therefore it is expected to see degassing effects in the fit results. Mineral and Ein Qedem, both from the Dead Sea area, have very low neon concentrations and generally lower noble gas concentrations than the rest of the samples. This is probably due to the very high salinities there ( $\sim 200$  g/kg [Stern, 2010]), leading to a low solubility in these cases. The high salinities are taken into account in the preparation of the samples for the fit, since at least part of the water discharging from these locations originates from Dead Sea water [Starinsky, 1974] and not fresh water. The initial salinity in Panga was hence set to 200 g/kg for the Mineral and Ein Qedem samples.

Noble gas concentrations from all the samples were fitted with the UA model, which is the most simple model (Equation 2.16). Ein Gofra, Ein Balzam, Ein Makla, Hamat Tveria and Ein Qedem show negative excess air fractions, which indicates degassing processes. However, this model is very simplified, thus the CE model is used.

The CE model was chosen to fit the samples of this study, since it can be adopted for degassed samples as well. In a first step, all the samples were fitted with initial  $F = 0.5$  (see Equation 2.20). Only Meitzar 3 and Ein Yahav 16 give reasonable results, with  $0 < A < 0.05$  and  $0 < F < 0.1$ , therefore another fit was performed, this time with  $F > 1$ , or to be more concrete  $F = 2$ , for the samples that show possible degassing from their neon concentrations and the fit results of the UA model. The CE model fit results are shown in Table 5.4.

The results were optimized using Monte Carlo simulations, as explained in chapter 4. The samples can be divided into four groups of different results characteristics. Examples of Monte Carlo results from each group are shown in Figure 5.1.

1. **Normal, reasonable results:** There are two samples in this group. Ein Yahav 16 is the only sample which did not need to be optimized. Ein Yahav 6, as well, gave reasonable fit parameters ( $F < 1$  and  $A \ll 1$ ).
2. **Degassing:** This group consists of Ein Gofra, Ein Makla, Ein Balzam, Hamat Tveria, Tzofar 20 and Mineral. They are characterized by  $F \gg 1$  and  $A \ll 1$ , indicating degassing. The CE model is not aimed to estimate the amount of degassing, therefore in such case the model parameters have big uncertainties. As explained in chapter 2, the excess air composition is determined by the fractionation  $F$ . In case of a degassed sample, the model calculated a “reversed” fractionation, so that air would be degassing from the sample with the same composition of the excess air and there is a big uncertainty in qualifying the degree of degassing. The samples in this group are the same samples that have a relatively low neon concentration.

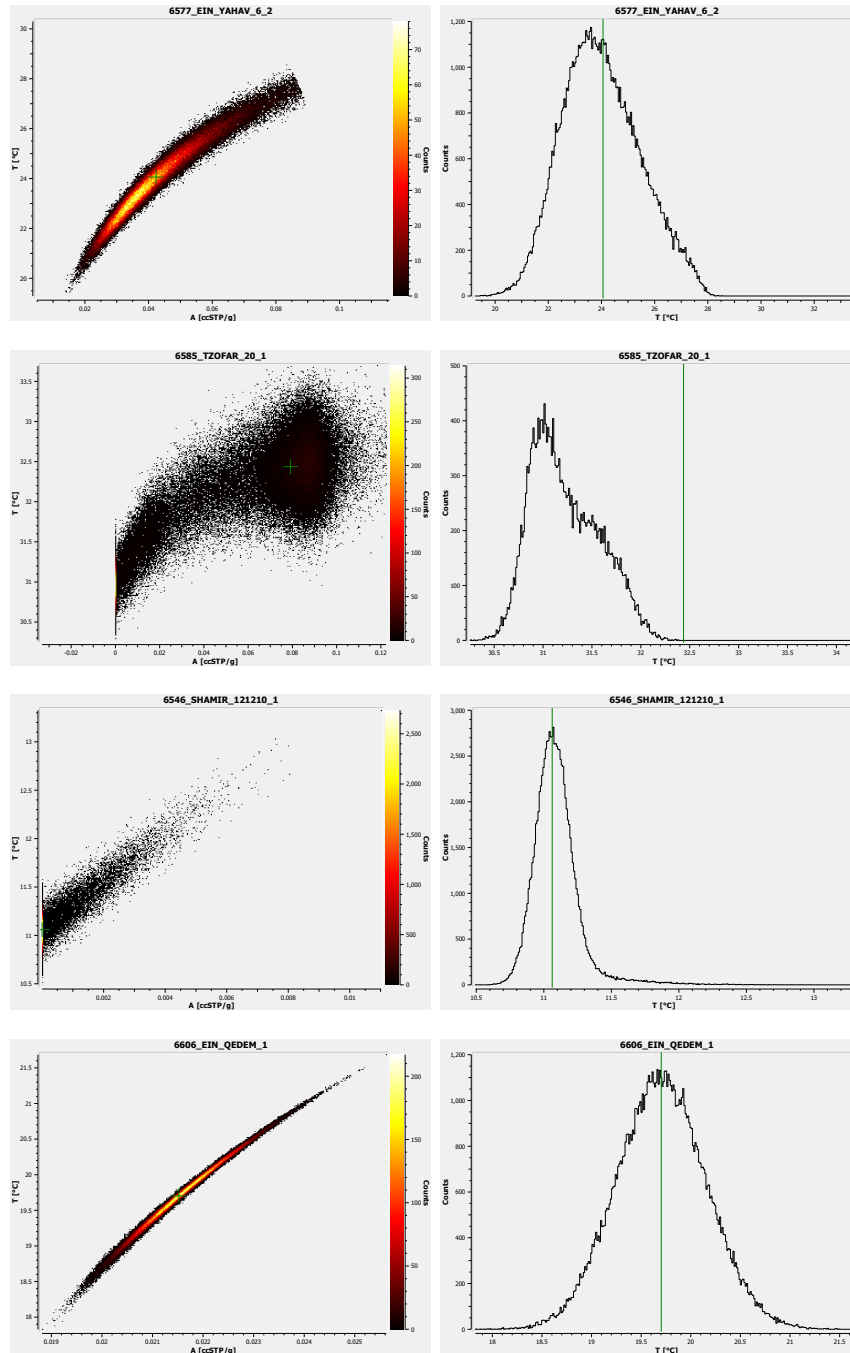


Figure 5.1: Representative results of Monte Carlo simulations, that were performed in order to optimize the NGT fits with the CE model (Equation 2.20). The results are listed in Table 5.4. The simulated temperature against the excess air fraction in each sample is plotted on the left column and a histogram of the simulated temperatures is plotted on the right column. Each of the samples represents a different type of results obtained in this study. From the top to bottom the samples are: Ein Yahav: Reasonable excess air fraction, Tzofar 20: Degassing, Shamir: Quasi equilibrated and Ein Qedem: Results with low probability.

3. **Results with a low probability:** Meitzar 2 and Ein Qedem have  $F \gg 1$  and  $A \ll 1$  like the second group, but their  $\chi^2$  are extremely high. The NGT obtained for Meitzar 2 is only 2.6 °C, indicating that something went wrong with this sample. However, there were no special events during the sampling, except of small bubbles seen in the sampling tube (see Appendix A.5), but these were also formed in other samples. Ein Qedem is the saltiest sample and has generally lower noble gas concentrations than the rest of the samples (Table 5.3), suggesting that massive degassing might have taken place before the sample was taken.
4. **quasi-equilibrated samples:** This group consists Shamir, Meitzar 3 and Ein Yahav 116, with  $F; A \ll 1$ . However, there is a possibility that these parameters are positive, due to the big uncertainties. Meitzar 3 indeed shows reasonable results with the UA. It is inferred that these samples are close to equilibrium state.

Overall, the CE model gives reasonable NGTs for most samples, ranging from 11 °C in Shamir to 31 °C in Tzofar 20 in the north and south, respectively. Meitzar 2 and Ein Qedem are excluded from the discussion due to big uncertainties of their results. The average NGT in the northern part of the sampling area is 17.8 °C and in the southern, the average is 23.9 °C. These temperatures are comparable with the present annual mean air temperatures. According to data from the Israeli Meteorological Service, an annual average air temperature of 18 °C was measured between 1983–2000 in Kfar Blum, north of Lake Kinneret. In Sodom, south of the Dead Sea, an annual average air temperature of 23 °C was measured in 1983–2000. Hamat Tveria and Tzofar 20 have slightly higher NGTs than the rest of the samples in their regions, north and south respectively. This is further discussed in chapter 6.

Table 5.4: Results of fit to the CE model. The upper table shows the fitted NGTs and the atmospheric component of  $^3\text{He}$  and He (equilibrium + excess air). The lower table shows the fit parameters. H.Tveria refers to the spring of Hamat Tveria. The uncertainties of the parameters are the calculated standard deviations of the Monte Carlo simulations. Ein Yahav 16 was not optimized by Monte Carlo and has a chi square in [%], refers to the probability to obtain the listed fit results.

Sample	NGT [°C]	$\Delta\text{NGT}$ [°C]	$^3\text{He}_{atm}(\text{CE})$ [ccSTP/g]	$\Delta^3\text{He}_{atm}(\text{CE})$ [ccSTP/g]	$\text{He}_{atm}(\text{CE})$ [ccSTP/g]	$\Delta\text{He}_{atm}(\text{CE})$ [ccSTP/g]
Shamir	11.09	0.18	8.461E-14	5.672E-16	6.171E-08	3.919E-10
Gofra	19.24	0.42	4.386E-14	2.478E-16	3.233E-08	1.740E-10
Meitzar 2	2.64	0.11	5.671E-14	3.155E-16	4.168E-08	2.272E-10
Meitzar 3	18.80	0.90	7.294E-14	4.116E-16	5.349E-08	2.877E-10
Makla	16.19	0.44	5.240E-14	3.040E-16	3.854E-08	2.186E-10
Balzam	17.60	0.15	5.866E-14	3.271E-16	4.305E-08	2.354E-10
H. Tveria	23.85	1.70	3.325E-14	1.864E-16	2.447E-08	1.348E-10
Mineral	21.88	1.90	2.662E-14	2.415E-15	1.948E-08	1.539E-09
Qedem	19.71	0.45	1.548E-14	8.647E-17	1.139E-08	6.302E-11
Yahav 6	24.00	1.46	8.314E-14	4.560E-16	6.098E-08	3.364E-10
Yahav 16	22.31	0.93	7.956E-14	7.696E-16	5.817E-08	5.111E-10
Yahav 116	20.13	0.64	9.449E-14	1.157E-15	6.877E-08	7.533E-10
Tzofar 20	31.23	0.35	5.847E-14	2.727E-16	4.289E-08	1.967E-10

Sample	A [ccSTP/g]	$\Delta A$ [ccSTP/g]	F	$\Delta F$	$\chi^2$	$\Delta\chi^2$
Shamir	1.234E-04	5.287E-04	-3043.66	989.82	5.3	4.2
Gofra	1.888E-03	1.614E-03	4.88	4.83	1.8	2.3
Meitzar 2	1.055E-04	4.997E-03	958.12	90.10	159.1	25.3
Meitzar 3	1.432E-02	7.195E-03	-3.22	102.95	3.4	3.4
Makla	8.110E-07	7.210E-06	947.41	174.82	7.9	5.3
Balzam	-6.735E-07	1.137E-06	1001.41	336.34	3.9	3.4
H.Tveria	1.904E-02	1.112E-02	3.79	93.55	6.4	4.9
Mineral	-3.070E-03	1.664E-03	102.16	334.55	2.3	2.7
Qedem	2.156E-02	7.615E-04	1.52	0.01	645.5	50.7
Yahav 6	4.346E-02	1.319E-02	0.63	0.01	1.1	1.5
Yahav 16	3.449E-03	3.021E-03	0.09	0.57	0.2	69.1
Yahav 116	1.200E-03	1.450E-03	-1416.44	1878.52	1.3	1.7
Tzofar 20	6.458E-03	7.772E-03	148.40	574.43	3.9	4.5

## 5.2 Helium isotopes

Helium isotopes,  $^3\text{He}$  and  $^4\text{He}$ , are used as tracers of intrusion of volatiles from the mantle into the crust on the Israeli side of the Dead Sea Transform. The concentrations of both isotopes are plotted against each other in Figure 5.2. The results show two main branches

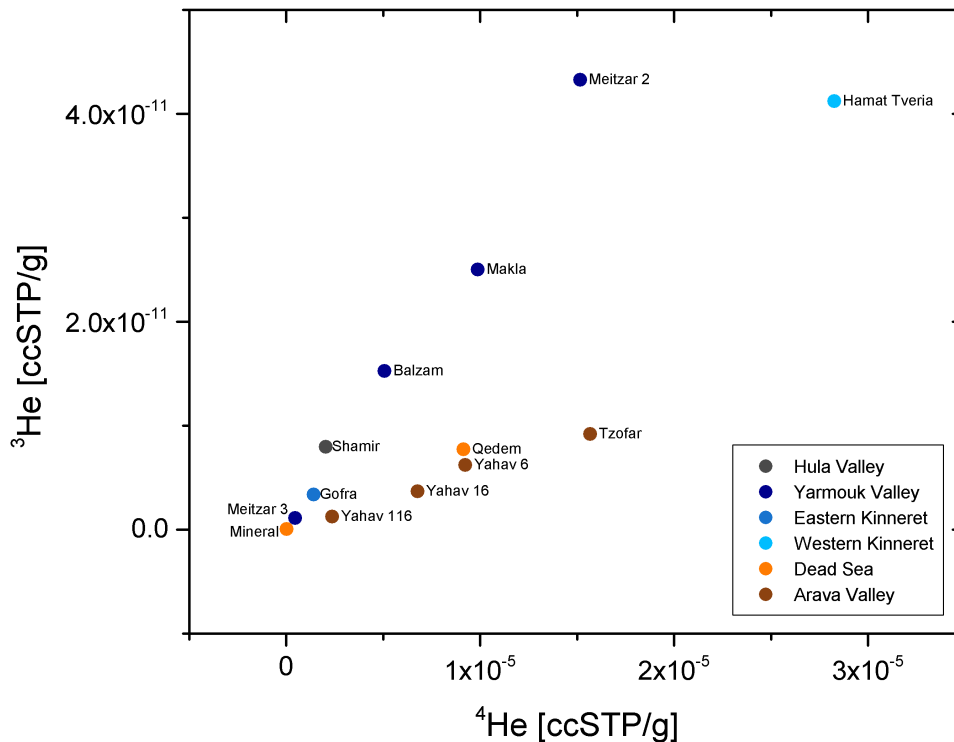


Figure 5.2:  $^3\text{He}$  concentration versus  $^4\text{He}$  concentration. Samples from the same geographic area are marked with the same color. Note the different trends of samples from the northern part of the sampling area and samples from southern part of the sampling area.

and the sample from Hamat Tveria, which lies between them. The upper branch consists of samples from the northern regions of the sampling area (Hula Valley, Lake Kinneret and Yarmouk Valley) and the lower branch consists of samples from the southern regions (Dead Sea and Arava Valley), meaning that northern samples tend to contain more  $^3\text{He}$  relative to the southern ones. This might be an evidence of an enhanced mantle derived helium component there, since  $^3\text{He}$  predominantly originates from the mantle. Interesting is that samples that are located in the same field have different isotope compositions. Meitzar 2 and Meitzar 3 wells are a few meters away from each other, but contain different amounts of  $^3\text{He}$  and  $^4\text{He}$ . Ein Makla and Ein Balzam, the sampled springs of Hamat Gader, lie 5 km away from Meitzar and also have significantly different amounts of  $^3\text{He}$  and  $^4\text{He}$ . The same is true for the three wells from Ein Yahav. Mineral and Ein Qedem are located by the Dead Sea, only 4 km away from each other and show different isotope concentrations. Hamat Tveria lies on the western shore of Lake Kinneret and has much higher isotope concentrations than the rest of the samples. Looking more closely at Figure 5.2, it can

be noticed that the samples from Tzofar 20 is shifted from the other samples as well, so that the two might form a new branch. Interesting is that Tzofar 20 and the samples from Lake Kinneret shores (Hamat Tveria and Gofra) show a correlation between their helium concentration ( $\approx {}^4\text{He}$ ) and their electrical conductivity, which is used here as an indication for water salinity (Figure 5.3).

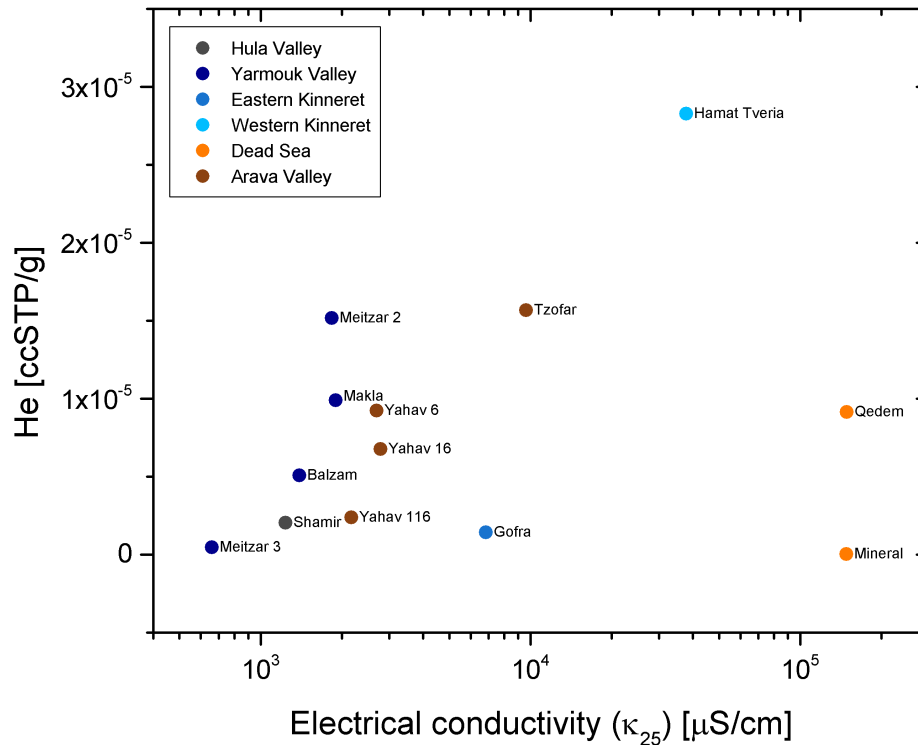


Figure 5.3: Helium concentration versus electrical conductivity, which is related to the water salinity. The conductivity is presented on a logarithmic scale. Samples from the same geographic area form clusters and show different trends, except of the sample from Tzofar 20, which lies closer to the samples from the eastern and western Lake Kinneret.

### 5.3 Helium components

The fractionation ratio  ${}^3\text{He}/{}^4\text{He}$  is calculated and separated into tritiogenic, atmospheric and terrigenous, consists of radiogenic and mantle components, as shown in Figure 2.6. The decomposition is done in steps. First of all, the tritiogenic component is discussed, then terrigenous helium is separated from atmospheric helium and finally mantle derived helium and crustal helium are calculated from the terrigenous helium.

### 5.3.1 Tritiogenic helium:

Tritium was measured in order to determine the tritiogenic helium amount in each sample. The results are given in Table 5.5. Values under 2 TU are considered as background noise since it is the detection limit of the measurement system.

Table 5.5: Tritium concentrations in the thermal waters of the Dead Sea Transform. The concentrations are calculated from equation 2.13. Values smaller than 2 TU are under the detection limit of the measurement system, therefore they are interpreted as 0 TU.

Sample	$^3\text{H}$ [TU]	$\Delta ^3\text{H}$ [TU]
Gofra	1.01	0.92
Meitzar 2	0.91	0.96
Balzam	0.12	0.97
Shamir	0.62	1.01
Meitzar 3	0.66	1.00
Makla	0.66	0.95
Yahav 116	1.90	1.02
Yahav 6	6.52	1.10
Yahav 16	0.25	1.04
Tzofar 20	0.83	1.06
H.Tveria	0.74	1.03
Mineral	3.34	1.09
Qedem	0.08	0.87

Thermal waters are generally considered to be old enough, so that no tritium should be found in them. Hence, finding tritium in such samples indicates mixing with younger water. Ein Yahav 6 and Mineral are the only samples that contain a significant amount of tritium. However, the amount of 6.5 TU, measured in Ein Yahav 6, corresponds to  $\sim 100 \text{ TU} \approx 2 \cdot 10^{-13} \text{ ccSTP/g}$  of tritiogenic  $^3\text{He}$  produced in the water since the tritium bomb peak in 1963, calculated from Equation 2.13. This is one order of magnitude lower than the total concentration of  $^3\text{He}$  in the sample, therefore is neglected in the further analysis. The case of Mineral is different, since the  $^3\text{He}$  concentration of this sample is  $\sim 3 \cdot 10^{-14}$ , which is lower than the tritiogenic helium concentration that should have been dissolved there of  $\sim 51 \text{ TU} \approx 1 \cdot 10^{-13} \text{ ccSTP/g}$ . It can be explained by mixing of the water in this well with younger water from the Dead Sea or the local fresh groundwater. However, the initial amount of tritium infiltrated during the mixing is not known, therefore it is not clear how much tritiogenic helium presents in this sample. Hence, tritiogenic helium in the sample from Mineral is neglected too.

### 5.3.2 Terrigenic versus atmospheric helium:

The ratios  $^3\text{He}/^4\text{He}$  and  $\text{Ne}/\text{He}$  were calculated for each sample in order to distinguish between atmospheric and terrigenic helium in the water. The results are given in Table 5.6.

Figure 5.4 shows the relationship between the atmospheric and terrigenic components. It is noticeable that samples from the same geographic area lie close to each other. Waters

Table 5.6:  ${}^3\text{He}/{}^4\text{He}$  and Ne/He ratios.  $R_s$  corresponds to the measured  ${}^3\text{He}/{}^4\text{He}$ .  $R_{corr}$  is the air corrected  ${}^3\text{He}/{}^4\text{He}$  ratio, from Equation 2.30, using the measured Ne/He ratios. The  ${}^3\text{He}/{}^4\text{He}$  ratios are normalized to  ${}^3\text{He}/{}^4\text{He}$  in air,  $R_a$ , which is:  $(1.384 \pm 0.006) \cdot 10^{-6}$  [Clarke et al., 1976].

Sample	$R_s$	$\Delta R_s$	$R_s/R_a$	$\Delta(R_s/R_a)$	$R_{corr}/R_a$	$\Delta(R_{corr}/R_a)$	Ne/He	$\Delta$ (Ne/He)
Gofra	2.371E-06	1.011E-07	1.713	0.073	1.714	0.073	0.097	0.001
Shamir	3.893E-06	1.702E-07	2.813	0.123	2.815	0.123	0.120	0.001
Meitzar 3	2.394E-06	1.074E-07	1.730	0.078	1.734	0.078	0.473	0.003
Balzam	3.008E-06	1.538E-07	2.173	0.111	2.174	0.111	0.035	0.000
Meitzar 2	2.856E-06	1.258E-07	2.063	0.091	2.064	0.091	0.012	0.000
Makla	2.531E-06	1.059E-07	1.829	0.077	1.829	0.077	0.017	0.000
Yahav 116	5.224E-07	2.008E-08	0.377	0.015	0.377	0.015	0.110	0.001
Yahav 6	6.718E-07	2.661E-08	0.485	0.019	0.485	0.019	0.026	0.000
Yahav 16	5.419E-07	2.177E-08	0.392	0.016	0.391	0.016	0.034	0.000
Tzofar 20	5.853E-07	2.293E-08	0.423	0.017	0.423	0.017	0.011	0.000
H. Tveria	1.458E-06	6.553E-08	1.053	0.047	1.053	0.047	0.004	0.000
Mineral	1.192E-06	4.959E-08	0.862	0.036	0.858	0.037	2.685	0.029
Qedem	8.463E-07	3.236E-08	0.611	0.023	0.611	0.023	0.005	0.000

from the north have the highest  $^3\text{He}/^4\text{He}$  ratios, between  $1 R_a$  in Hamat Tveria and  $2.8 R_a$  in Shamir. Ein Qedem and Mineral from the Dead Sea have  $^3\text{He}/^4\text{He}$  ratios of  $0.6 R_a$  and  $0.9 R_a$ , respectively and southernmost samples from the Arava Valley show a range of  $^3\text{He}/^4\text{He}$  from  $0.4 R_a$  to  $0.5 R_a$ .

All the samples have  $^3\text{He}/^4\text{He}$  ratios that are higher than the typical crustal ratio (see Section 2.4), indicating that they all contain some fraction of mantle derived helium. As for the atmospheric component, all the samples, except of Mineral and Meitzar 3, lie almost exactly on the mixing line between crustal and mantle derived helium endmembers and contain a very minimal amount of Ne/He. This indicates that helium in the samples is mostly of terrigenous origin and only a very small amount comes from atmospheric origin. This even holds for the samples from springs, that usually experience more ad-mixing compared to wells and therefore would be expected to contain higher atmospheric helium. In contrast, Mineral and Meitzar 3 have a considerable atmospheric component. These were also the samples that were most affected by air contamination during sampling, as described in Appendix A.5.

Another interesting sample is Hamat Tveria, that shows a  $^3\text{He}/^4\text{He}$  ratio which is very close to the atmospheric ratio ( $R_s \approx 1$ ). One could think that it is a result of a prominent atmospheric component, but this is not the case. Hamat Tveria has a very low neon to helium ratio (Table 5.6), due to the high  $^4\text{He}$  concentration in this sample shown in Figure 5.2. During the time of recharge, this water contained the helium and neon concentrations of the atmospheric endmember, which are marked as “Atmosphere” in Figure 5.4. The water got older and incorporate helium from the crust and from the mantle, causing it to move along a mixing line between atmospheric and local terrigenous endmembers. It happened to be that the final helium isotope composition is very similar to the atmospheric ratio. This case demonstrates how useful it is to examine the neon concentration together with the helium isotopes concentrations, because they can be a big help to distinguish between atmospheric and terrigenous influences.

**Air correction:**

The separation to components was performed in two ways: By calculation of the mixing line intercept (Equation 2.35) and by using the fitting results of Panga from Table 5.4, for the atmospheric component (Equation 2.38).

The first method is demonstrated in Figure 5.4 for two of the samples, that have the highest Ne/He ratio. Since each sample is located on a mixing line between the atmospheric end member and a terrigenous end member, the uncontaminated  $^3\text{He}/^4\text{He}$  can be determined. Such a mixing line is drawn for Mineral and Meitzar 3, as shown in Figure 5.4. The intercept of this line with the y axis represents the terrigenous component of the sample. In case of Mineral, this value is almost identical to the terrigenous component of Ein Qedem, which is located only about 5 km away from Mineral. If Mineral would really contain a significant amount of tritiogenic helium, it would not lie so close to the point of Ein Qedem, after the air correction. Therefore it is deduced that the sample of Mineral consists of a big atmospheric helium component, a smaller terrigenous one and no further components. Applying the same correction for Meitzar 3 brings it close to Meitzar 2, which is located in the same well field.

The differences between the results of the two methods do not exceed the 10 % except for Mineral, having about a 39 % difference. The higher differences occur in samples that have

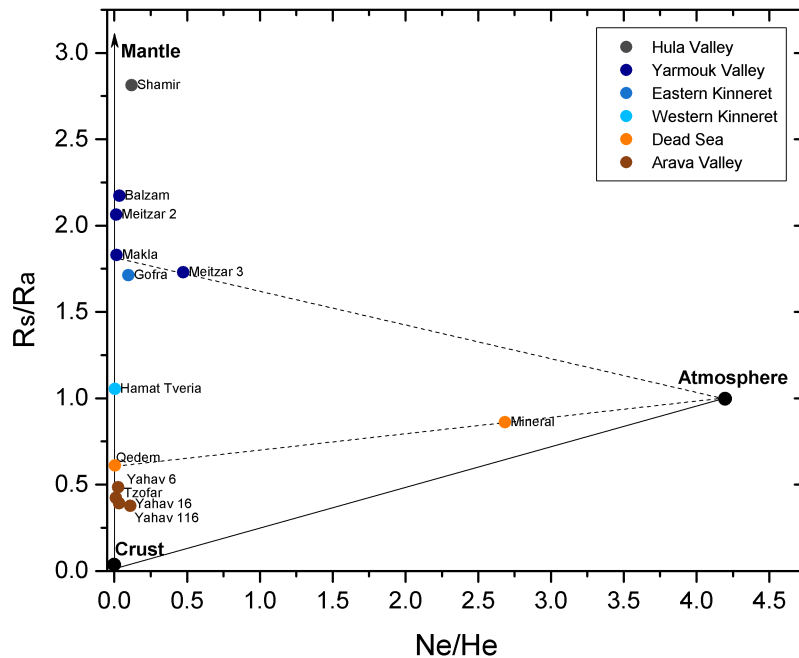


Figure 5.4:  $^3\text{He}/^4\text{He}$  versus the concentration ratio of Ne/He.  $R_s$  is normalized to the isotopic ratio in the atmosphere,  $R_a = 1.384 \cdot 10^{-6}$  from Clarke et al. [1976]. The solid lines represent mixing lines between the atmosphere, crust and mantle endmembers, following Figure 2.7. The dashed lines represent the air corrections of Mineral and Meitzar 3 (see the text for more information). The data for this graph is taken from Table 5.6.

a more significant atmospheric component, or better to say, a high Ne/He ratio, as seen in Figure 5.4. Since most of the samples in this study have small atmospheric components, both methods are proper for the air correction, except of the sample from Mineral. Since not all the samples could be well fitted, as shown in Section 5.1, the first method of intercept determination was chosen for the further analysis. The corrected  $^3\text{He}/^4\text{He}$  ratios are given in Table 5.6.

### 5.3.3 Separation of atmospheric, crustal and mantle derived helium

The relative parts of atmospheric, crustal and mantle derived helium components were calculated for each sample using equations 2.44 and 2.42. The results are given in Table 5.7. Figure 5.5 combines all the three components. It is actually an extension of Figure 5.4, where the terrigenous component is now split into crustal and mantle components.

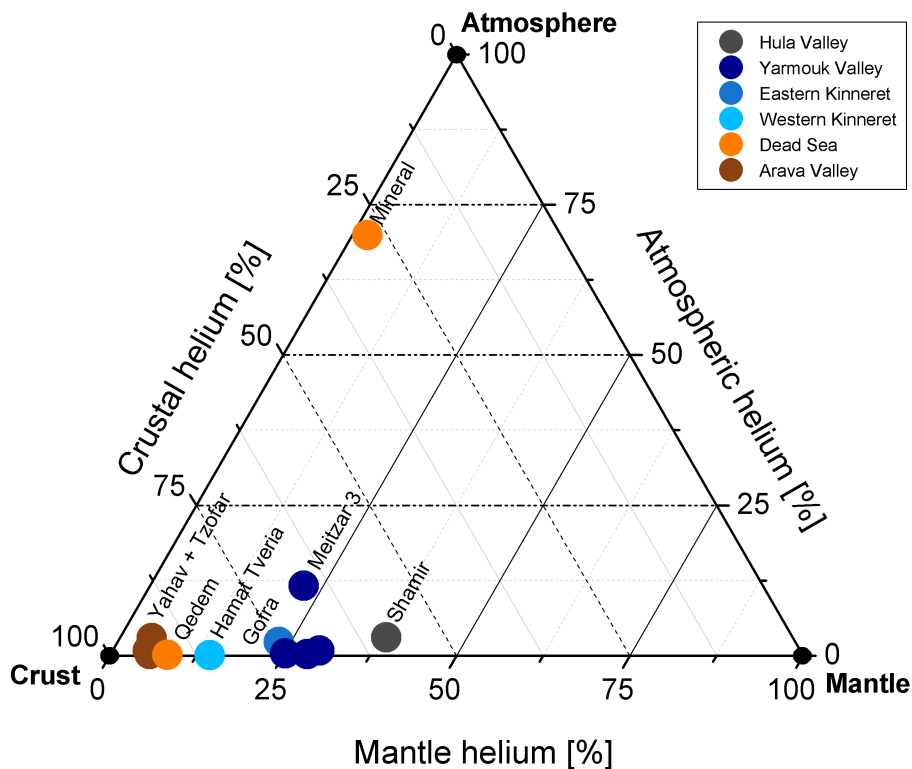


Figure 5.5: The relative parts of mantle, atmospheric and crustal helium components in each sample. The data for the graph is taken from Table 5.7. The mantle, atmospheric and crustal endmembers are marked on the graph and each axis represents a mixing line between two of them. The grid lines of the mantle component are marked with a solid line, the grid lines of the atmospheric component are marked with a dashed-dotted line and the grid lines of the crustal component are marked with a dashed line. The percentage of each component in a sample is read parallel to these lines. For example, the sample from Mineral contains 69.2 % atmospheric  $^4\text{He}$ , 2.29 %  $^4\text{He}$  from a mantle origin and 28.5 % crustal helium.

It is seen in Table 5.7 that the fraction of  $^3\text{He}$  from the mantle is above 90% in almost all samples. One might be surprised to see that Tzofar, for example, has about 96% mantle  $^3\text{He}$ , a bit higher than Meitzar 3, while Figure 5.4 shows that the mantle component of Meitzar 3 is bigger than that of Tzofar 20.

The mantle  $^4\text{He}$  percentage in Table 5.7 indicates that Meitzar 3 indeed contains more mantle helium than Tzofar 20 (22% compared to 6%). However, it is a direct consequence of the mixing model used here. As explained in Section 2.4.1, only  $^4\text{He}$  includes useful information about the partition of atmospheric, crustal and mantle derived helium in the water.

All the samples, except of Mineral, contain more than 90% terrigenic helium. This is visualized in Figure 5.5, where all data points are concentrated at the bottom of the triangle and show low atmospheric fractions. Mineral lies far away from the other samples, with 69.2% atmospheric helium, which is an evidence to the air contamination that occurred during sampling (see Appendix A.5 for more information). Therefore it is excluded from the general discussion later.

Mantle fraction of the total He in the sampled waters ranges from 4% in Ein Yahav 116 to 39% in Shamir. It can be noticed here as well, that northern samples contain more mantle helium.

Table 5.7: Atmospheric, crust and mantle derived helium components of the total helium concentration in the water. Their calculation is explained in Section 2.4.1.

Sample	${}^4\text{He}_A$	$\Delta {}^4\text{He}_A$	${}^3\text{He}_A$	$\Delta {}^3\text{He}_A$	${}^4\text{He}_M$	$\Delta {}^4\text{He}_M$	${}^3\text{He}_M$	$\Delta {}^3\text{He}_M$	${}^4\text{He}_C$	$\Delta {}^4\text{He}_C$	${}^3\text{He}_C$	$\Delta {}^3\text{He}_C$
Gofra	<b>2.27</b>	0.02	<b>1.32</b>	0.06	<b>23.25</b>	1.01	<b>98.05</b>	5.98	<b>74.48</b>	1.01	<b>0.63</b>	0.03
Shamir	<b>3.02</b>	0.02	<b>1.07</b>	0.05	<b>38.39</b>	1.71	<b>98.63</b>	6.15	<b>58.59</b>	1.71	<b>0.30</b>	0.02
Meitzar 3	<b>11.59</b>	0.09	<b>6.70</b>	0.30	<b>22.20</b>	1.08	<b>92.74</b>	6.12	<b>66.20</b>	1.08	<b>0.55</b>	0.03
Balzam	<b>0.85</b>	0.01	<b>0.39</b>	0.02	<b>29.82</b>	1.54	<b>99.15</b>	7.21	<b>69.33</b>	1.54	<b>0.46</b>	0.03
Meitzar 2	<b>0.28</b>	0.00	<b>0.13</b>	0.01	<b>28.38</b>	1.26	<b>99.37</b>	6.22	<b>71.35</b>	1.26	<b>0.50</b>	0.02
Makla	<b>0.39</b>	0.00	<b>0.21</b>	0.01	<b>25.11</b>	1.06	<b>99.20</b>	5.90	<b>74.50</b>	1.06	<b>0.59</b>	0.03
Yahav 116	<b>2.89</b>	0.04	<b>7.67</b>	0.31	<b>4.64</b>	0.20	<b>88.79</b>	5.15	<b>92.47</b>	0.20	<b>3.54</b>	0.14
Yahav 6	<b>0.66</b>	0.01	<b>1.36</b>	0.06	<b>6.44</b>	0.27	<b>95.87</b>	5.49	<b>92.90</b>	0.27	<b>2.77</b>	0.11
Yahav1 16	<b>0.86</b>	0.01	<b>2.20</b>	0.09	<b>5.11</b>	0.22	<b>94.33</b>	5.53	<b>94.03</b>	0.22	<b>3.47</b>	0.14
Tzofar 20	<b>0.27</b>	0.00	<b>0.65</b>	0.03	<b>5.63</b>	0.23	<b>96.14</b>	5.44	<b>94.10</b>	0.23	<b>3.22</b>	0.13
H. Tveria	<b>0.09</b>	0.00	<b>0.08</b>	0.00	<b>14.39</b>	0.66	<b>98.74</b>	6.32	<b>85.52</b>	0.66	<b>1.17</b>	0.05
Mineral	<b>69.94</b>	5.57	<b>81.17</b>	7.29	<b>2.19</b>	0.91	<b>18.36</b>	7.66	<b>27.87</b>	5.65	<b>0.47</b>	0.10
Qedem	<b>0.12</b>	0.00	<b>0.20</b>	0.01	<b>8.26</b>	0.32	<b>97.63</b>	5.35	<b>91.61</b>	0.32	<b>2.17</b>	0.08

## 5.4 Carbon isotopes

$\delta^{13}\text{C}$  is analysed in order to gain further information about volatile fluxes from the mantle. The results are given in Table 5.8. The isotopic composition of the samples varies from the most depleted with  $-11.8\text{‰}$  (Meitzar 3) to Mineral with  $+5.5\text{‰}$ , which is the only positive value and about  $6\text{‰}$  higher than the second enriched sample, Hamat Tveria, with  $-1.8\text{‰}$ . Most of the samples, except of Mineral, have  $\delta^{13}\text{C}$  values in the range of groundwater, between  $-20\text{‰}$  and  $0\text{‰}$ . The extreme high  $\delta^{13}\text{C}$  in the sample from Mineral can be due to the fact that the hyper saline water of this spring consists of some fraction of Dead Sea water, which also shows positive  $\delta^{13}\text{C}$  values, up to  $4\text{‰}$  [Barkan et al., 2001].

Table 5.8: Carbon isotopes and concentrations in thermal waters in the Israeli side of the Dead Sea Transform.  $\text{CO}_2/{}^3\text{He}$  data are taken from Torfstein et al. [2013]. **M**, **L** and **S** correspond to mantle, limestone and sediment derived  $\text{CO}_2$  components, which were calculated from the mixing model explained in Section 2.4.2. The uncertainty of these components is determined from the range of the isotope signature of  $\text{CO}_2$  from mantle, limestone and sediment origin and are explained in the text.

Sample	$\delta^{13}\text{C}$ [‰]	$\Delta \delta^{13}\text{C}$ [‰]	$\text{CO}_2/{}^3\text{He}$	M [%]	L [%]	S [%]
Meitzar 3	<b>-11.793</b>	0.004	<b>1.190E+09</b>	<b>1.26</b>	<b>59.70</b>	<b>39.04</b>
Balzam	<b>-8.446</b>	0.028	<b>7.540E+08</b>	<b>1.99</b>	<b>70.29</b>	<b>27.72</b>
Makla	<b>-7.633</b>	0.013	<b>2.315E+08</b>	<b>6.48</b>	<b>69.48</b>	<b>24.04</b>
Meitzar 2	<b>-3.399</b>	0.003	<b>2.300E+09</b>	<b>0.65</b>	<b>88.16</b>	<b>11.19</b>
Qedem	<b>-1.096</b>	0.019	<b>1.254E+09</b>	<b>1.20</b>	<b>95.41</b>	<b>3.39</b>
Gofra	<b>-8.382</b>	0.019	<b>2.330E+09</b>	<b>0.64</b>	<b>71.56</b>	<b>27.80</b>
Tzofar	<b>-7.150</b>	0.026	<b>1.580E+07</b>	<b>94.94</b>	<b>1.80</b>	<b>3.26</b>
H. Tveria	<b>-1.847</b>	0.001	<b>1.873E+08</b>	<b>8.01</b>	<b>87.57</b>	<b>4.42</b>
Yahav 6	<b>-5.714</b>	0.002	-	-	-	-
Yahav 16	<b>-3.396</b>	0.025	-	-	-	-
Yahav 116	<b>-6.203</b>	0.002	-	-	-	-
Mineral	<b>5.543</b>	0.010	-	-	-	-
Shamir 1	<b>-1.535</b>	0.007	-	-	-	-

Ein Makla, Tzofar, Ein Yahav 6 and Ein Yahav 116 are the only samples that lie in the typical  $\delta^{13}\text{C}$  range in the upper mantle:  $-8\text{‰} < \delta^{13}\text{C} < -5\text{‰}$  [Sano and Marty, 1995]. Since both helium and carbon are still escaping from the mantle, it would be expected to find more mantle helium in samples that have  $\delta^{13}\text{C}$  typical for the mantle, but Figure 5.6 shows no such correlation. This is probably due to the fact that  $\delta^{13}\text{C}$  could only be measured from the total carbon in the water, including all species of carbon. Furthermore, in contrast to  ${}^3\text{He}/{}^4\text{He}$ , no correlation between  $\delta^{13}\text{C}$  and geographic locations is seen (Figure 5.6).

In order to have a better understanding of the carbon origin, the  $\delta^{13}\text{C}$  data are combined with  $\text{CO}_2/{}^3\text{He}$  data from [Torfstein et al., 2013]. These authors suggest that the origin of the carbon is mostly from reactions in the crustal sediments and mention the option to use the isotopic signatures in order to gain more information. After finding out that only a part of the helium in the waters originates from the mantle, it can be expected to see a mixing between mantle carbon and carbon from crustal sources.

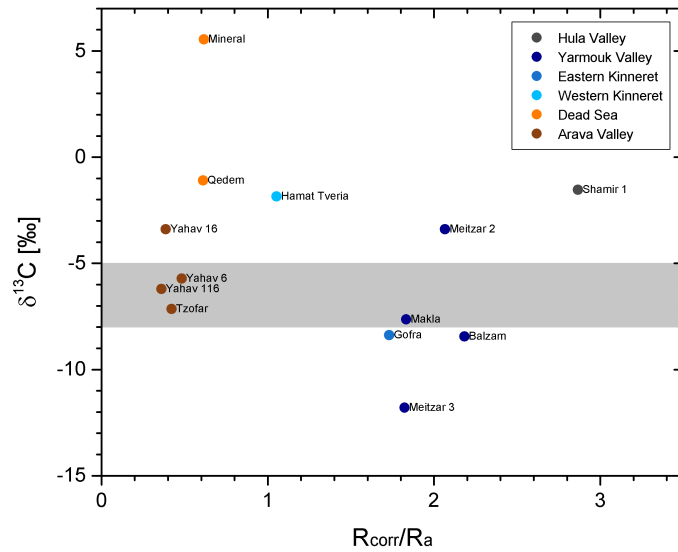
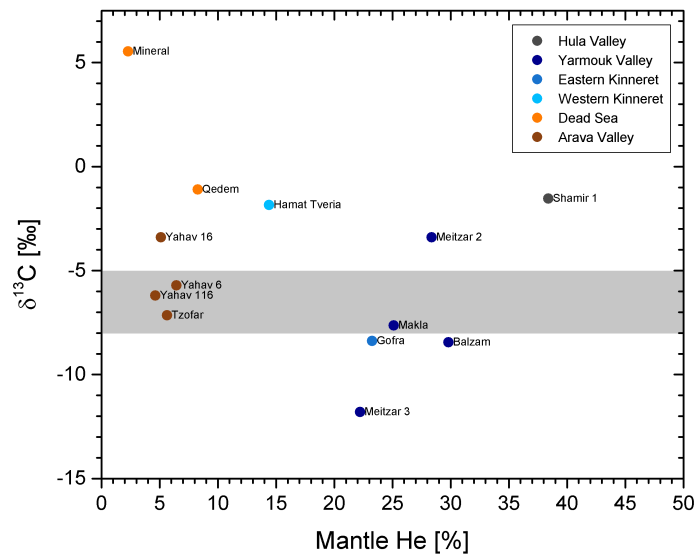
(a)  $\delta^{13}C$  versus terrigenous helium from Table 5.6.(b)  $\delta^{13}C$  versus mantle derived helium fraction from Table 5.7.

Figure 5.6: Relationship between  $\delta^{13}C$  and mantle derived helium in the samples. The shading marks the typical signature of mantle derived carbon of  $-5\text{‰} < \delta^{13}C < -8\text{‰}$ .

In order to estimate the fraction of mantle derived carbon in the water samples, a mixing model between three end members of the upper mantle (MORB), marine carbonate and sediments is used, as explained in Section 2.4.2. The results are listed in Table 5.8. The isotopic signatures and  $\text{CO}_2/{}^3\text{He}$  taken for the end members are given in Table 2.2. These values are not discrete, but have a range. Hence, they are varied here in order to determine their influence on the results.

$\text{CO}_2/{}^3\text{He}$  ratios in limestone and in sediments are varied between  $1 \cdot 10^{12}$  and  $1 \cdot 10^{14}$ . This changed the calculated endmember fractions of all samples by only a few percent. Changing the  $\delta$  value of the mantle affects the results by about  $\pm 1\%$ . The change of  $\delta$  value of the limestone leads to a change of  $\pm 10\%$  of the limestone and the sediments endmembers fractions. Varying the  $\delta$  value of the sediments leads to a change of  $\pm 50\%$  in sediment fractions and  $\pm 30\%$  for the limestone fraction in all the samples, except for limestone in Tzofar 20, which its limestone varies in  $\pm 90\%$ . The  $\text{CO}_2/{}^3\text{He}$  ratio of the upper mantle was the parameter that mostly affected the results. Taking a value of  $7.5 \cdot 10^8$  instead of  $1.5 \cdot 10^9$  reduces the results to about a half and taking  $3 \cdot 10^9$  doubles the results.

It is important to notice that the relative share of  $\text{CO}_2$  from the mantle is determined only from the  $\text{CO}_2/{}^3\text{He}$  ratios (Equation 2.50). Looking at the  $\text{CO}_2/{}^3\text{He}$  ratios of the samples and the endmembers shows that they are too low relative to the  $\text{CO}_2/{}^3\text{He}$  ratio of the mantle endmember, thus it can be expected to see mantle derived  $\text{CO}_2$  fractions that exceed the 100%. Therefore, the analysis of the carbon origin in the thermal waters from mantle, limestone and sediment sources can be done only qualitatively. Some of the endmembers percentages obtained from the mixing model are negative or bigger than 100%, which makes no sense. In order to achieve reasonable values, the ratio of  $\text{CO}_2/{}^3\text{He}$  in the mantle (Table 2.2) was reduced to  $1.5 \cdot 10^7$ , which is 100 times smaller than the original value of  $1.5 \cdot 10^9$  and the maximal value that gives reasonable results. Further reducing it lowers the mantle fractions, but leaves similar proportions between the end members.

The calculated mantle derived  $\text{CO}_2$  is found in a range of 0.64% in Ein Gofra to more than 94% in Tzofar 20, which is the southernmost sample. Tzofar 20 and Ein Makla, which have  $\delta^{13}\text{C}$  values that are typical to the mantle, show bigger mantle components in Figure 5.7. However, Hamat Tveria has a  $\delta^{13}\text{C}$  signature higher than  $-5\%$  and also show a relatively big mantle component. No correlation is seen between the mantle components and the geographic location of the samples, but it might be also due to the lack of  $\text{CO}_2/{}^3\text{He}$  data for the southern samples. As for the limestone and sediment components, most of the samples have qualitatively more limestone carbon than sedimental organic carbon, but this is not necessarily the true, due to big uncertainties of  $\pm 20\%$ .

Since a much lower  $\text{CO}_2/{}^3\text{He}$  of was considered for the mantle endmember, it cannot be considered as “mantle” any more. This means that the  $\text{CO}_2$  components distribution shown in Figure 5.7 corresponds to three non-mantle end members. Moreover,  $\text{CO}_2/{}^3\text{He}$  of the samples is on average lower than the global mean value of  $(1.5 \pm 1.1) \cdot 10^{10}$  in groundwater [Sano and Marty, 1995 ; Sano and Williams, 1996 and de Leeuw et al., 2007]. This might be due to different fractionation ratios of carbon compared to helium isotopes during gas-water exchange [Van Soest et al., 1998]. The solubility of carbon dioxide is about 40 times bigger than the solubility of helium in thermal waters [Stephen and Stephen, 1963], means that the ratio of  $\text{CO}_2$  in gas and water phase is much smaller than the ratio of helium in gas and water phase. It is therefore expected to measure a smaller fraction

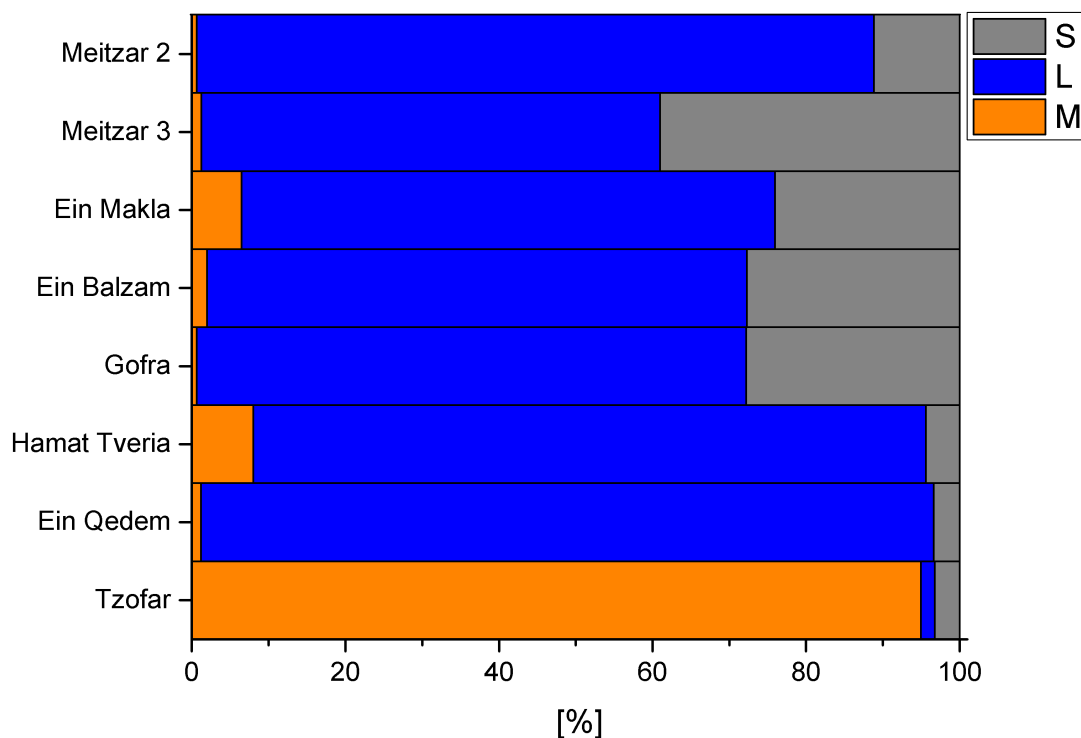


Figure 5.7: Mixing model between mantle derived carbon (**M**), marine carbonate in limestone (**L**) and carbon from sediments (**S**) components in the samples. The samples are ordered by geographic locations, from north (top) to south (bottom).  $\delta^{13}\text{C}$  and  $\text{CO}_2/{}^3\text{He}$  of the end members from Table 2.2 are inserted into the model equations described in Section 2.4.2.  $1.5 \cdot 10^7$  is taken for the mantle end member, which is 100 times smaller than the actual value, measured by [Marty and Jambon, 1987], since the later yields endmembers percentages that are negative or bigger than 100 %.

of  $\text{CO}_2$  in a gas phase, relative to the fraction of helium in a gas phase. This element fractionation explains why Tzofar 20 contains so much more “mantle” derived carbon than the other samples. This sample has the smallest  $\text{CO}_2/{}^3\text{He}$ , of  $1.58 \cdot 10^7$  whereas the rest of the samples have ratios of  $\sim 10^8$  to  $\sim 10^9$ . The crust underlies the southern Dead Sea Transform is about 10 km thicker than the crust underlies the northern Dead Sea Transform (Figure 3.3), suggesting that the water in the south can flow longer until it reaches the surface, thus enhanced element fractionation occurs there.

Despite the uncertainties and especially the big variations of  $\text{CO}_2/{}^3\text{He}$  ratios in limestone and sediment, the calculation is still useful since it shows that the carbon in the water samples from the Israeli side of the Dead Sea Transform does not originate from mantle sources. This confirms the findings of Torfstein et al. [2013], that the  $\text{CO}_2$  in the water does not originate from the mantle.

## 5.5 Stable isotopes

$\delta^{18}\text{O}$  and  $\delta^2\text{H}$  are measured in order to examine possible exchange of  $\delta^{18}\text{O}$  between the groundwater and the local rocks in high temperatures, as a results of heat flux from the mantle. The results are compared to the [Global Meteoric Water Line \(GMWL\)](#) and the local [Eastern Mediterranean Meteoric Water Line \(EMWL\)](#). They are given in Table 5.9 and shown in Figure 5.8. The measured values are spread over a large range and with the same enrichment level for  $\delta^{18}\text{O}$  and  $\delta^2\text{H}$ , in other words samples that are more enriched in  $\delta^{18}\text{O}$  are also more enriched in  $\delta^2\text{H}$ . Tzofar 20, from Arava Valley, is the most depleted sample, with  $\delta^{18}\text{O} = -8.38\text{‰}$  and  $\delta^2\text{H} = -57.6\text{‰}$ . Mineral, from the Dead Sea basin, is the most enriched sample, with  $\delta^{18}\text{O} = -4.2\text{‰}$  and  $\delta^2\text{H} = +1.08\text{‰}$ .

Table 5.9: Stable isotopes.

Sample	$\delta^{18}\text{O}$	$\Delta \delta^{18}\text{O}$	$\delta^2\text{H}$	$\Delta \delta^2\text{H}$
<b>Meitzar 3</b>	<b>-5.69</b>	0.10	<b>-28.68</b>	0.41
<b>Shamir</b>	<b>-7.03</b>	0.07	<b>-36.02</b>	0.11
<b>Balzam</b>	<b>-5.93</b>	0.09	<b>-30.74</b>	0.56
<b>Meitzar 2</b>	<b>-7.02</b>	0.15	<b>-36.63</b>	0.90
<b>Makla</b>	<b>-6.04</b>	0.12	<b>-31.41</b>	0.53
<b>Yahav 116</b>	<b>-6.60</b>	0.06	<b>-39.56</b>	0.45
<b>Yahav 6</b>	<b>-7.51</b>	0.11	<b>-47.83</b>	0.66
<b>Yahav 16</b>	<b>-6.91</b>	0.10	<b>-42.38</b>	0.54
<b>Gofra</b>	<b>-4.60</b>	0.07	<b>-21.84</b>	0.12
<b>Tzofar 20</b>	<b>-8.38</b>	0.05	<b>-57.58</b>	0.13
<b>H. Tveria</b>	<b>-3.57</b>	0.10	<b>-16.00</b>	0.50
<b>Mineral</b>	<b>1.08</b>	0.06	<b>-4.24</b>	0.40
<b>Qedem</b>	<b>0.92</b>	0.10	<b>-4.49</b>	0.57

The data in Figure 5.8 can be divided into three clusters: Northern cluster, Dead Sea cluster and Arava Valley cluster, each of them shows a different trend of the stable isotopes.

The stable isotopes of the northern cluster lie close to the [EMWL](#), indicating that the the water is of meteoric origin. The samples in this cluster lie on a line that is shifted from the [EMWL](#) towards the [GMWL](#), indicating evaporation. [Mazor et al. \[1973\]](#) attribute this shift to a mixing between endmembers with different temperatures and salinities. [Arad and Bein \[1986\]](#) indicate that these end members that form the thermal water in Meitzar and Hamat Gader groups originate from different recharge zones in the north and south of Golan Heights, from different recharge heights, therefore the depletion is due to elevation effect, as explained in Section 2.4.3. The most depleted water in this cluster, from Meitzar 2 and Shamir, originates from the northern, higher parts of the Golan Heights and they are also among the deepest sampled wells, thus contain a higher amount of mantle derived helium, as explained before.

The stable isotopes of Ein Qedem and Mineral, in the Dead Sea cluster, lie on a mixing line between the [EMWL](#) and the mean value of  $\delta^{18}\text{O}$  in the Dead Sea (4‰) [[Gat and Dansgaard, 1972](#)], showing evaporation effect. It is deduced from chemical analyse that the thermal springs along the Dead Sea consist of a mixing between local fresh water and ancient Dead Sea water, namely evaporated sea water [[Möller et al., 2007b](#)], which can explain the enrichment in  $\delta^{18}\text{O}$  and  $\delta^2\text{H}$  of the samples from the Dead Sea area.

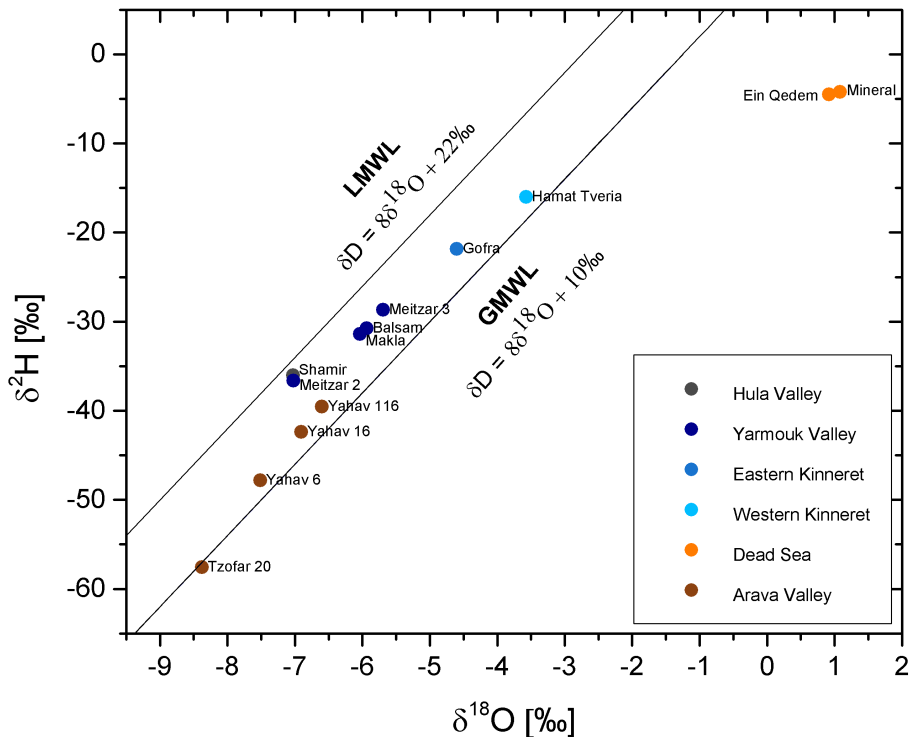


Figure 5.8: Stable isotopes signatures. The [Global Meteoric Water Line \(GMWL\)](#) [[Craig, 1961a](#)] and [Eastern Mediterranean Meteoric Water Line \(EMWL\)](#) [[Gat and Carmi \[1970\]](#), cited by e.g. [[Gat and Dansgaard, 1972](#)]] are plotted for a better orientation, where the [EMWL](#) is considered as the local meteoric water line in Israel (LMWL), e.g. [Gat and Dansgaard, 1972](#) and [Möller et al., 2007a](#). The data for this graph is given in [Table 5.9](#).

The samples from Arava Valley are shifted from the [EMWL](#) and lie pretty close the the [GMWL](#). An explanation is found by [Gat et al., 1969](#) ; [Gat and Dansgaard, 1972](#) and [Möller et al., 2006](#), who refer to the water as ancient fossil water, suggesting that it might had recharged as the climate in the area was cooler and more humid than known in the present time. Additional trend which can be seen within this cluster is that Tzofar 20 lies away from the other samples from Ein Yahav. [Gat et al., 1969](#) and [Möller et al., 2007a](#) found that the chemical composition of Tzofar 20 is different from the composition of the wells of Ein Yahav, but interestingly similar to the composition of the water from Hamat Tveria in the north. They indicate that these waters were formed from the same primordial brine, that had splayed over over wide parts of the Dead Sea Transform. Interesting to notice is that these two samples distinct from the others by their relationship between helium isotopes and electrical conductivity, which support the findings of these authors.

Non of the samples is enriched in  $\delta^{18}\text{O}$  relative to other samples of the same geographic area, indicating no evidence of water-rock interaction, thus no evidence of high water temperatures. This supports the findings of [Gat et al. \[1969\]](#), who only found evidence of  $\delta^{18}\text{O}$  exchange in a depth of 3150 m, which is much deeper than the sampling sites in this work ([Table 3.2](#)).

## 6 Discussion

### 6.1 Spatial distribution of $^3\text{He}/^4\text{He}$

The isotope ratio  $^3\text{He}/^4\text{He}$  plays an important role in the determination of the origin of helium in the thermal waters along the Dead Sea Transform. The samples were taken from different geographic areas along the Israeli side of the Dead Sea Transform, from the Hula Valley in the north to the Arava Valley in the south, showing a trend in the  $^3\text{He}/^4\text{He}$  ratios.  $^3\text{He}/^4\text{He}$  is the highest in the northern samples and decreases towards the south. In order to visualize effects of geographic location on the helium isotopes, the helium isotopes concentrations and the ratio  $^3\text{He}/^4\text{He}$  are plotted and referred to a specific location. The city of Eilat is chosen, which is the southernmost city in Israel and is located on the Gulf of Eilat, also known as the Gulf of Aqaba (Figure 6.1). The data are arranged in three main clusters of three main regions: Samples from the north part of the sampling site, samples from the Dead Sea area and samples from Arava Valley.

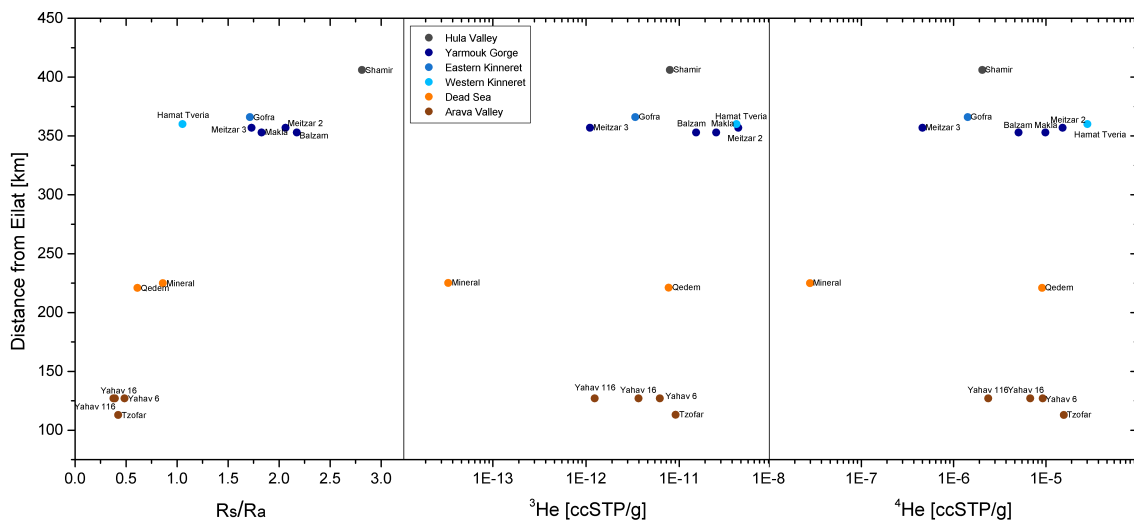


Figure 6.1: The distance from Eilat, at the Gulf of Aqaba, versus the helium isotopes concentrations and their ratio. The locations of the sampling sites can be found in Figure 3.5.

While the isotopes concentrations do not enable to distinguish between samples from different clusters, the  $^3\text{He}/^4\text{He}$  ratios show a distinct range in each cluster. The samples from the Arava Valley have the lowest  $^3\text{He}/^4\text{He}$  ratios, followed by the samples from the Dead Sea area, with medium  $^3\text{He}/^4\text{He}$  values and the samples from the north, which have the highest  $^3\text{He}/^4\text{He}$  ratios from all samples. Hence,  $^3\text{He}/^4\text{He}$  ratio, compared to the individual  $^3\text{He}$  and  $^4\text{He}$  concentrations, has a higher sensitivity to trace mantle derived helium.

The correlation between  $^3\text{He}/^4\text{He}$  and the geographic location of a sample increases from the south to the north of the Dead Sea Transform, leading to a larger diversity of  $^3\text{He}/^4\text{He}$  ratios in the northern samples compared to the southern ones (Figure 6.1). It can be explained by the fact that the samples from the south are located closer by each other compared to the samples from the north. Hamat Tveria and Shamir, for example, are located 50 km away from each other and have a difference of  $\sim 2.4 \cdot 10^{-6}$  in their  $^3\text{He}/^4\text{He}$  values while Tzofar 20 and Ein Yahav, that are located less than 20 km apart, have similar  $^3\text{He}/^4\text{He}$  values, with a difference of only  $\sim 6.5 \cdot 10^{-8}$ . Moreover, it is interesting to compare the two wells from Meitzar, in the north, with the three wells from Ein Yahav in the south. Even though the wells in each field contain water from different depths and aquifers, the  $^3\text{He}/^4\text{He}$  levels of the samples within each of these fields (Table 5.6) vary from each other by only 10 %.

## 6.2 Mantle, crustal and atmospheric components distribution

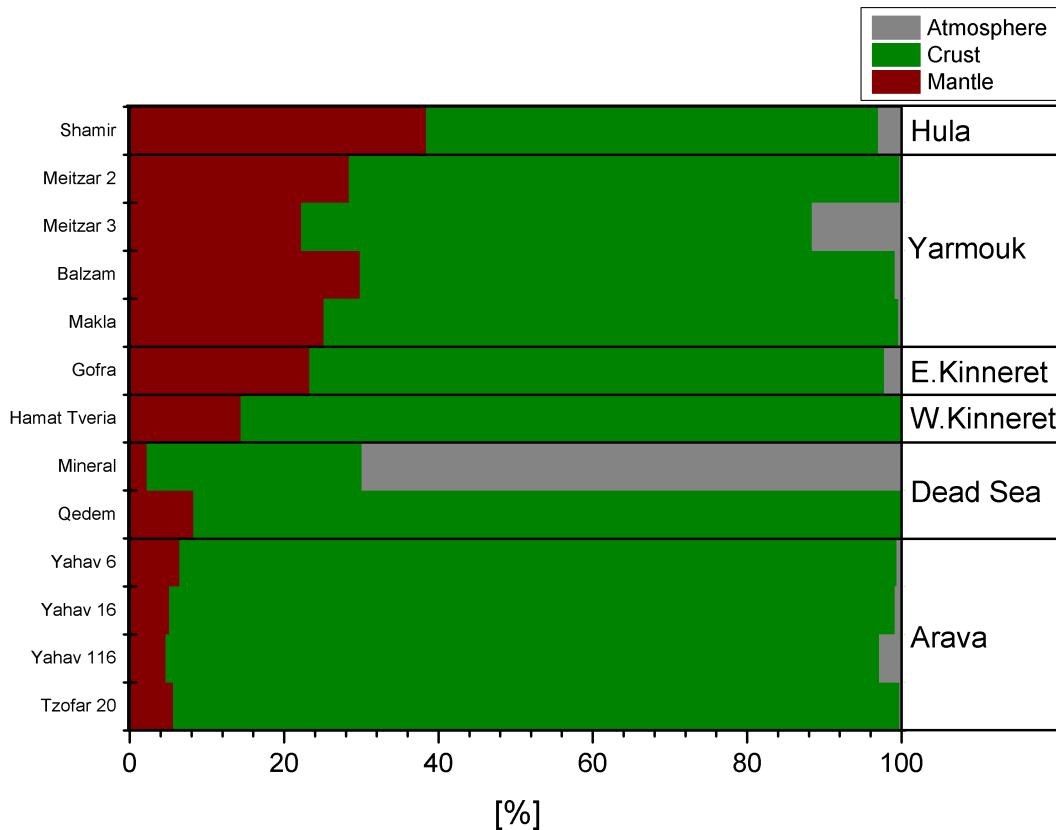


Figure 6.2: Percentages of mantle, crustal and atmospheric helium in the different regions along the Dead Sea Rift: Hual Valley, Yarmouk Valley, eastern and western shores of Lake Kinneret, the Dead Sea and Arava Valley. The data are taken from Table 5.7. Notice the north to south gradient of the mantle fraction. All the samples, aside from Mineral, contain a very low amount of atmospheric helium.

The total concentration of helium in each sample can be separated to contributions from

atmospheric, crustal and mantle sources (Figure 5.5), using the measured  $^3\text{He}/^4\text{He}$  ratios and the typical ratios of each of the endmembers (Table 2.1), as explained in Chapter 2. The distribution of these components in different regions along the Dead Sea Transform is shown in Figure 6.2. All samples, except of Mineral, contain mostly helium of crustal origin, which makes sense since these thermal waters circulate in the crust. Mineral and Meitzar 3 contain a significant contribution of atmospheric helium due to air infiltration during the sampling process (see Appendix A.5). The rest of the samples in all regions show less than 5 % atmosphere derived helium, meaning that more than 90 % of the helium is terrigenic. In addition, no difference is seen in the share of the atmospheric helium component in springs compared to wells. The increase mantle derived helium from south to north is noticed in Figure 6.2, as well as an increase from the western to eastern sides of Lake Kinneret. The maximal  $^3\text{He}/^4\text{He}$  of  $2.8 R_a$  is obtained in Shamir. For comparison, Torfstein et al. [2013] measured a ratio  $^3\text{He}/^4\text{He}$  of  $(6.6 \pm 0.7)R_a$  in basalts from the Golan Heights.

### 6.3 The geothermal structure of the Dead Sea Transform

Thermal springs are formed when water that flows in warm, usually deep layers discharges at the surface. Ascent can happen when high pressure pushes up the water or in areas where the crust is cracked, called break up points. Therefore thermal waters are usually found in tectonically active regions. The heat may come from different sources and as a result of different processes. The volatiles dissolved in the water can be useful for the understanding of the origin of this heat.

The thermal water of the Dead Sea Transform gains heat mostly from the normal geothermal gradient of  $\sim 25$  K/km [Starinsky et al., 1979 and Arad and Bein, 1986], which leads to higher temperatures in greater depths. The temperatures of the sampled wells are analysed in respect to their average screens, which correspond to the depth of ascent. Springs are not analysed since the original depth from which water is ascending is not known. Figure 6.3 shows that the sampled wells from the southern part of the sampling area have more or less a normal behaviour, which means that water from higher depths have higher temperatures. On the other hand, the samples from the northern part of the sampling area are scattered and show no correlation between the depth and water temperature.

The wells presented in Figure 6.3 can be divided into two groups with different trends: The wells of Meitzar and the rest of the samples, which lie on a line with a different slope. The data in each group were linearly fitted and the corresponding temperature gradients were calculated. The southern samples, together with the sample of Shamir from the north, yield a temperature gradient of 14 K/km and the samples from Meitzar well field yield a gradient of 59 K/km. For comparison, Arad and Bein [1986] reported a temperature gradient of 40 K/km in the area of Meitzar and the Golan Heights. This enhanced temperature gradient is in good agreement with the heat flux anomaly found by Shalev et al. [2013] and shown in Figure A.12 in Appendix A.8. This additional heat source is attributed to magma cooling, during young magmatic activity according to Arad and Bein, 1986 ; Bein and Feinstein, 1988 ; Bajjali et al., 1997 ; Shalev et al., 2013 and Roded et al., 2013.

The relationship between helium isotopes and heat is examined in Figure 6.4. No correlation is seen between  $^3\text{He}/^4\text{He}$  ratio and water temperature, which supports the fact

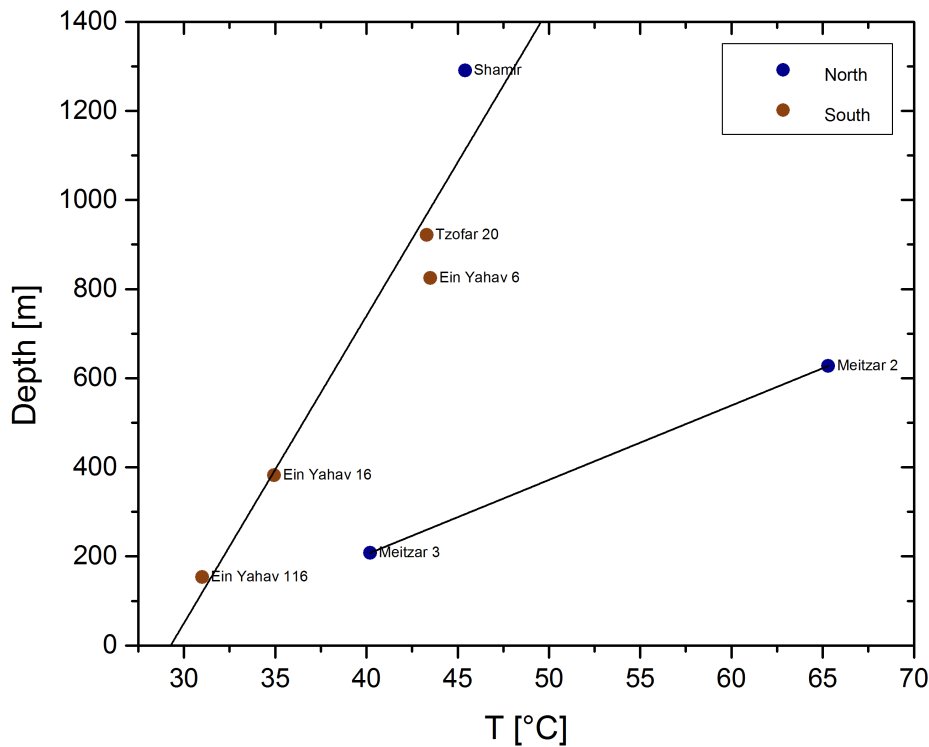
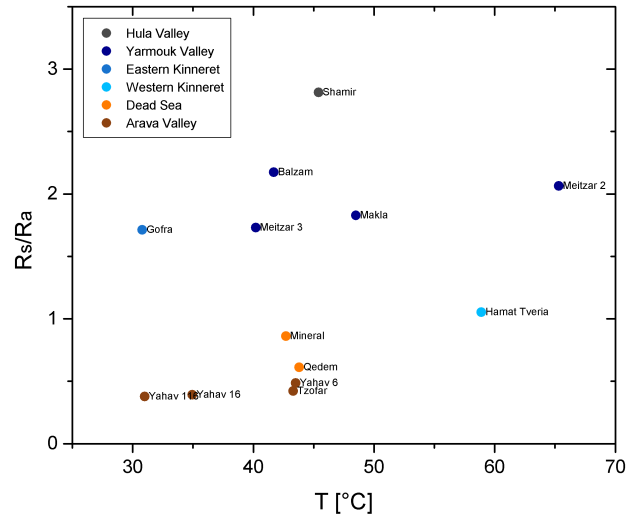


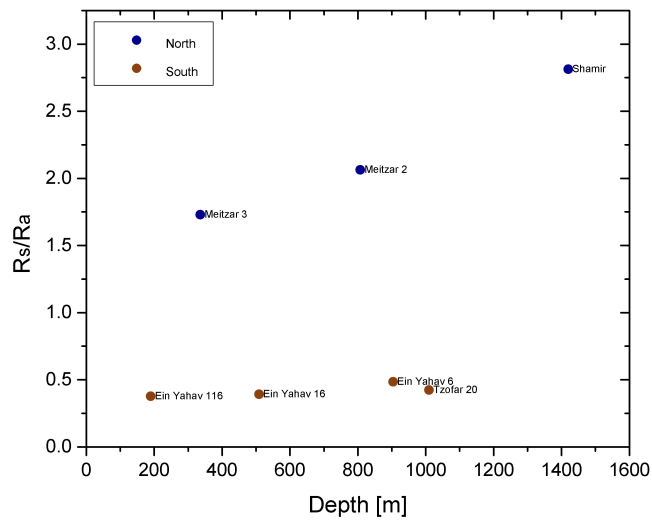
Figure 6.3: Depth of the sampled wells against water temperature. The depth corresponds to the averaged screen of the well (see Table 3.2). Note the different groups of samples from Meitzar and the rest of the samples. The samples in each group were linearly fitted (solid grey lines) in order to calculate temperature gradients. The calculated temperature gradients are 59 K/km for the samples from Meitzar and 14 K/km for the rest of the samples.

that not only thermal waters have relatively high  $^3\text{He}/^4\text{He}$  ratios, but also colder water. Notice the isotopic ratio of the spring Ein Gofra, on the east shore of Lake Kinneret. This sample has a ratio of  $^3\text{He}/^4\text{He}$  that is similar to the  $^3\text{He}/^4\text{He}$  ratios of the thermal springs in Yarmouk Valley (Figure 5.4), in spite of its relatively low water temperature (30.8 °C). Two explanations are suggested: 1) The magma in the mantle underlying this spring has already cooled down, but helium is still escaping from it into the groundwater in this area. 2) Mantle derived helium does not affect the water temperature, but is increased in deeper layers. This indicates that the old water of Ein Gofra might come from a depth of at least a few hundred of meters below the surface and retains the mantle derived helium incorporated at that depth. The lower temperature in Ein Gofra might be a result of a slow ascending of the water in the ground.

A change in the helium flux from the mantle with the depth of the well is noticed. It can be seen in Figure 6.4(b) that the  $^3\text{He}/^4\text{He}$  ratio of the northern samples is increasing with depth and is pretty constant for the southern samples. It is shown in Figures 6.2 and 5.5 that the major amount of helium in most samples is of crustal origin, therefore it is suggested that  $^3\text{He}/^4\text{He}$  decreases in the north due to dilution of the mantle derived



(a)



(b)

Figure 6.4:  $^3\text{He}/^4\text{He}$  ratio versus water temperature (a) and depth of the sampled wells (b), determined by the average screen of the well.

helium with radiogenic helium from the crust. Since all samples contain some fraction of mantle derived helium, it is not clear if the mantle intrusion into the crust is constant along the Dead Sea Transform or increases from south to north.

[Torfstein et al. \[2013\]](#) suggest two explanations to the differences between the contributions of mantle derived helium in the north and south of Israel. The first possibility is that there is a constant helium flux from the mantle into the crust along the Dead Sea Transform, which is more diluted by radiogenic helium from the crust in the southern regions of the Dead Sea Transform. The second possibility suggests that more helium is escaping from the upper mantle in the northern regions of the Dead Sea Transform. According to [Torfstein et al. \[2013\]](#), young magmatic activity took place in all the sampling areas, in the north and the south, therefore it cannot explain the higher  $^3\text{He}/^4\text{He}$  ratios in the northern part of the sampling area. It is interesting to look at the samples from Meitzar and Ein Yahav fields in [Figure 6.4\(b\)](#), located in the Yarmouk Valley and Arava Valley, respectively. Two trends can be seen: 1) The samples from Meitzar 2 and Meitzar 3 show an increase in the mantle derived helium with depth, while Ein Yahav 6, Ein Yahav 16 and Ein Yahav 116 have a similar mantle derived helium component. 2) Meitzar 3 is only about 150 m deeper than Ein Yahav 116 and has a value of  $^3\text{He}/^4\text{He}$  which is about 4.5 times higher. On one hand, the first trend supports the idea of dilution of the mantle derived helium in the northern samples by helium from local groundwater. On the other hand, the second trend supports the possibility of an enhanced mantle derived helium component in the north. The lack of evidence for dilution in the south can be explained by the fact that the crust which underlies the Arava Valley is about 1.4 times thicker than the crust underlies the north part of the sampling area, as indicated by [Torfstein et al. \[2013\]](#) and shown in [Figure 3.3](#). Therefore the samples there might be more diluted and are less affected by mixing.

It is not so clear whether higher  $^3\text{He}/^4\text{He}$  ratios in the northern sampling sites are due to enhanced intrusion of mantle derived helium there or stronger dilution by  $^3\text{He}/^4\text{He}$  ratios in the south, which reduces the measured  $^3\text{He}/^4\text{He}$  ratios in the groundwater there. It is possible that a different faulting pattern in the north enables more mantle derived helium to reach the groundwater.

The examination of the change in the  $^3\text{He}/^4\text{He}$  ratio with the well depth confirms the idea suggested by [Torfstein et al. \[2013\]](#), of two possible patterns of mantle derived helium intrusion into the crust. However,  $^3\text{He}/^4\text{He}$  ratios in thermal waters from the Jordanian side of the Dead Sea Transform, measured by [Kaudse \[2014\]](#), show a different trend. No decrease in the measured  $^3\text{He}/^4\text{He}$  ratios from north to south is observed, but rather a local anomaly in the  $^3\text{He}/^4\text{He}$  ratios in the area between the Dead Sea and Lake Kinneret. Moreover, [Kaudse \[2014\]](#) also found a correlation between high measured  $^3\text{He}/^4\text{He}$  ratios and local heat flux.

## 6.4 Other isotopes as tracers for mantle flux

### 6.4.1 Carbon isotopes

The  $\delta^{13}\text{C}$  values are in good agreement with measurements from other studies [[Mazor et al., 1973](#) and [Rosenthal, 1994](#)]. The results show no correlation between  $\delta^{13}\text{C}$  and geographic locations of the samples. It is not so simple to interpret the origin of  $\text{CO}_2$  in

the water only from  $\delta^{13}\text{C}$  since the isotope signatures of the different sources overlap, as shown in Figure 2.8.

The data of  $\text{CO}_2/{}^3\text{He}$  ratios from Torfstein et al. [2013], combined with  $\delta^{13}\text{C}$  in the three endmember mixing model (Figure 5.7) show no mantle derived  $\text{CO}_2$  component in the water (Section 5.4).  $\delta^{13}\text{C}$  was indeed not necessary for the determination of the mantle endmember share in the water and could be calculated by Torfstein et al. [2013], by inserting  $\text{CO}_2/{}^3\text{He}$  into Equation 2.50.

### 6.4.2 Stable isotopes

The measured  $\delta^{18}\text{O}$  and  $\delta^2\text{H}$  are similar to values obtained by other studies [Mazor et al., 1973 ; Mazor et al., 1980 ; Rosenthal, 1994 and Möller et al., 2006]. No evidence was found of interaction between water and crustal rocks.

As mentioned in Section 5.5, the sample from Tzofar 20 was attributed to recharge in a cooler and more humid climate in ancient time. In contrast, the NGT calculated for Tzofar 20 is more than  $30^\circ\text{C}$ , which is even more than the annual mean temperature at the present time. The reason for this contradiction is not very clear, but a possible explanation is the existence of a deep unsaturated zone at the recharge area. In such a case, the water keeps exchanging noble gases with air in greater depth, where the ground temperature increases due to the normal geothermal gradient. Therefore, the NGT can be higher than the local air temperature.



## 7 Summary and outlook

Thermal waters in Israel were analysed in order to identify local intrusions of volatile gases from the mantle into the crust. Thirteen samples were taken from thermal wells and springs along the Israeli side of the Dead Sea Transform. The sampling area included, from north to south: Hula Valley, Lake Kinneret, Yarmouk Valley, the Dead Sea area and Arava Valley. The sampling sites are shown in Figure 3.5. Helium, which is among the gases that are escaping from the mantle, was used as the main tracer of the mantle intrusions. The isotope ratio  $^3\text{He}/^4\text{He}$  of the water was compared to the typical ratio in the upper mantle in order to determine the amount of mantle derived helium within the sampling area.

Water temperature, electrical conductivity and alkalinity were measured directly in the field. Samples of groundwater for analysis of  $^3\text{H}$ ,  $\delta^{13}\text{C}$  and stable isotopes ( $\delta^{18}\text{O}$  and  $\delta^2\text{H}$ ) were collected in bottles. Groundwater for noble gas samples was collected in copper tubes. The noble gas concentrations were measured by mass spectrometry at the IUP. The measured noble gas isotope concentrations were used for analysing  $^3\text{He}/^4\text{He}$  ratios and for Noble Gas Temperature (NGT) determination.

To determine the different helium sources, the total helium concentration was decomposed. Only small amounts of tritium were found in the samples. Thus, the tritiogenic component could be neglected. By comparing the ratios of  $^3\text{He}/^4\text{He}$  and Ne/He, terrigenous helium was separated from atmospheric helium. Finally, atmospheric, crustal and mantle derived helium could be distinguished from each other, considering the typical  $^3\text{He}/^4\text{He}$  ratios of these three reservoirs.

Different geographic areas show different  $^3\text{He}/^4\text{He}$  ratios. The highest ratios were found in samples from the northern part of the sampling area (Hula Valley, Yarmouk Valley and Lake Kinneret), followed by lower  $^3\text{He}/^4\text{He}$  ratios measured in the Dead area and the southernmost samples, from Arava Valley, which showed the lowest  $^3\text{He}/^4\text{He}$  ratios. The analysis revealed that the helium origin is predominantly terrigenous, containing mostly radiogenic helium from the crust. Mantle derived helium was found in all the samples, ranging from 2.2% to 38.4% of the total helium concentration. Only the sample from Mineral well consisted mostly of atmospheric derived helium, but this is attributed to atmospheric contamination during sampling. The results confirm the findings of Torfstein et al. [2013] who saw a similar trend of enhanced  $^3\text{He}/^4\text{He}$  values in the northern samples relative to the southern samples. However, thermal waters from the Jordanian side of the Dead Sea Transform show local variations of  $^3\text{He}/^4\text{He}$  ratios, but no clear north-south trend [Kaudse, 2014].

Furthermore, the relationship between water temperature, depth of ascent and the  $^3\text{He}/^4\text{He}$  ratio in wells was examined. All the analysed samples, except of both wells from Meitzar, have a temperature-depth dependency corresponding to a temperature gradient which is lower than the normal geothermal temperature gradient. The analysis of water from the wells of Meitzar implies a temperature gradient which is much higher than the normal

geothermal gradient, indicating a local heat anomaly. This is supported by data of heat flux in Israel, reported by [Shalev et al. \[2013\]](#), who indicated an elevated heat flux around the Yarmouk Valley. No correlation was found between the  $^3\text{He}/^4\text{He}$  ratio and the water temperature. The relationship between  $^3\text{He}/^4\text{He}$  ratios in wells and the depth of the wells is different for samples from the northern and southern parts of the sampling area. Whereas the northern samples show a clear increase of the  $^3\text{He}/^4\text{He}$  ratio with the well depth,  $^3\text{He}/^4\text{He}$  ratios of the southern samples do not vary much. This difference between the north and south, together with north-south trend seen for the  $^3\text{He}/^4\text{He}$  ratios, suggest enhanced intrusions of helium from the mantle in the northern areas along with a stronger dilution of the  $^3\text{He}/^4\text{He}$  ratio by the crust in southern areas.

In addition to the analysis of mantle derived helium,  $\delta^{13}\text{C}$  was measured in order to trace mantle derived  $\text{CO}_2$ . Only four samples out of thirteen show a typical  $\delta^{13}\text{C}$  isotope signature of mantle  $\text{CO}_2$ . Thus, data of  $\text{CO}_2/^3\text{He}$  from [Torfstein et al. \[2013\]](#) were combined with the  $\delta^{13}\text{C}$  data to analyse mixing between mantle, limestone and sediment derived  $\text{CO}_2$  components. A model from [Sano and Marty \[1995\]](#) was used to estimate the relative contributions of the different components to the total concentration of  $\text{CO}_2$ . However, the model yielded unreasonable values. Therefore, a lower  $\text{CO}_2/^3\text{He}$  ratio was inserted into the model equations, which led to reasonable results, showing clearly that the  $\text{CO}_2$  in the water is not of a mantle origin. These results are in agreement with findings of [Torfstein et al. \[2013\]](#), who found no evidence of mantle  $\text{CO}_2$  in their samples.

Stable isotope data shows that all waters are of meteoric origin. Their distribution reflects different recharge conditions, i.e. recharge altitudes and/or recharge times. Furthermore, no evidence for clear groundwater-rock interaction is found, which would take place at temperatures above  $100^\circ\text{C}$ . This means that all sampled water did not circulate deep enough, where such effects could impact the stable isotope composition.

More information of the recharge conditions was obtained by [NGT](#) determination. The measured noble gas concentrations were fitted with the [CE](#) excess air model. The resulting temperatures are close to the mean annual air temperatures in the Dead Sea Transform at the present time. The fact that the [NGTs](#) of the samples from Arava Valley correspond to the annual mean temperature or are even higher contradicts the explanation of the stable isotope trend there, which suggests recharge in a cooler climate. A possible explanation would be that the unsaturated zone in the recharge area was deep enough, that the water temperature was influenced by the geothermal gradient before it lost contact with the atmosphere, which had led to a higher [NGT](#) and therefore do not reflect the mean annual surface temperature but the temperature at a deep groundwater table.

Since in this work almost all hot springs and wells in the Israeli side of the Dead Sea Transform were analysed, further investigations should be performed for cold springs in the same region. Based on the measurement from Ein Gofra, where the water temperature was quite low ( $30^\circ\text{C}$ ), it can be expected to find  $^3\text{He}/^4\text{He}$  ratios in cold waters, which are similar to the  $^3\text{He}/^4\text{He}$  ratios measured in the thermal waters from the same geographic area. Moreover, the analysis of water from cold springs could provide important and interesting new information, especially in the area between Lake Kinneret and the Dead Sea, where no thermal wells or springs are accessible.

# A Appendix

## A.1 Ostwald solubility calculation

Table A.1: Coefficients for solubility calculation (Equation 2.8) from Benson and Krause Jr. [1976].

Noble gas	$a_0$ [-]	$a_1$ [K]	$a_2$ [K <sup>2</sup> ]
He	-5.0746	-4127.8	627250
Ne	-4.2988	-4871.1	793580
Ar	-4.2123	-5239.6	995240
Kr	-3.6326	-5664.0	1122400
Xe	-2.0917	-6693.5	1341700

## A.2 Mixing ratios of noble gases

Table A.2: Atmospheric volume mixing ratios of noble gases in dry air.

Noble gas	mixing ratio
He	$(5.24 \pm 0.05) \cdot 10^{-6}$
Ne	$(1.818 \pm 0.0004) \cdot 10^{-5}$
Ar	$(9.34 \pm 0.01) \cdot 10^{-3}$
Kr	$(1.14 \pm 0.01) \cdot 10^{-6}$
Xe	$(8.7 \pm 0.1) \cdot 10^{-8}$

## A.3 Stable isotopes notation

The isotope ratio  $R$  is defined as:

$$R \equiv \frac{\text{Abundance of rare isotopes}}{\text{Abundance of common isotopes}}$$

The delta notation is defined as:

$$\delta \equiv \frac{R_{\text{sample}} - R_{\text{standard}}}{R_{\text{standard}}} = \left( \frac{R_{\text{sample}}}{R_{\text{standard}}} - 1 \right) \cdot 1000 \text{‰}$$

## A.4 Locations in Israel

Table A.3: Locations in Israel, marked on the map in figure A.1 from Rosenthal et al. [2009].

Aqaba (57)	Hazeva (51)	Nablus (25)	Tabigha springs (7)
Ashdod (37)	Hebron (44)	Paran-Zin syncline (55)	Taninim river (15)
Banias River (3)	Hula Valley (5)	Pezael (30)	Tiberias hot springs (9)
Beer Tuvia (45)	Jenin (21)	Qalqiliya (28)	Tubas (22)
Beer Sheva (47)	Jericho (35)	Qane spring (42)	Tul Karem (27)
Bet She'an Valley (19)	Jerusalem (36)	Qilt (34)	Uja (32)
Betlehem (39)	Jordan Valley, upper (6)	Ramallah (33)	Yahav wells (53)
Dan River (2)	Judea syncline (40)	Salfit (26)	Yarmouk River (11)
Eilat (56)	Lisan Peninsula (48)	Samar spring (43)	Yizrael Valley (17)
Ein Yahav (52)	Makhtesh Ramon (54)	Samaria (24)	Zemach (12)
Fuliya springs (8)	Menashe reservoir (16)	Samaria syncline (23)	Zofar (53)
Haon (10)	Mt. Carmel (14)	Samia (31)	Zukim springs (41)
Harod Valley (18)	Mt. Gilboa (20)	Sdom (49)	
Hasbani River (4)	Mt. Hermon (1)	Shefela (38)	
Hatira (50)	Naaman River (13)	Shiqma reservoir (46)	

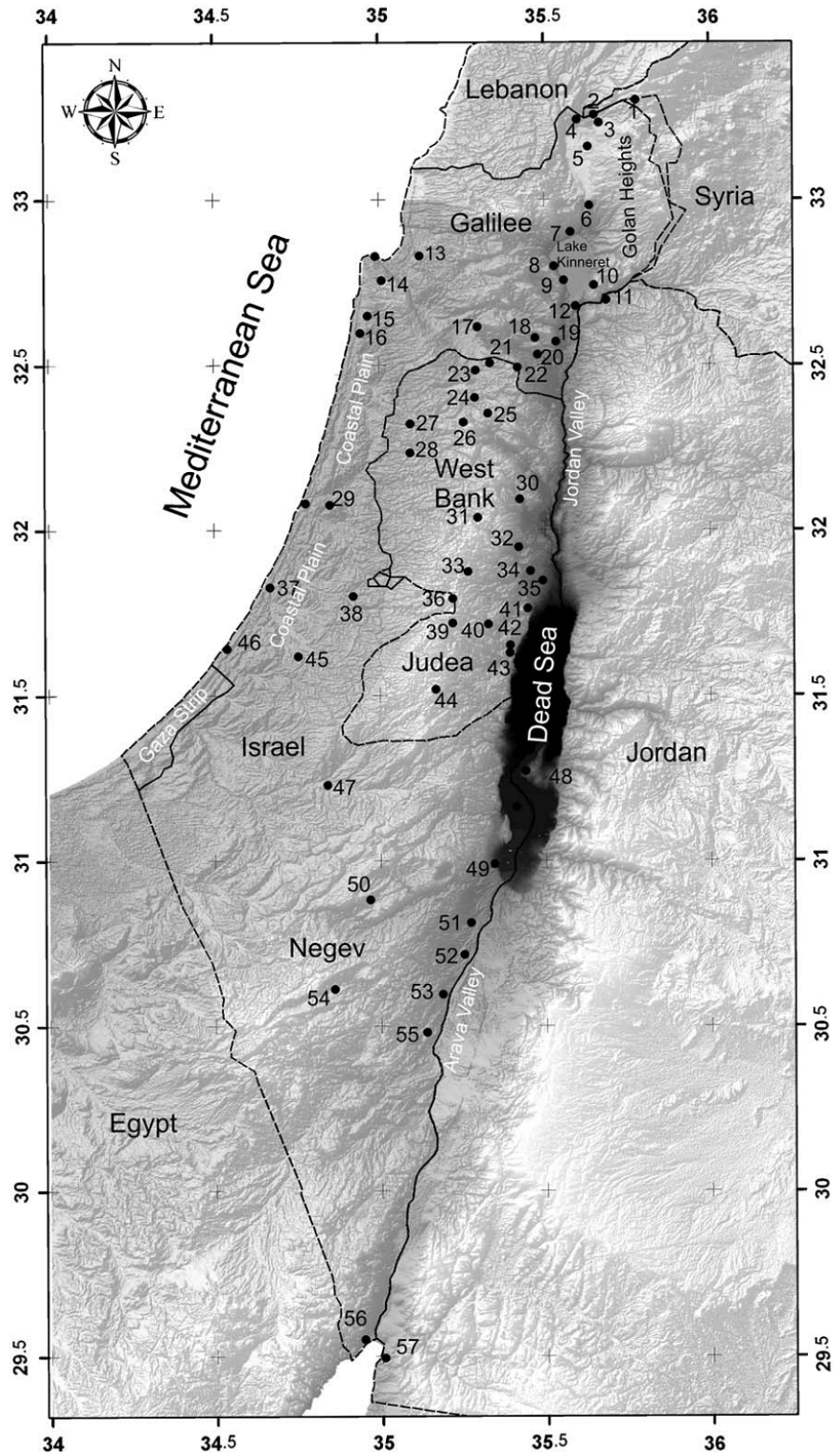


Figure A.1: General location map of Israel and the Jordan Rift Valley from Rosenthal et al. [2009]. For the list of locations see Table A.3

## A.5 A detailed description of the sampling sites and the sampling process

The purpose of this part is to give the reader more information about the main characteristics of the sampling sites sampled in the frame of this work and the problems that have arisen during the sampling process. The sampling sites are presented in an alphabetic order. Note that a few of the names start with “Ein”, which is the Hebrew word for “spring”. However, one should pay more attention, because not all the places that start with “Ein” are springs. A good example for it are the three wells of Ein Yahav in the Arava in the south of Israel. Generally, the natural springs become fewer in the south of Israel, in the Negev desert.

### Ein Qedem

This is one of the thermal springs that were exposed during the decrease of the sea level. It is located about 30 meters away from the Dead Sea, 6 km northern from Kibutz Ein Gedi. The spring is surrounded with sink holes and a moist soil. There is one main spring and another few smaller springs that appear and disappear every few months. The water had a strong smell of sulfur and the flow rate was low. Therefore, the noble gas sample was taken by sucking up the water through the water hose and the copper tube. This is the saltiest water that was sampled in this work, with salinity of about 190 gr/kg [Starinsky, 1974; Stern, 2010]. It was sampled right after Mineral, which has a similar salinity. As a result, the sensor used to measure electrical conductivity couldn't reach zero in the air, even after it was washed in fresh water. However, it was back to normal on the next day.



(a) Ein Qedem spring on the view of the Dead Sea and the mountains of Jordan (b) The spring pool (photograph of Paul Bauer)

Figure A.2: Ein Qedem springs

### Ein Yahav

This well field is located in the northern Arava, about 30 km away from the Dead Sea. It consists of three artesian wells, numbered 6, 16 and 116, with different depths, screens and different water temperatures between 31 °C and 43.5 °C. Samples were taken from all the three. Ein Yahav 6 and Ein Yahav 116 had a sampling tap and Ein Yahav 16 was broken at that time, so the water was delivered to an alternate point, about 10 meters away from the drill (figure A.3).



(a) Ein Yahav 6



(b) Ein Yahav 16 (left) and Ein Yahav 116 (right) (c) The alternative outflow of Ein Yahav 16, due to a problem in the drilling

Figure A.3: Ein Yahav wells

The water of Ein Yahav 6 was the warmest and had a light smell of sulfur. It became grey after about 15 minutes in the air. A water hose with a copper tube was connected to the sampling tap and noble gas samples, as well as the other samples, were taken without any problems.

The pipe of Ein Yahav 16 was under construction, therefore the water was delivered to another pipe a few meters away, so that it could still be used. As can be seen in Figure A.3 there was no sampling tap and the flow was pretty strong. The water had a smell of unrecognised chemicals. The samples were taken directly from the pipe. For the noble gas samples, the water hose was placed in the outflow pipe. Small bubbles were formed in the hose.

Ein Yahav 116 had the coldest water out of the three. The sampling process was similar to that of Ein Yahav 6, with no special events.

#### Gofra

Gofra is the name of one of the beaches on the east side of Lake Kinneret. It is called after the word Gofrit, which means sulfur in Hebrew and describes very well the strong smell that comes from the spring Ein Gofra on the beach (picture A.4). This was the site with the lowest water temperature (30.8 °C). The water springs under a rock and is collected in a small shallow pool. The water in the pool contains white soft sulfur sediments and bubbles arise from the bottom. The discharge pace is low, therefore the noble gas samples were taken by inserting the water hose under the rock, as close as possible to the spring itself and sucking water until it filled the copper tube. A few smaller unpermanent springs were observed around the main spring.

#### Hamat Gader

Hamat Gader is a spring field of five hot springs, on the southern slopes of Golan Heights, on the border with Jordan. The word Hamat comes from the Hebrew “Ham”, which means “hot” and Gader means “fence”, named after the fence of the border with Jordan, that passes right at the side of this field. The place is also known from the big resort there. Samples were taken from two of the springs, Ein Makla and Ein Balzam, that have the highest temperatures. According to information from Hamat Gader Resort, it can be assumed that the water springs from a depth of about 2 km.

Ein Makla is a very hot spring, with a temperature of 48.5 °C, that is located in an



Figure A.4: Ein Gofra spring at Gofra Beach, Lake Kinneret



(a) The archaeological site from the Roman time. (b) Ein Makla spring. Notice the sulfur sediments on the right side. Behind are the highlands of Jordan



(c) Ein Balzam spring. This is also one of the hot pools in Hamat Gader resort. The floor was left as it is and covered with gravel in order to enable the water to flow out freely

Figure A.5: Ein Makla and Ein Balzam in Hamat Gader

archaeological site from the Roman time (see picture A.5). The spring forms a pool, which has a depth of about 3 m and a diameter of about 5 m. The pool is covered by a black sheet. There are sulfur sediments on the water with a very strong smell. Bubbles were rising from the bottom of the pool, each time from a different point and the water came out from the ground probably in more than one points in the pool. Since the water was too hot, it was only possible to stand in it with special boots that blocked the heat for a while. Gloves were also needed in order to fill up the bottles. Since it was not clear, where exactly the spring point is, the water hose of the noble gas sample was thrown into the middle of the pool and we made sure that no sulfur pieces would block it. My father held the other side and sucked water into the copper tube. I knocked on the sides of the copper tube to make sure there were no air bubbles trapped inside and closed it with the ratchet. Four noble gas samples were taken in Ein Makla for surely having good samples from this site.

The other spring that was sampled in Hamat Gader is called Ein Balzam. It is also called "The spring of scents", probably because of the prominent sulfur smell there. According

to information from Hamat Gader Resort, the flow rate there is 500 - 700 m<sup>3</sup>/h and it is opened for the visitors of the resort. The place of the spring is built as a roofed bathing pool, with built walls, and the natural bottom, with gravel on it, so that the water can come out freely. The pool is about 10 x 5 m big. The water is about 42 °C so that it was possible to go inside for about ten minutes to take the samples. The lifeguard showed us where it is believed that the water comes out. The noble gas samples were taken in a similar way to Ein Makla. I was holding one side of the water hose with the foot, so that it stayed close to the bottom and my father sucked water from the other side. It was helpful for the sucking to first blow air out of the hose as it was already in the water.

#### Hamat Tveria

This ancient spring field is located in the city of Tiberias, on the west side of Lake Kinneret. A medical bath from ancient time is found at this site. There are 17 hot springs, some of them are under the ground and nowadays there is a park for visitors and thermal pools that use the springs water. The water is very hot (56 °C) and contains sulfur, which gives nice colours to the canals in the park. The sample was taken in the main spring, which appears in Figure A.6. The water springs from the hole in the built wall and is delivered to the hot pools of the resort. In order to take the samples, the water hose of the noble gas sample was inserted a few centimeters into the spring and was held by a stone that was inserted there too. Three noble gas samples were taken, due to a stuck screw in one of the aluminium racks. I noticed small bubbles that were formed in the bottles and hoses as the water came out of the spring, which might be an indication of degassing.



(a) The main spring

(b) The Roman spring

Figure A.6: Hamat Tveria springs

#### Meitzar

Meitzar is a well field on the southern slopes of the Golan Heights on the border with Jordan, close to Hamat Gader. Two out of the three boreholes there were sampled: Meitzar 2 and Meitzar 3. Both are artesian and have a sampling tap close to the drilling point, where the water hose was connected (see picture A.7).

Meitzar 2 was the sampling site which had the highest temperature of 65.3 °C. Little bubbles were forming during the sampling, making a bigger bubble at the end of the copper tube. The water hose was therefore bent a little bit and the big bubble was gone. The smaller bubbles remained and might be a result of degassing.

The sampling process of Meitzar 3 was similar to that of Meitzar 2. The pressure in the

sampling tap was pretty low, so that less water came out. As a result, bubbles were formed in the water hoses and the copper tubes. I waited until the bubbles were minimal and closed the copper tubes.



(a) Meitzar 2

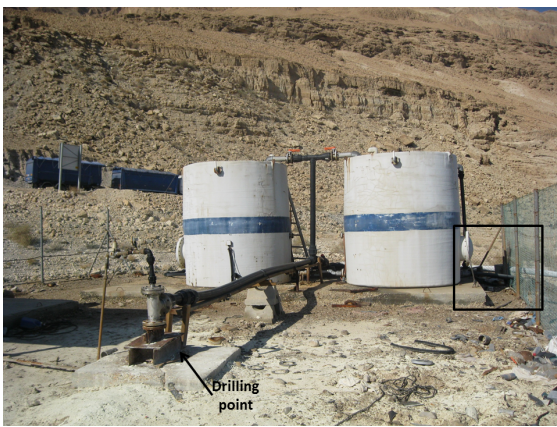


(b) Meitzar 3

Figure A.7: Meitzar well field

Mineral

Mineral is a beach on the northern-east side of the Dead Sea. The well is artesian and provides water to the thermal pool located on the beach. As shown in picture A.8 water from the well is pumped to the upper part of the containers and then flows inside. Air contact obviously occurs in the containers. In addition, the pumping is done alternately, which means that water is not always flowing in the containers. The water had a smell of sulfur and it contained small unrecognized soft white pieces. It was only possible to take the samples from an outflow pipe that was located at the bottom of one of them. The sampling is shown in Figure A.8c. The water hose was inserted into the outflow pipe and a stone was pushed there, to prevent the hose from slipping out of the pipe, due to the strong flow. Some bubbles were formed on the outflow side of the copper tube, so we bent the water hose close to the connection with the tube and the bubbles were gone.



(a) The drilling site of Mineral beach. The square marks the outflow pipe, which can be seen more detailed in (b)



(b) The inside of one of the containers



(c) The outflow pipe, from which the samples were taken

Figure A.8: Mineral borehole site

Shamir

Shamir is the northernmost site that was sampled. It is located on the northern slopes of the Golan Heights, close to Kibutz Shamir. There are three wells in this field, one of them is thermal. This thermal well was sampled. It is an artesian well with a maximal flow rate of 500 m<sup>3</sup>/h. There was a sampling tap close to the actual drilling point (see Figure A.9). Little bubbles were formed in the hoses.



Figure A.9: Shamir well on the northern slopes of the Golan Plateau. The noble gas sample is connected to the sampling tap, close to the drilling point, which is the vertical black column.

Tzofar

Tzofar 20 is a thermal well that belongs to Tzofar well field in the Arava. It was the southernmost site that was sampled for this work. The well is artesian and is about 1000m deep. As shown in Figure A.10, water comes out of the ground and flows through a 1.5m pipe into a pool. The tap on the pipe is most of the time closed, so that water doesn't come out all the time. It was opened a few minutes before samples were taken in order to wash out water that might have been in contact with air. The flow was not regulated and bubbles were flowing through the water hose of the noble gas samples. Smaller bubbles started to form in the hose, a few seconds after it came out of the well.



Figure A.10: Tzofar 20

## A.6 Neon and argon isotopic ratios

Table A.4: Neon and argon isotopic ratios calculated directly from WuCEM.

Sample	$^{20}\text{Ne}/^{22}\text{Ne}$	$\Delta^{20}\text{Ne}/^{22}\text{Ne}$	$^{36}\text{Ar}/^{40}\text{Ar}$	$\Delta^{36}\text{Ar}/^{40}\text{Ar}$
Gofra	<b>9.790</b>	0.005	<b>287</b>	6
Shamir	<b>9.793</b>	0.004	<b>296</b>	6
Meitzar 3	<b>9.791</b>	0.005	<b>299</b>	6
Balzam	<b>9.790</b>	0.005	<b>298</b>	6
Meitzar 2	<b>9.803</b>	0.005	<b>298</b>	6
Makla	<b>9.764</b>	0.004	<b>302</b>	6
Yahav 116	<b>9.793</b>	0.004	<b>297</b>	6
Yahav 6	<b>9.792</b>	0.004	<b>298</b>	6
Yahav 16	<b>9.787</b>	0.005	<b>296</b>	6
Tzofar 20	<b>9.768</b>	0.005	<b>289</b>	7
Hamat Tveria	<b>9.773</b>	0.005	<b>324</b>	6
Meinral	<b>9.784</b>	0.004	<b>288</b>	6
Qedem	<b>9.845</b>	0.006	<b>316</b>	7

## A.7 Noble gas concentrations of the second and third measurement runs

The tables containing the noble gas concentrations obtained from the second and third measurement runs can be found on the following two pages.

Table A.5: Concentrations of noble gas isotopes from the second and third measurements periods in [ccSTP/g]. Only helium isotopes could be measured in Ein Balzlam, since the heating element was accidentally turned on in the middle of the measurement.

Sample	Date	$2^{nd}$ measurement run							
		$^3\text{He}$	$\Delta^3\text{He}$	$^4\text{He}$	$\Delta^4\text{He}$	$^{20}\text{Ne}$	$\Delta^{20}\text{Ne}$	$^{22}\text{Ne}$	$\Delta^{22}\text{Ne}$
Shamir	14.05.2013	8.146E-12	3.138E-13	2.274E-06	1.354E-08	7.335E-07	2.634E-09	7.436E-08	2.586E-10
Balzam	14.05.2013	1.657E-11	6.185E-13	4.979E-06	3.194E-08	—	—	—	—
Meitzar 2	15.05.2013	4.791E-11	1.836E-12	1.572E-05	9.280E-08	1.646E-07	5.804E-10	1.677E-08	5.667E-11
Makla	21.05.2013	3.360E-11	1.059E-12	8.463E-06	5.740E-08	2.997E-06	1.068E-08	3.052E-07	1.040E-09
Yahav 116	21.05.2013	1.203E-12	5.725E-14	2.390E-06	1.426E-08	2.356E-07	8.244E-10	2.407E-08	8.021E-11
Yahav 16	22.05.2013	3.650E-12	1.351E-13	6.622E-06	4.414E-08	2.023E-07	7.079E-10	2.067E-08	6.905E-11
Gofra	23.05.2013	3.920E-12	1.473E-13	1.468E-06	9.729E-09	1.252E-07	4.436E-10	1.280E-08	4.335E-11
Tzofar 20	24.05.2013	1.244E-10	5.591E-12	2.172E-04	1.324E-06	1.123E-06	4.008E-09	1.147E-07	3.934E-10
Hamat Tveria	24.05.2013	4.412E-11	1.809E-12	2.820E-05	1.745E-07	9.312E-08	3.357E-10	9.537E-09	3.551E-11
$3^{rd}$ measurement run									
Hamat Tveria	12.06.2013	4.713E-11	1.803E-12	2.856E-05	3.257E-07	9.613E-08	4.943E-10	9.844E-09	5.562E-11
Mineral	13.06.2013	3.397E-14	2.935E-15	2.734E-08	1.906E-10	6.770E-08	3.522E-10	6.905E-09	3.943E-11
Qedem	14.06.2013	8.512E-12	3.845E-13	9.878E-06	7.533E-08	3.853E-08	2.044E-10	3.914E-09	2.499E-11
$2^{nd}$ measurement run									
Sample	Date	$^{36}\text{Ar}$	$\Delta^{36}\text{Ar}$	$^{40}\text{Ar}$	$\Delta^{40}\text{Ar}$	$^{84}\text{Kr}$	$\Delta^{84}\text{Kr}$	$^{132}\text{Xe}$	$\Delta^{132}\text{Xe}$
Shamir	14.05.2013	2.169E-06	5.562E-08	6.384E-04	1.952E-06	6.537E-08	9.103E-10	3.508E-09	7.801E-11
Balzam	14.05.2013	—	—	—	—	—	—	—	—
Meitzar 2	15.05.2013	1.337E-06	3.740E-08	3.967E-04	1.228E-06	5.064E-08	7.439E-10	3.054E-09	7.340E-11
Makla	21.05.2013	6.264E-06	1.537E-07	1.903E-03	5.927E-06	1.489E-07	2.028E-09	6.257E-09	1.397E-10
Yahav 116	21.05.2013	1.103E-06	3.243E-08	3.297E-04	1.052E-06	3.986E-08	6.006E-10	2.553E-09	6.975E-11
Yahav 16	22.05.2013	1.022E-06	3.083E-08	3.084E-04	1.011E-06	3.781E-08	5.411E-10	2.366E-09	5.341E-11
Gofra	23.05.2013	9.294E-07	2.914E-08	2.773E-04	8.842E-07	3.762E-08	5.268E-10	2.275E-09	5.109E-11
Tzofar 20	24.05.2013	3.179E-06	7.972E-08	1.006E-03	3.110E-06	8.651E-08	1.173E-09	3.788E-09	9.662E-11
Hamat Tveria	24.05.2013	6.911E-07	2.450E-08	2.101E-04	6.775E-07	2.892E-08	3.995E-10	1.902E-09	4.762E-11
$3^{rd}$ measurement run									
Hamat Tveria	12.06.2013	7.364E-07	4.179E-08	2.103E-04	1.344E-06	2.892E-08	4.066E-10	1.949E-09	4.301E-11
Mineral	13.06.2013	3.174E-07	2.690E-08	8.394E-05	5.448E-07	9.343E-09	1.646E-10	4.690E-10	2.949E-11
Qedem	14.06.2013	3.597E-07	2.779E-08	1.066E-04	6.813E-07	1.397E-08	2.325E-10	7.455E-10	4.821E-11

Table A.6: Noble gas concentrations from the second and third measurement periods in [ccSTP/g], ordered by measurement date. The concentrations from the first run are listed in chapter 5. Only helium could be calculated in Ein Balzam, since only helium isotopes were measured there (see table A.5).

Sample	<i>2<sup>nd</sup></i> measurement run									
	He	$\Delta$ He	Ne	$\Delta$ Ne	Ar	$\Delta$ Ar	Kr	$\Delta$ Kr	Xe	$\Delta$ Xe
Shamir	2.274E-06	1.354E-08	8.101E-07	2.664E-09	6.410E-04	1.954E-06	1.147E-07	1.597E-09	1.304E-08	2.901E-10
Balzam	4.979E-06	3.194E-08	—	—	—	—	—	—	—	—
Meitzar 2	1.572E-05	9.280E-08	1.819E-07	5.872E-10	3.982E-04	1.230E-06	8.884E-08	1.305E-09	1.136E-08	2.730E-10
Makla	8.463E-06	5.740E-08	3.311E-06	1.083E-08	1.910E-03	5.934E-06	2.613E-07	3.558E-09	2.327E-08	5.196E-10
Yahav 116	2.390E-06	1.426E-08	2.603E-07	8.339E-10	3.310E-04	1.054E-06	6.993E-08	1.054E-09	9.495E-09	2.594E-10
Yahav 16	6.622E-06	4.414E-08	2.236E-07	7.162E-10	3.096E-04	1.012E-06	6.633E-08	9.493E-10	8.800E-09	1.986E-10
Gofra	1.468E-06	9.729E-09	1.384E-07	4.487E-10	2.784E-04	8.854E-07	6.600E-08	9.242E-10	8.459E-09	1.900E-10
Tzofar 20	2.172E-04	1.324E-06	1.241E-06	4.057E-09	1.010E-03	3.114E-06	1.518E-07	2.058E-09	1.409E-08	3.593E-10
Hamat Tveria	2.820E-05	1.745E-07	1.029E-07	3.398E-10	2.109E-04	6.784E-07	5.073E-08	7.009E-10	7.072E-09	1.771E-10
<i>3<sup>rd</sup></i> measurement run										
Hamat Tveria	2.856E-05	3.257E-07	1.063E-07	4.998E-10	2.111E-04	1.346E-06	5.073E-08	7.134E-10	7.248E-09	1.600E-10
Mineral	2.734E-08	1.906E-10	7.480E-08	3.559E-10	8.431E-05	5.459E-07	1.639E-08	2.888E-10	1.744E-09	1.097E-10
Qedem	9.878E-06	7.533E-08	4.256E-08	2.068E-10	1.071E-04	6.823E-07	2.451E-08	4.080E-10	2.772E-09	1.793E-10

## A.8 Additional figures



(a) WTW sensor used for the temperature and electrical conductivity measurements.



(b) Alkalinity measurement with Salifert kit.



(c) Noble gas sample.

Figure A.11: Additional photos from the field and the laboratory.

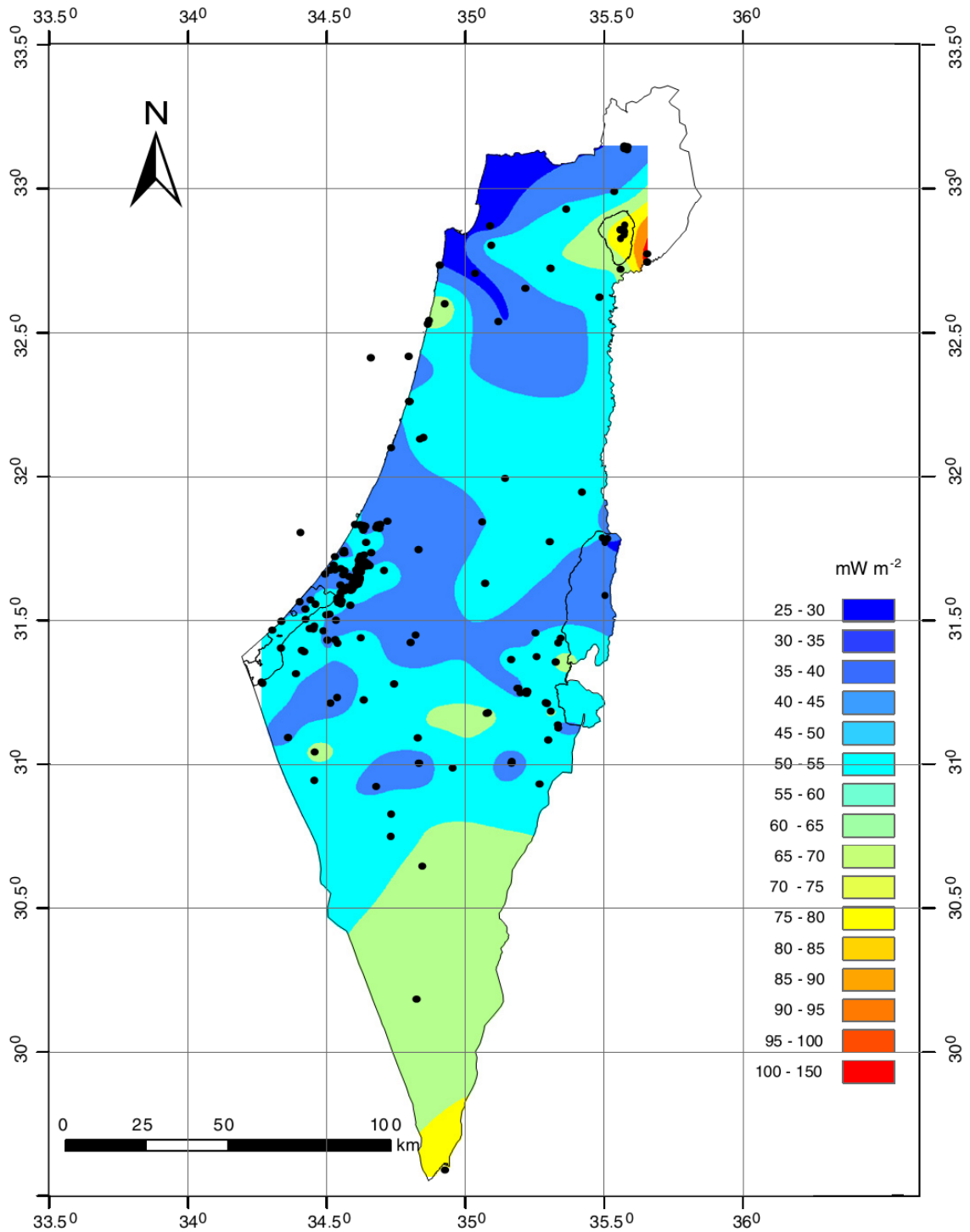


Figure A.12: Calculated geothermal heat flux in Israel, adopted from [Shalev et al., 2013]. The black dots refer to temperature measurements in boreholes. Notice the flux anomaly east of Lake Kinneret, in the Golan Heights.



# List of Figures

1.1	Interior layers of Earth . . . . .	11
2.1	Solubility versus temperature and salinity . . . . .	16
2.2	Noble gas components in groundwater . . . . .	17
2.3	Excess air models . . . . .	19
2.4	CE model derivation . . . . .	21
2.5	MORB and OIB . . . . .	23
2.6	Helium components . . . . .	24
2.7	Air correction explanation: $^3\text{He}/^4\text{He}$ versus $\text{Ne}/\text{He}$ in a sample . . . . .	25
2.8	$\delta^{13}\text{C}$ signatures of different sources of carbon in groundwater . . . . .	30
2.9	Stable isotopes: GMWL . . . . .	32
3.1	The Levant Rift . . . . .	34
3.2	Pull apart basin scheme . . . . .	35
3.3	The crust under the Dead Sea Transform . . . . .	36
3.4	Stratigraphic column of Israel . . . . .	38
3.5	Sampling sites locations . . . . .	40
4.1	Schematic description of MM5400 spectrometer . . . . .	43
4.2	Measurement process of the mass spectrometer . . . . .	43
5.1	NGTs results . . . . .	51
5.2	$^4\text{He}$ concentration versus $^3\text{He}$ concentration . . . . .	54
5.3	He concentration versus electrical conductivity . . . . .	55
5.4	$R_a$ versus $\text{Ne}/\text{He}$ . . . . .	59
5.5	Atmospheric, crustal and mantle derived helium . . . . .	60
5.6	$\delta^{13}\text{C}$ versus $^3\text{He}/^4\text{He}$ and mantle derived helium percentage . . . . .	64
5.7	Distribution of mantle, carbonate and sediments derived $\text{CO}_2$ in the samples . . . . .	66
5.8	Stable isotopes . . . . .	68
6.1	$^3\text{He}/^4\text{He}$ and helium isotopes concentrations versus the distance from Eilat . . . . .	69
6.2	Atmospheric, crustal and mantle derived helium in different regions along the Dead Sea Transform . . . . .	70
6.3	Depth versus water temperature of the sampled wells . . . . .	72
6.4	$^3\text{He}/^4\text{He}$ ratios versus temperature and depth of the sampled wells . . . . .	73
A.1	Israel locations . . . . .	81
A.10	Tzofar 20 . . . . .	90
A.11	Additional photos from the field and the laboratory . . . . .	94
A.12	Heat flux map of Israel . . . . .	95



## List of Tables

2.1	Average $^3\text{He}/^4\text{He}$ in the atmosphere, crust and mantle . . . . .	29
2.2	Isotopic signature of the main sources of carbon in groundwater . . . . .	31
3.1	General information about the sampling sites . . . . .	39
3.2	Wells data . . . . .	39
4.1	Atomic abundance factors of the measured noble gas isotopes . . . . .	45
5.1	Water parameters . . . . .	47
5.2	Noble gas isotopes concentrations . . . . .	48
5.3	Elemental noble gas concentrations . . . . .	49
5.4	NGTs results . . . . .	53
5.5	Tritium results . . . . .	56
5.6	$^3\text{He}/^4\text{He}$ and Ne/He ratios . . . . .	57
5.7	Atmospheric, crust and mantle derived helium components . . . . .	62
5.8	$\delta^{13}\text{C}$ and $\text{CO}_2/^3\text{He}$ . . . . .	63
5.9	Stable isotopes . . . . .	67
A.1	Vant Hoff equation coefficients . . . . .	79
A.2	Atmospheric volume mixing ratios of noble gases in dry air . . . . .	79
A.3	Israel locations . . . . .	80
A.4	Neon and argon isotopic ratios . . . . .	91
A.5	Noble gas isotopes concentrations: Additional measurement runs . . . . .	92
A.6	Noble gas concentrations: Additional measurement runs . . . . .	93



# Acknowledgments

First of all I would like to thank my supervisor, Prof. Dr. Werner Aeschbach Hertig, for the helpful explanations and ideas you provided me during the work. Thank you for giving me the opportunity, to carry out a field trip in Israel.

Tillmann Kaudse, thank you very much for your significant contribution to this work as my tutor, always making sure that things went on the right side, from the beginning to the end.

Special thank to Dr. Joseph Guttmann from Mekorot, for enabling me to take samples at the drilling wells of Meitzar, Ein Yahav and Tzofar and for providing necessary literature.

I would like to thank to all other sites owner, for allowing me to take samples there: Hilik from Mei Golan (Shamir drillings), Tami and Sharon from Israel Nature and Park Authority (Hamat Tveria springs), Oren and Ibrahim from Mineral Beach, Andrea and Moti from Hamat Gader Resort and Gofra Beach camping site.

Paul Königer from BGR in Hannover, special thanks for kindly measuring my stable isotopes samples. Adrian Walser and Giles Möhl, thank you for measuring  $\delta^{13}\text{C}$  and  $^3\text{H}$ .

I would like to thank to the people from my research group, especially Tillmann, Simon and Florian, for your help in the organization of the field trip, during the work in the laboratory, reviewing my thesis before the submission and making a great team work and atmosphere.

Special gratitude to Prof. Dr. Emanuel Mazor from Weitzmann Institute, for the explanations about thermal water formation and groundwater analyzing.

My dear friends, Paul Bauer and Svenja Reith, thank you so much for reviewing my thesis with a lot of attention and care. Special thanks to my boyfriend Clemens Schwingshackl. I really appreciate your help with my thesis and the support, especially during busy times.

At last, I would like to thank my parents, Raya and Shraga Tsur and my brother, Yuval Tsur, for driving with me to all the sites and helping with the sampling.

All of you, who are not mentioned here, I would like to thank you too for your contribution to my work.



# Bibliography

- Aeschbach-Hertig, W. (2005). A comment on “Helium sources in passive margin aquifers - new evidence for a significant mantle  $^3\text{He}$  source in aquifers with unexpectedly low in situ  $^3\text{He}/^4\text{He}$  production” by MC Castro [Earth Planet. Sci. Lett. 222 (2004) 897–913]. *Earth and Planetary Science Letters*, 240(3):827–829. [27](#), [28](#)
- Aeschbach-Hertig, W., El-Gamal, H., Wieser, M., and Palcsu, L. (2008). Modeling excess air and degassing in groundwater by equilibrium partitioning with a gas phase. *Water Resources Research*, 44(8). [18](#), [20](#), [21](#)
- Aeschbach-Hertig, W., Peeters, F., Beyerle, U., and Kipfer, R. (1999). Interpretation of dissolved atmospheric noble gases in natural waters. *Water Resources Research*, 35(9):2779–2792. [22](#)
- Aeschbach-Hertig, W. and Solomon, D. K. (2013). Noble gas thermometry in groundwater hydrology. In *The Noble Gases as Geochemical Tracers*, pages 81–122. Springer. [15](#), [18](#), [20](#), [22](#), [45](#)
- Allègre, C., Staudacher, T., and Sarda, P. (1987). Rare gas systematics: formation of the atmosphere, evolution and structure of the Earth’s mantle. *Earth and Planetary Science Letters*, 81(2):127–150. [11](#)
- Arad, A. and Bein, A. (1986). Saline-versus freshwater contribution to the thermal waters of the northern Jordan Rift Valley, Israel. *Journal of Hydrology*, 83(1):49–66. [67](#), [71](#)
- Bajjali, W., Clark, I. D., and Fritz, P. (1997). The artesian thermal groundwaters of northern Jordan: insights into their recharge history and age. *Journal of hydrology*, 192(1):355–382. [71](#)
- Ballentine, C. and Hall, C. (1999). Determining paleotemperature and other variables by using an error-weighted, nonlinear inversion of noble gas concentrations in water. *Geochimica et Cosmochimica Acta*, 63(16):2315–2336. [22](#)
- Barkan, E., Luz, B., and Lazar, B. (2001). Dynamics of the carbon dioxide system in the Dead Sea. *Geochimica et Cosmochimica Acta*, 65(3):355 – 368. [63](#)
- Barnes, I., Irwin, W. P., and White, D. E. (1978). Global distribution of carbon dioxide discharges and major zones of seismicity. *Survey Water Resources Inv., Open-file rept*, pages 78–39. [29](#)
- Bayer, H.-J., Hötzl, H., Jado, A., Röscher, B., and Voggenreiter, W. (1988). Sedimentary and structural evolution of the northwest Arabian Red Sea margin. *Tectonophysics*, 153(1):137–151. [34](#)
- Bein, A. and Feinstein, S. (1988). Late Cenozoic thermal gradients in Dead Sea transform system basins. *Journal of Petroleum Geology*, 11(2):185–192. [71](#)

- Benson, B. B. and Krause Jr., D. (1976). Empirical laws for dilute aqueous solutions of nonpolar gases. *Journal of Chemical Physics*, 64(2):689–709. [16](#), [79](#)
- Benson, B. B. and Krause Jr., D. (1980). Isotopic fractionation of helium during solution: A probe for the liquid state. *Journal of Solution Chemistry*, 9(12):895–909. [23](#)
- Bergelson, G., Nativ, R., and Bein, A. (1999). Salinization and dilution history of ground water discharging into the Sea of Galilee, the Dead Sea Transform, Israel. *Applied Geochemistry*, 14(1):91–118. [12](#)
- Bröder, L. (2011). A paleoclimate record from groundwater of the Great Artesian Basin in Australia. Master's thesis, Heidelberg University. [32](#)
- Clark, I. and Fritz, P. (1997). Environmental isotopes in hydrology. [30](#)
- Clarke, W. B., Jenkins, W., and Top, Z. (1976). Determination of tritium by mass spectrometric measurement of  $^3\text{He}$ . *The international journal of applied radiation and isotopes*, 27(9):515–522. [23](#), [57](#), [59](#)
- Cook, P. G. and Herczeg, A. L. (2000). *Environmental tracers in subsurface hydrology*, volume 529. Kluwer Academic Publishers Boston. [16](#), [22](#)
- Craig, H. (1961a). Isotopic variations in meteoric waters. *Science*, 133(3465):1702–1703. [31](#), [68](#)
- Craig, H. (1961b). Standard for reporting concentrations of deuterium and oxygen-18 in natural waters. *Science*, 133(3467):1833–1834. [31](#)
- de Leeuw, G., Hilton, D., Fischer, T., and Walker, J. (2007). The He–CO<sub>2</sub> isotope and relative abundance characteristics of geothermal fluids in el salvador and honduras: New constraints on volatile mass balance of the central american volcanic arc. *Earth and Planetary Science Letters*, 258(1):132–146. [65](#)
- El-Isa, Z., Mechie, J., Prodehl, C., Makris, J., and Rihm, R. (1987). A crustal structure study of Jordan derived from seismic refraction data. *Tectonophysics*, 138:235–253. [35](#)
- Elliott, T. (2009). Earth science: Restoration of the noble gases. *Nature*, 459:520–521. [23](#)
- Freund, R. (1965). A model of the structural development of Israel and adjacent areas since upper cretaceous times. *Geological Magazine*, 102:189–205. [34](#)
- Freund, R., Garfunkel, Z., Zak, I., Goldberg, M., Weissbrod, T., Derin, B., Bender, F., Wellings, F. E., and Girdler, R. W. (1970). The Shear along the Dead Sea Rift [and discussion]. *Philosophical Transactions of the Royal Society of London. Series A, Mathematical and Physical Sciences*, 267(1181):107–130. [34](#)
- Friedrich, R. (2007). *Grundwassercharakterisierung mit Umwelttracern: Erkundung des Grundwassers der Odenwald-Region sowie Implementierung eines neuen Edelgas-Massenspektrometersystems*. Inaugural dissertation, Universität Heidelberg. [43](#)
- Garfunkel, Z., Zak, I., and Freund, R. (1981). Active faulting in the Dead Sea Rift. *Tectonophysics*, 80:1 – 26. [34](#), [35](#)
- Gat, J. and Carmi, I. (1970). Evolution of the isotopic composition of atmospheric waters in the Mediterranean Sea area. *Journal of Geophysical Research*, 75(15):3039–3048. [31](#), [68](#)

- Gat, J. R. and Dansgaard, W. (1972). Stable isotope survey of the fresh water occurrences in Israel and the northern Jordan Rift Valley. *Journal of Hydrology*, 16(3):177–211. [31](#), [67](#), [68](#)
- Gat, J. R., Mazor, E., and Tzur, Y. (1969). The stable isotope composition of mineral waters in the Jordan Rift Valley, Israel. *Journal of Hydrology*, 7(3):334–352. [31](#), [68](#)
- Giggenbach, W. (1992). Isotopic shifts in waters from geothermal and volcanic systems along convergent plate boundaries and their origin. *Earth and Planetary Science Letters*, 113(4):495–510. [32](#)
- Ginzburg, A., Makris, J., Fuchs, K., Prodehl, C., Kaminski, W., and Amitai, U. (1979). A seismic study of the crust and upper mantle of the Jordan-Dead Sea Rift and their transition toward the Mediterranean Sea. *Journal of Geophysical Research: Solid Earth*, 84(B4):1569–1582. [35](#)
- Gomez, F., Karam, G., Khawlie, M., McClusky, S., Vernant, P., Reilinger, R., Jaafar, R., Tabet, C., Khair, K., and Barazangi, M. (2007). Global positioning system measurements of strain accumulation and slip transfer through the restraining bend along the dead sea fault system in Lebanon. *Geophysical Journal International*, 168(3):1021–1028. [35](#)
- Graham, D. W. (2002). Noble gas isotope geochemistry of mid-ocean ridge and ocean island basalts: Characterization of mantle source reservoirs. In Porcelli, D., Ballentine, C., and Wieler, R., editors, *Noble Gases in Geochemistry and Cosmochemistry*, volume 47 of *Rev. Mineral. Geochem.*, pages 247–317. Mineralogical Society of America, Geochemical Society, Washington, DC. [23](#), [24](#)
- Griesshaber, O. and Oxburgh (1992). Helium and carbon isotope systematics in crustal fluids from the Eifel, the Rhine Grabben and Black Forest, F.R.G. *Chemical Geology*, 99:213 – 235. [29](#)
- Grothe, J. (1992). Datenerfassung und Datenauswertung am Heidelberger Low-Level-Tritium-Messsystem. *Diploma Thesis*, Universität Heidelberg. [45](#)
- Heaton, T. H. E. and Vogel, J. C. (1981). “excess air” in groundwater. *Journal of Hydrology*, 50:201–216. [17](#)
- Herzberg, O. and Mazor, E. (1979). Hydrological applications of noble gases and temperature measurements in underground water systems: Examples from Israel. *Journal of Hydrology*, 41:217–231. [12](#)
- Hoefs, J. (2009). *Stable isotope geochemistry*. Springer. [29](#), [32](#)
- Hoetzel (2009). *The water of the Jordan Rift Valley*. Springer-Verlag Berlin Heidelberg. [33](#), [36](#)
- Hoffmann, E. and Stroobant, V. (2007). Mass spectrometry principles and applications. *England: West Sussex*. [42](#)
- Horowitz, A. (2001). *The Jordan Rift Valley*. A.A. Balkema Publishers. [33](#), [34](#), [35](#), [36](#)
- Jung, M., Wieser, M., von Oehsen, A., and Aeschbach-Hertig, W. (2012). Properties of the closed-system equilibration model for dissolved noble gases in groundwater. *Chemical Geology*. [45](#)

- Kaudse, T. (2014). *Noble gases in groundwater of the Azraq Oasis, Jordan and along the central Dead Sea Transform*. In preparation, Heidelberg University. [12](#), [16](#), [43](#), [74](#), [77](#)
- Kipfer, R., Aeschbach-Hertig, W., Peeters, F., and Stute, M. (2002). Noble gases in lakes and ground waters. In Porcelli, D., Ballentine, C., and Wieler, R., editors, *Noble gases in geochemistry and cosmochemistry*, volume 47 of *Rev. Mineral. Geochem.*, pages 615–700. Mineralogical Society of America, Geochemical Society, Washington, DC. [17](#), [18](#), [20](#), [45](#)
- Kreuzer, A. (2007). *Paläotemperaturstudie mit Edelgasen in Grundwasser der Nordchinesischen Tiefebene*. Inaugural dissertation, Universität Heidelberg. [46](#)
- Lange, T., Hammerschmidt, K., Friedrichsen, H., Marei, A., and Weise, S. M. (2008). Groundwater in the shallow aquifer of the Jericho area, Jordan valley – noble gas evidence for different sources of salinization. In Zereini, F. and Hötzl, H., editors, *Climatic changes and water resources in the Middle East and North Africa*, pages 469–495. Springer, Berlin, Heidelberg. [12](#)
- Lupton, J. E. (1983). Terrestrial inert gases-isotope tracer studies and clues to primordial components in the mantle. *Annual Review of Earth and Planetary Sciences*, 11:371–414. [23](#), [24](#)
- Mamyrin, B. and Tolstikhin, I. (1984). *Helium isotopes in nature*, volume 3. Elsevier. [12](#), [18](#), [23](#)
- Mart, Y. (1991). The Dead Sea Rift: from continental rift to incipient ocean. *Tectonophysics*, 197:155 – 179. [33](#)
- Mart, Y., Ryan, W. B., and Lunina, O. V. (2005). Review of the tectonics of the Levant Rift system: the structural significance of oblique continental breakup. *Tectonophysics*, 395(3):209–232. [34](#)
- Marty, B. and Jambon, A. (1987).  $C/{}^3He$  in volatile fluxes from the solid earth: implications for carbon geodynamics. *Earth and Planetary Science Letters*, 83(1):16–26. [29](#), [66](#)
- Mayer, S. (2012). Analyzing short-term fluctuations of noble gas concentrations in soil air and groundwater. Master’s thesis, Heidelberg University. [19](#)
- Mazor, E. (1972). Paleotemperatures and other hydrological parameters deduced from gases dissolved in groundwaters, Jordan Rift Valley, Israel. *Geochimica et Cosmochimica Acta*, 36:1321–1336. [12](#)
- Mazor, E., Kaufman, A., and Carmi, I. (1973). Hammat Gader (Israel): Geochemistry of a mixed thermal spring complex. *Journal of Hydrology*, 18(3):289–303. [12](#), [67](#), [74](#), [75](#)
- Mazor, E., Levitte, D., Truesdell, A. H., Healy, J., and Nissenbaum, A. (1980). Mixing models and ionic geothermometers applied to warm (up to 60 °C) springs: Jordan Rift Valley, Israel. *Journal of Hydrology*, 45(1-2):1–19. [75](#)
- Möller, P., Dulski, P., Salameh, E., and Geyer, S. (2006). Characterization of the sources of thermal spring-and well water in Jordan by rare earth element and yttrium distribution and stable isotopes of  $H_2O$ . *Acta hydrochimica et hydrobiologica*, 34(1-2):101–116. [68](#), [75](#)

- Möller, P., Rosenthal, E., Geyer, S., and Flexer, A. (2007a). Chemical evolution of saline waters in the Jordan-Dead Sea transform and in adjoining areas. *International Journal of Earth Sciences*, 96(3):541–566. [68](#)
- Möller, P., Rosenthal, E., Geyer, S., Guttman, J., Dulski, P., Rybakov, M., Zilberbrand, M., Jahnke, C., and Flexer, A. (2007b). Hydrochemical processes in the lower Jordan valley and in the Dead Sea area. *Chemical Geology*, 239(1):27–49. [38](#), [67](#)
- O’Nions, R. and Oxburgh, E. (1988). Helium, volatile fluxes and the development of continental crust. *Earth and Planetary Science Letters*, 90(3):331–347. [29](#)
- Picard, L. (1987). The Elat (Aqaba)-Dead Sea-Jordan subgraben system. *Tectonophysics*, 141:23 – 32. [33](#)
- Quennell, A. . (1959). The structural and geomorphic evolution of the Dead Sea Rift. *Quart. J. Geol. Soc. London*, 114:1–24;432–433. [34](#)
- Quennell, A. (1956). Geologic map of the Kingdom of Trans Jordan. [34](#)
- R., F. (1970). Plate tectonics of the Red Sea and East Africa. *Nature*, 228:453. [34](#)
- Roded, R., Shalev, E., and Katoshevski, D. (2013). Basal heat-flow and hydrothermal regime at the Golan-Ajloun hydrological basins. *Journal of Hydrology*, 476:200–211. [71](#)
- Roedel, W. and Wagner, T. (2010). *Physik unserer Umwelt: Die Atmosphäre*. Springer Verlag, 4 edition. [16](#)
- Rosenthal, E. (1994). The hydrogeothermal provinces of Israel. In Risler, J.-J. and Simmers, I., editors, *Hydrogeothermics (International contributions to hydrogeology)*, pages 113–135. A A Balkema Publishers, Leiden, London, New York, Philadelphia, Singapore. [74](#), [75](#)
- Rosenthal, E., Guttman, J., Sabel, R., and Möller, P. (2009). Limiting hydrochemical factors for sustainability of water resources: The Cisjordanian experience. *Chemie der Erde-Geochemistry*, 69(3):191–222. [80](#), [81](#)
- Sano, Y. and Marty, B. (1995). Origin of carbon in fumarolic gas from island arcs. *Chemical Geology*, 119(1):265–274. [29](#), [31](#), [63](#), [65](#), [78](#)
- Sano, Y. and Wakita, H. (1988). Precise measurement of helium isotopes in terrestrial gases. *The Chemical Society of Japan*, 61:1153 – 1157. [12](#), [26](#)
- Sano, Y. and Williams, S. N. (1996). Fluxes of mantle and subducted carbon along convergent plate boundaries. *Geophysical Research Letters*, 23(20):2749–2752. [65](#)
- Schlosser, P., Stute, M., Sonntag, C., and Otto Münnich, K. (1989). Tritogenic  $^3\text{He}$  in shallow groundwater. *Earth and Planetary Science Letters*, 94(3):245–256. [18](#)
- Shalev, E., Lyakhovskiy, V., Weinstein, Y., and Ben-Avraham, Z. (2013). The thermal structure of Israel and the Dead Sea Fault. *Tectonophysics*. [71](#), [78](#), [95](#)
- Starinsky, A. (1974). *Relationship between Ca-chloride brines and sedimentary rocks in Israel*. PhD thesis. [37](#), [50](#), [82](#)
- Starinsky, A., Katz, A., and Levitte, D. (1979). Temperature-composition-depth relationship in Rift Valley hot springs: Hammat Gader, northern Israel. *Chemical Geology*, 27(3):233–244. [71](#)

- Stephen, H. and Stephen, T. (1963). *Solubilities of inorganic and organic compounds*, volume 1. Pergamon Press Oxford. [65](#)
- Stern, O. (2010). Geochemistry, hydrology and paleo-hydrology of Ein Qedem spring system. Master's thesis, The Hebrew University. [37](#), [50](#), [82](#)
- Sun, T., Hall, C. M., and Castro, M. C. (2010). Statistical properties of groundwater noble gas paleoclimate models: Are they robust and unbiased estimators? *Geochemistry Geophysics Geosystems*, 11(2):Q02002. [22](#)
- Torfstein, A., Hammerschmidt, K., Friedrichsen, H., Starinsky, A., Garfunkel, Z., and Kolodny, Y. (2013). Helium isotopes in Dead Sea Transform waters. *Chemical Geology*. [12](#), [36](#), [37](#), [63](#), [66](#), [71](#), [74](#), [75](#), [77](#), [78](#)
- Unkel, I. (2006). *AMS-14C-Analysen zur Rekonstruktion der Landschafts- und Kulturgeschichte in der Region Palpa (S-Peru)*. Inaugural dissertation, Universität Heidelberg. [45](#)
- Van Soest, M., Hilton, D., and Kreulen, R. (1998). Tracing crustal and slab contributions to arc magmatism in the lesser antilles island arc using helium and carbon relationships in geothermal fluids. *Geochimica et Cosmochimica Acta*, 62(19):3323–3335. [65](#)
- Wieser, M. (2011). *Imprints of climatic and environmental change in a regional aquifer system in an arid part of India using noble gases and other environmental tracers*. PhD thesis, Heidelberg University. [19](#), [43](#), [46](#)
- Wilson, J. (1965). A new class of faults and their bearing on continental drift. *Nature*, 207(4995):343–347. [34](#)
- Yecheili, Y., Starinsky, A., and Rosenthal, E. (1992). Evolution of brackish groundwater in a typical arid region: Northern Arava Rift Valley, southern Israel. *Applied Geochemistry*, 7(4):361 – 374. [37](#)